PCCP

ROYAL SOCIETY OF CHEMISTRY

PERSPECTIVE

View Article Online
View Journal | View Issue

Cite this: *Phys. Chem. Chem. Phys.*, 2022, **24**, 9082

Construction and physical properties of low-dimensional structures for nanoscale electronic devices

Lihong Bao, [ab] Li Huang,[a] Hui Guo[a] and Hong-Jun Gao *[ab]

Received 31st December 2021,
Accepted 23rd March 2022

DOI: 10.1039/d1cp05981e

rsc.li/pccp

Over the past decades, construction of nanoscale electronic devices with novel functionalities based on low-dimensional structures, such as single molecules and two-dimensional (2D) materials, has been rapidly developed. To investigate their intrinsic properties for versatile functionalities of nanoscale electronic devices, it is crucial to precisely control the structures and understand the physical properties of low-dimensional structures at the single atomic level. In this review, we provide a comprehensive overview of the construction of nanoelectronic devices based on single molecules and 2D materials and the investigation of their physical properties. For single molecules, we focus on the construction of single-molecule devices, such as molecular motors and molecular switches, by precisely controlling their self-assembled structures on metal substrates and charge transport properties. For 2D materials, we emphasize their spin-related electrical transport properties for spintronic device applications and the role that interfaces among 2D semiconductors, contact electrodes, and dielectric substrates play in the electrical performance of electronic, optoelectronic, and memory devices. Finally, we discuss the future research direction in this field, where we can expect a scientific breakthrough.

1. Introduction

Low-dimensional structures and their hierarchical systems, including atom clusters, molecules, quantum dots, nanowires, nanoribbons, nanotubes, and two-dimensional atomic crystals, are important building blocks for bottom-up construction of nanoscale electronic devices with novel functionality.[1–10] As one of the smallest building blocks, molecules often self-assemble into ordered nanostructures on solid surfaces.[11–39] By precisely controlling their structures and properties,[11,12,18,21,26,40–57] data recording by switching of charge and spin states [10,52,54,58–63] at a single molecule level has been realized, enabling the integration of

[a] *Institute of Physics & University of Chinese Academy of Sciences, Chinese Academy of Sciences, Beijing, 100190, P. R. China. E-mail: hjgao@iphy.ac.cn*
[b] *Songshan Lake Materials Laboratory, Dongguan, Guangdong, 523808, P. R. China*

Lihong Bao

Lihong Bao received his PhD in Condensed Matter Physics from the Institute of Physics (IOP), Chinese Academy of Sciences (CAS), in 2008. Then he carried out his postdoctoral research in USA. He was appointed as an Associate Professor in 2013 in the IOP, CAS. His current research interest is on the construction of nanoscale electronic devices and the physical properties of low-dimensional materials.

Hong-Jun Gao

Hong-Jun Gao received his PhD in physics from Peking University in 1994. He became a Professor in the Institute of Physics, Chinese Academy of Sciences, in 1995. He is an Academician of the Chinese Academy of Sciences, an Academician of the Developing-Country Academy of Sciences (TWAS), and an Academician of the German National Academy of Sciences. His research interest is on the construction and physical properties of quantum nanostructures including 2 dimensional atomic/molecular crystals, and scanning tunneling microscopy/spectroscopy.

device functions at a single molecule level,[2,64–72] such as single-electron transistors,[73] single-molecule transistors,[74–76] and single-molecule switches.[77–80] Moreover, controlling the motion of molecules at a single molecule level[16,46,49,53,56,81] allows for the construction of molecular machines,[82–87] including molecular nanocars,[88–90] molecular propellers,[91–93] molecular gears,[94–96] and molecular motors,[16,56,83,97–104] which builds up a fundamental basis for future nanoengineering of biological processes like those of natural motor proteins.

Two-dimensional (2D) atomic crystals,[105–107] such as graphene[108,109] and transition metal dichalcogenides,[110] have atomically thin and flat surfaces and are free of dangling bonds,[111] facilitating effective gate control even at the ultimate 2D atomic layer limit,[112] and constitute the promising building blocks for construction of high-performance nanoelectronic devices[113] and integrated circuits.[114] For graphene, since its successful isolation by the mechanical exfoliation method in 2004,[108] tremendous efforts have been devoted to growing large-scale and high-quality graphene, such as chemical vapor deposition (CVD) growth on metal[115–118] or dielectric substrates[119–122] and epitaxial growth on metal substrates.[123–125] However, the introduction of wrinkles or contaminations during the transfer process after growth severely influences the intrinsic properties of graphene.[126–134] Furthermore, the presence of defects formed during growth, such as grain boundaries,[133,135–141] makes the construction of high-performance electronic and quantum devices even more challenging. Therefore, developing a transfer-free method to place graphene on dielectric substrates to be compatible with Si technology is highly required.

Beyond graphene, transition metal dichalcogenides (TMDCs) with the chemical formula of MX_2,[110,142] in which M stands for transition metals (such as Mo, W, Nb, V, and Cr) and X stands for chalcogen elements (such as S, Se, and Te), emerge as a family of materials with novel properties, such as thickness-dependent bandgaps,[110] strong spin–orbit coupling (SOC),[143] and valley polarization,[144] making them attract extensive research attention in not only their novel physical properties[145] but also their applications for nanoelectronics and nanophotonics.[146] In monolayer transition metal dichalcogenides, the inversion symmetry is broken and the strong SOC will induce degeneration of valley-locked spin–split,[145,147] allowing for control of the spin and valley polarization states for next generation spintronic and valleytronic devices.[144,148–150] Moreover, the experimental discovery of intrinsic ferromagnetism in mono- or few-layered CrI_3,[151] $Cr_2Ge_2Te_6$,[152] and VSe_2[153] has ignited intense exploitation of 2D magnetism in TMDCs.[154–156]

van der Waals (vdW) heterostructures with atomically clean and sharp interfaces can be formed by layer-by-layer stacking of 2D materials with different band profiles,[157,158] providing unprecedented opportunities for construction of novel electronic devices. The wide range of band gaps in 2D semiconductors from 0.4 to 2.0 eV allows the formation of vdW heterostrucutures with type I (straddling gap), type II (staggered gap), and type III (broken gap) band alignments.[159,160] Compared to conventional quantum wells or superlattices, vdW heterostructures have steep band edges, giving rise to revolutionary possibilities of quantum engineering the transport of charge carriers and excitons.[161] Moreover, vdW heterostructures can be formed by either vertically or laterally stacking 2D semiconductors, enabling the construction of novel proof-of-principle devices.[162–168] Benefitting from their atomically clean and sharp interface properties, these electronic and optoelectronic devices showed extraordinary performance and unique functionality.[169]

In this article, we present a comprehensive review on the recent progress and frontiers of the construction and physical properties of low-dimensional structures for nanoscale electronic devices. Firstly, we review the construction of a single molecule device (Section 2), which represents the smallest building block for nanoscale electronic devices. Then we discuss the construction of electronic devices based on high-quality and single-crystal graphene epitaxially grown on a Ru(0001) substrate (Section 3), the electrical transport properties of magnetic transition metal dichalcogenides (Section 4), and construction of nanoscale electronic devices based on 2D materials (Section 5). Finally, we summarize this review and give an outlook for future research in this field.

2. Construction of a single molecule device

In organic electronic devices, the charge transport behavior is mainly governed by the orientation and stacking of molecules.[64,71,170] In the past years, great efforts have been devoted to controlling the formation of molecular structures and their electronic properties at the single molecule level,[11,41,81] such as the growth dynamics of various functional molecules and single molecule configurations on metal surfaces with monolayer or sub-monolayer coverage,[12,13,17–22,26,29,32,47,171,172] spin-dependent electronic properties of molecules with magnetic ion centers,[24,25,48,52,54,55,60–62] and motion of single molecules on metal surfaces.[16,41,49,56,81] One of the key challenges for single molecule electronic devices lies in how to control their electronic transport properties through a single-molecule junction,[173] *i.e.* control their electronic conduction channels by modulating the various molecular orbitals to get two stable and distinguishable electronic states for either logic or memory device applications.[10,36,52,54,58,59,61,62,174] Good control over the rotation axis and frequencies of the molecules in their self-assembled structures on a very large scale is the key requirement for construction of molecular machines like molecular rotors.[16,41,49,56,81]

2.1 Construction of a single molecular rotor and its array formation on Au(111) surfaces. As an important member of the family of molecular machines, molecular rotors can convert external energy into orchestrated motion at the molecular level, such as light illumination, chemical reactions, and electric fields. Precise design and control over the ''on'' and ''off'' states of molecular rotors have great implications for their eventual applications, which has been realized by charge states, selection of anchoring sites, and interaction between rotors and surrounding molecules. Furthermore, the capability of self-assembling individual molecular motors into large scale ordered arrays while retaining their original functions is the

key ingredient for their further integration into complex molecular machines. Molecular motors assembled on solid surfaces can be easily accessed by applying an electric field and addressed by *in situ* surface analysis techniques, such as scanning tunneling microscopy (STM), which can image the molecular motors with ultra-high spatial resolution, study the dynamics of molecules by inelastic electron tunneling spectroscopy, and manipulate the molecular motors with STM tips.

Phthalocyanines (Pcs) and their derivatives represent an ideal class of molecules to construct molecular motors because a well-defined off-center rotation axis is fixed on the surface by anchoring the nitrogen atom in the molecular framework by a single metal adatom on the reconstructed metal substrate by forming strong N–metal bonds.[16,56] The lateral motion of the molecule keeps it stationary with respect to the anchoring site, while the rotational degree of freedom around the nitrogen–metal bond is conserved by thermal excitation.[16,56] Fig. 1(a) shows an STM image of a large-scale ordered molecular motor array of tetra-*tert*-butyl zinc phthalocyanine [$(t\text{-Bu})_4$–ZnPc] molecules on a $22 \times \sqrt{3}$ reconstructed Au(111) surface.[17,23,25,175–180] Most of the molecules adsorb at the elbow positions of the Au(111) reconstructed surface (Fig. 1(b)), forming a "folding fan" structure (Fig. 1(b and c)). The tunneling current periodically oscillates with amplitudes between 0 and 5 nA (Fig. 1(d)), revealing that the "folding fan" feature comes from the frequency mismatch between the low-frequency imaging and high-frequency rotation of (*t*-Bu)4–ZnPc molecules driven by thermal energy. The presence of a rotation center is the prerequisite for rotation of molecules, which is formed by pinning of one nitrogen atom of (*t*-Bu)4–ZnPc molecules by one Au adatom on the Au(111) surface.[16] Fig. 1(e) shows an STM image of a single $(t\text{-Bu})_4$–ZnPc molecule. After removing the molecule during scanning, the Au adatom at the elbow site was clearly observed (Fig. 1(f).

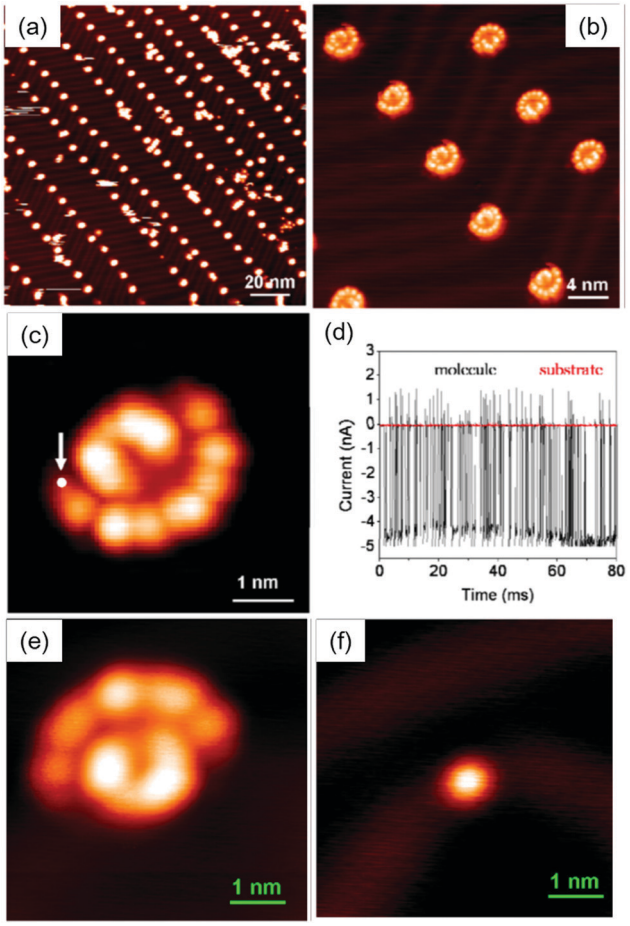

Fig. 1 STM characterization of a large-scale ordered molecular motor array of $(t\text{-Bu})_4$–ZnPc molecules on an Au(111) surface: (a) large-scale ordered array; (b) molecular rotors and (c) single molecule rotor showing a "folding fan" feature. (d) Tunneling current *versus* time spectrum measured on the molecular rotor. The position taken for the *I*–*t* spectrum is indicated by the arrow and spot in (c). (e) STM image of one single $(t\text{-Bu})_4$–ZnPc molecule at the elbow position. (f) Au adatom acting as the rotation center after the molecule in (e) was removed during scanning. Adapted with permission from ref. 16. Copyright 2008, American Physical Society.

Fig. 2(a and b) shows the top and side views of the optimized configuration for a $(t\text{-Bu})_4$–ZnPc molecule adsorbed on an Au adatom on the Au(111) surface calculated by density-functional calculations, in which the strong chemical bond between nitrogen and the gold adatom ensures the formation of a fixed off-center axis for the rotation of $(t\text{-Bu})_4$–ZnPc molecules. The molecular rotation is strongly dependent on the surface atom arrangement of the Au(111) surface. For gold adatoms located in the different regions of the herringbone structure of the reconstructed Au(111) surface,[181] such as face-centered cubit (fcc), hexagonal close packed (hcp), corrugation ridges, and elbow sites, the adsorbed $(t\text{-Bu})_4$–ZnPc molecule displays very different features. For a large-scale array of $(t\text{-Bu})_4$–ZnPc molecular rotors, all single molecular motors are anchored at the elbow sites, showing a "folding fan" feature (Fig. 2(c)).[16] In contrast, STM images of the molecular rotors located in the fcc region (Fig. 2(d)), in the hcp region (Fig. 2e), and on the corrugation ridges all show "flower" features. Fig. 2(f) shows the model for the rotation of a single $(t\text{-Bu})_4$–ZnPc molecule, in which *tert*-butyl groups are imaged as the bright lobes in STM images and twelve stable adsorption configurations 30 degrees apart from each other are the intermediate states for the molecular rotation. Under thermal excitation, the molecule switches between different intermediate states with high frequency, showing the "flower" feature (Fig. 2(d and e)). For the rotation of the $(t\text{-Bu})_4$–ZnPc molecule at elbow sites, the corrugation ridges limit the molecular rotation within an angle of 120° due to the bending of corrugation lines, resulting in the "folding-fan" feature. Compared with other ways of controlling the molecular rotation, such as chemical environment, light excitation, temperature, and STM tip manipulation, this method provides a facile scheme to control the molecular rotation with atomic precision by varying the anchoring sites of molecular motors.

Replacing the center metal atoms in Pc molecules will not change their rotational motion because the axis is formed by the chemical bond between one of the imine nitrogen atoms and Au adatoms on the surface, such as for $(t\text{-Bu})_4$–NiPc molecules, and two distinct current levels in the tunneling current (*I*)–time (*t*) curve indicate the rotational hopping or

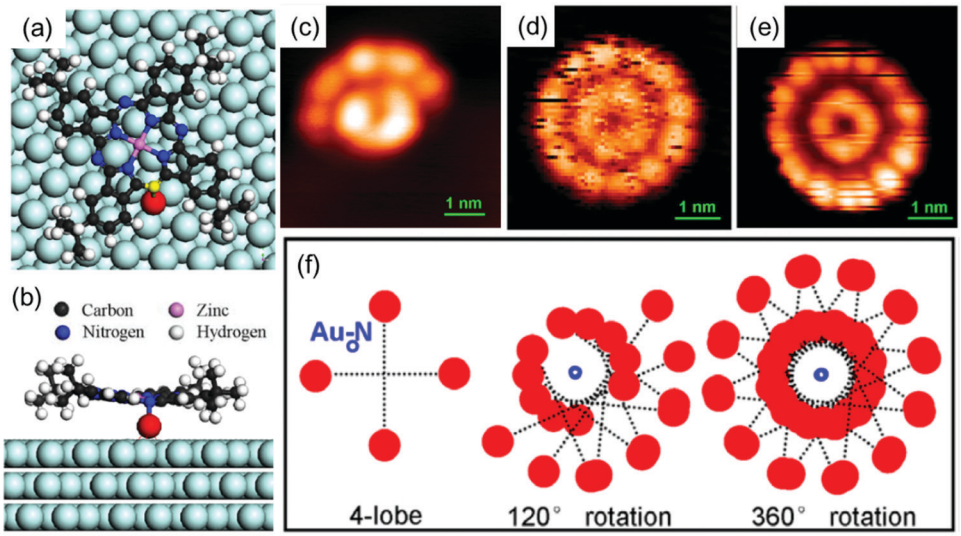

Fig. 2 (a) Top view and (b) side view of the optimized configuration of a $(t\text{-Bu})_4$–ZnPc molecule adsorbed on the Au(111) surface *via* a gold adatom calculated by density-functional calculations. The molecular formula of $(t\text{-Bu})_4$–ZnPc is $C_{48}H_{48}N_8Zn$. (c)–(e) STM images of $(t\text{-Bu})_4$–ZnPc molecules adsorbed onto the elbow site (c), fcc site (d), and hcp site (e) of the reconstructed herringbone structure of the Au(111) surface. (f) Schematic images of molecular rotors with rotation angles of 120° and 360°. The red solid circles represent the bright lobes for stationary single molecules. The blue empty circle represents the rotation center. Adapted with permission from ref. 16. Copyright 2008, American Physical Society.

random switching between two configurations of the molecule.[56,99,182] This behavior can be changed by varying the STM tip–molecule distance, by which the occupation probability of the molecular configuration is changed due to the change in potential energy of each configuration.[56] Furthermore, changing the voltage bias of the STM tip can also tune the potential energy of the molecular configuration. In this way, no matter what kind of activation mechanism is applied, such as heat, electric field, and light, the rotational motion of molecular motors can be manipulated by modification of their potential energy by varying the tip-molecule distance and sample bias.

2.2 Reversible single spin transition of a molecule and its data recording. Control over the charge and spin states at the single molecule level plays a crucial role in not only the fundamental understanding of charge and spin interactions in single molecules but also the development of future molecular electronics and spintronics.[2,63,67,71,72,79,183–189] To this end, great efforts have been devoted to probing electronic transport properties through a single-molecule junction,[63,67,73,74,184,186–188,190–202] in which the electron transport can be controlled by field regulation of single-molecule conductivity using a charged surface atom,[194] by tuning the molecular conformation,[184] by molecular interactions,[197] using local electric fields,[203] by hydrogenation of molecules,[180,204] or by tuning molecular adsorption sites.[205] Although the spin states of molecules can be controlled mechanically[206] or electrically,[207] or by applying magnetic fields,[61,208,209] reversible control of a single spin of the molecule is still quite challenging.[63,66,67,187,188,201] The spin states of molecules can manifest themselves as spin-related transport phenomena, such as negative differential resistance[209] or the Kondo effect,[60,180,205] in which the spin of the molecules is coupled to the conduction channels and a conduction anomaly emerges at the Fermi level.[68,190,210,211] Many attempts have been applied to tune the Kondo effect of molecule systems, including conformation variation,[212] alternation of adsorption sites,[213] quantum size effects,[214] ligand attachment,[215] molecular assembly,[216] and atomic doping;[217] however, none of them are reversible or can tune the Kondo effect at the single-molecule level. Reversible control of the spin transition of a molecule at the single-molecule level is both fundamentally important and promising for applications in data recording.

Magnetic metal phthalocyanines (MPcs) and metal porphyrins (MPs) with a single magnetic metal ion are an ideal class of molecules to probe and modulate the Kondo effect at the single-molecule level,[212,218,219] because when they are placed on metal surfaces, well-defined Kondo resonances induced by the correlated interaction between the local spin of the metal ions and conduction electrons from the metal substrate can be easily observed.[180,205] For example, for iron phthalocyanine (FePc) molecules adsorbed on an Au(111) surface, the Kondo effect was clearly observed for two adsorption sites and the Kondo temperature is well above room-temperature,[205] showing the great capability of tuning the Kondo effect at the single-molecule level by changing the adsorption sites and molecular configuration. When replacing the Fe metal ion with Mn, the isolated MnPc molecules that adsorbed onto the Au(111) surface preferably occupy the elbow sites of the reconstructed Au(111) surface first and then face centered cubic (fcc) sites,[28] as shown in Fig. 3(a). A protruding "cross" feature with four-fold symmetry was clearly observed due to three inherent unpaired electrons with a total spin of $S = 3/2$ in each MnPc molecule.[60] Fig. 3(b) shows that the bright protrusion of the center of MnPc molecules is depressed after being dosed with H_2. The dI/dV curve collected at the center of MnPc molecules reveals a pronounced step shaped feature close to the Fermi level at zero bias (Fig. 3(c)). Such a feature shows a linear

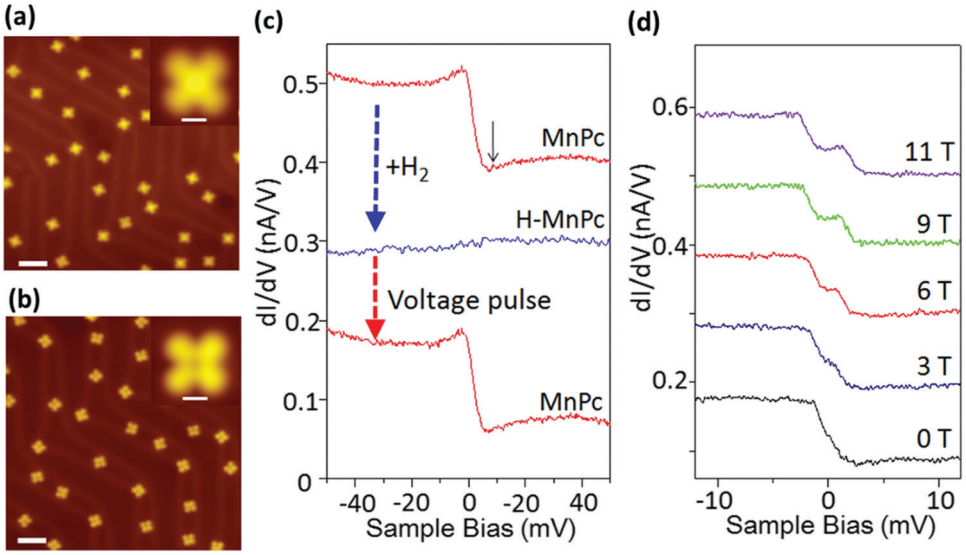

Fig. 3 STM images and d*I*/d*V* curves of the MnPc molecules on the Au(111) surface before and after hydrogen atom adsorption. STM images of the MnPc molecules adsorbed onto the Au(111) surface (a) and after hydrogen atom decoration (b), showing molecules with (a) and without (b) a bright center, respectively. Scale bars are 5 nm. Insets show high-resolution images of a single molecule with (a) and without (b) a bright center. Scale bars are 0.7 nm. (c) d*I*/d*V* spectra collected at the center of a MnPc molecule induced by the absorption and desorption of a single hydrogen atom. (d) d*I*/d*V* spectra recorded at the center of the MnPc molecule under an external magnetic field at 0.4 K, showing the splitting of Kondo resonance. Adapted with permission from ref. 60. Copyright 2013, Springer Nature.

splitting feature under magnetic fields, a hallmark of Kondo resonance,[190,205,211,214–216] as displayed in Fig. 3(d). In comparison, the d*I*/d*V* curve collected at the center of MnPc molecules after hydrogen atom deposition (H-MnPc) is featureless in the same energy range, showing the depression of the Kondo effect. By applying a positive voltage pulse onto the depressed center of the MnPc molecules, the bright protrusion and Kondo resonance features can be fully recovered due to the tip-induced detachment of adsorbed hydrogen atoms from MnPc molecules.[204] This shows the great success of the reversible control of single spin in magnetic molecules at the single-molecule level by turning "ON" and "OFF" of the Kondo effect through hydrogen atom decoration.

Both the bright protrusion feature of the MnPc state and the depressed feature of the H-MnPc state can be well reproduced by STM simulation by adoption of the Tersoff–Hamann approximation[220] in density functional theory (DFT) calculation, as shown in Fig. 4(a). The physical mechanism for the spin switching process is revealed by calculating the projected density of states (PDOS) of the MnPc state and H-MnPc state of the molecules. As shown in Fig. 4(b and c), the PDOS of d_{xz}, d_{yz} and d_z^2 orbitals of Mn ions in MnPc and H-MnPc clearly show the transition of the spin of $S = 3/2$ of MnPc molecules to S = 1 of H-MnPc molecules. The calculated binding energy of 1.75 eV between the hydrogen atom and MnPc molecules confirmed the chemical adsorption nature of the hydrogen atom decoration on MnPc molecules. Such reversible tuning of the Kondo "ON" and "OFF" states by hydrogen adsorption and desorption on single MnPc molecules is schematically shown in Fig. 4(d).

From the fundamental principle of information recording and storage, the presence and disappearance of the Kondo resonances in the MnPc molecule can be considered as the "0" and "1" logic states of a single bit of information, respectively. Benefiting from the capability of atomic manipulation of molecular adsorption and desorption by STM, information recording and storage at the ultimate molecular limit can be realized. Fig. 5(a) shows the STM image and d*I*/d*V* mapping of a 3×4 molecular array of MnPc molecules on an Au(111) surface. All the MnPc molecules within the array are initially decorated into H-MnPc molecules by adsorption of hydrogen atoms, which is verified by the featureless d*I*/d*V* mapping, *i.e.* absence of the Kondo resonance (Kondo "OFF" state). By selectively applying positive voltage bias on H-MnPc molecules, an individual molecule within the array can be precisely addressed and the selected H-MnPc molecules can be converted back to the MnPc state (Fig. 5(b)). Fig. 5(c) shows the conversion of H-MnPc molecules in a close-packed array with the highest molecular density. Both the STM images and d*I*/d*V* mapping clearly demonstrate the robustness of such operation. Even when the intermolecular spacing was reduced to as small as 1.4 nm in the close-packed array, all the dark-dot features can still be localized at the center of the MnPc molecules, and the characteristic parameters of the Kondo resonance in their d*I*/d*V* curves, such as the Fano factor (q) and the Kondo temperature (T_K), are consistent with those of isolated molecules (Fig. 5(d)). Such reversible tuning of the Kondo effect at the single-molecule level by adsorbing or desorbing a single hydrogen atom to reversibly control the single spin state of magnetic molecules provides a robust and effective method to atomically precisely manipulate the single spin states of a single molecule and will have great implications for non-volatile information recording and storage at the molecular level without the change in molecular conformations.

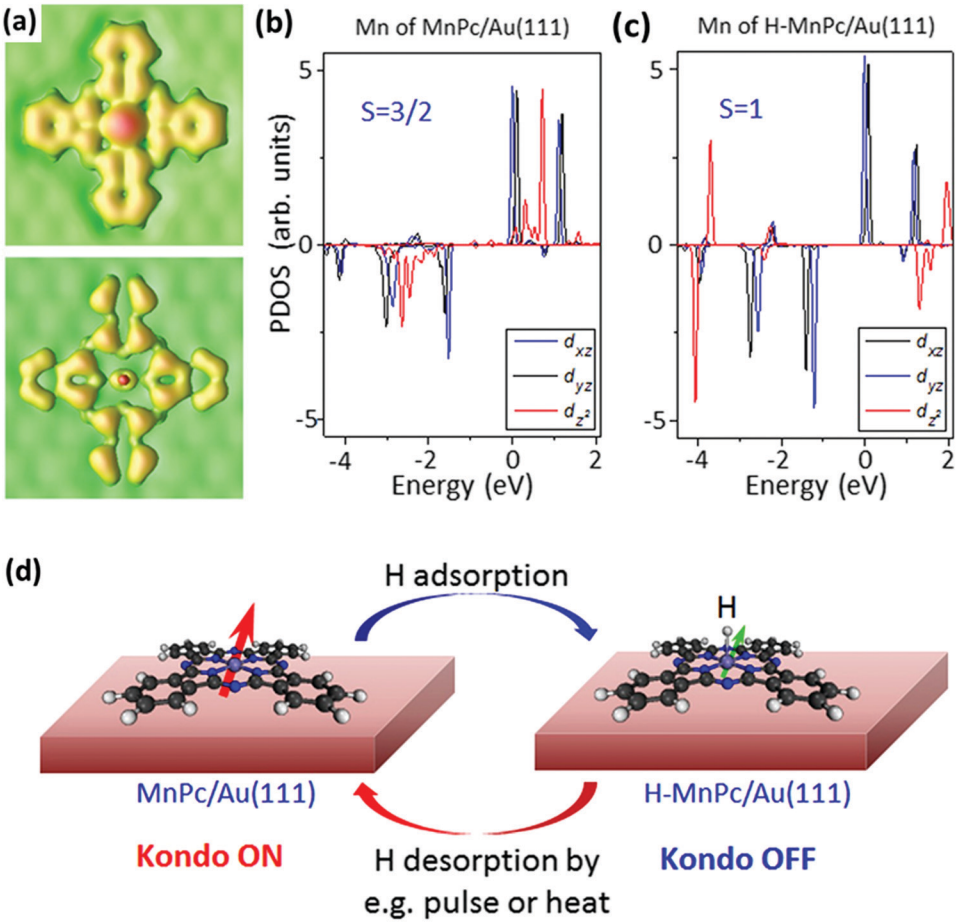

Fig. 4 STM simulation and PDOS of the MnPc/Au(111) before and after hydrogen adsorption. (a) Simulated STM images of the MnPc/Au(111) and the H-MnPc/Au(111), reproducing the topographic features in Fig. 3a and b. (b) and (c) PDOS of d_{xz}, d_{yz} and d_{z^2} orbitals of Mn ions in the MnPc/Au(111) and the H-MnPc/Au(111), respectively, revealing that the spin at the Mn ion is reduced from 3/2 to 1. (d) Schematics of reversible control of the molecular Kondo effect with adsorption (Kondo OFF) and desorption of hydrogen atoms (Kondo ON). Adapted with permission from ref. 60. Copyright 2013, Springer Nature.

3. Construction of electronic devices based on large-scale and high-quality graphene epitaxially-grown on Ru(0001)

Graphene, a monolayer of carbon atoms with honeycomb lattices, ignites explosive research interest in not only studying the fundamental properties[108,109,221–224] but also fabricating high-performance electronic devices[225–230] at the two-dimensional atomic layer limit. In the past decades, various techniques have been developed to prepare high-quality graphene monolayers, such as mechanical exfoliation from bulk graphite,[108,222,231,232] chemical vapor deposition (CVD) on metal[115–118] or dielectric substrates,[119–122] and epitaxial growth on metal substrates.[123–125] However, either the as-grown graphene has small grain size or needs to be transferred onto a dielectric substrate, which will severely degrade the mobility of graphene and greatly limit its practical applications in constructing future nanodevices or quantum devices. Previous results have shown that Si can be intercalated into the interface between graphene and epitaxial substrates in a non-destructive way,[233–237] which represents the best way to develop a transfer-free and Si-technology compatible route to prepare large-scale and high-quality graphene and facilitate its further device integration.

3.1 Epitaxial growth of centimeter-scale and single-crystal graphene

Centimeter-scale and single-crystal graphene can be epitaxially grown on metal substrates either by directly annealing metal crystals, such as Ru(0001),[123–125] Ni(111),[238–240] Pt(111),[238,241] and Ir(111),[237] or by annealing them under ethylene exposure.[50,238,241,242] Low-electron-energy-diffraction (LEED) patterns collected from different regions of graphene grown on a Ru(0001) substrate indicate that centimeter-scale, single-crystal graphene was formed on the whole Ru(0001) surface, as shown in Fig. 6. The weak signals of graphene at the edges of the Ru(0001) substrate shown in Fig. 6(a and f) suggest that graphene was not formed at the edges of the substrate, compared to the identical LEED patterns of both graphene and the Ru(0001) surface shown in Fig. 6(c–e). The STM image shown in Fig. 6(g) reveals the uniformity and continuity of the as-grown large-scale graphene. A moiré pattern with a periodicity of

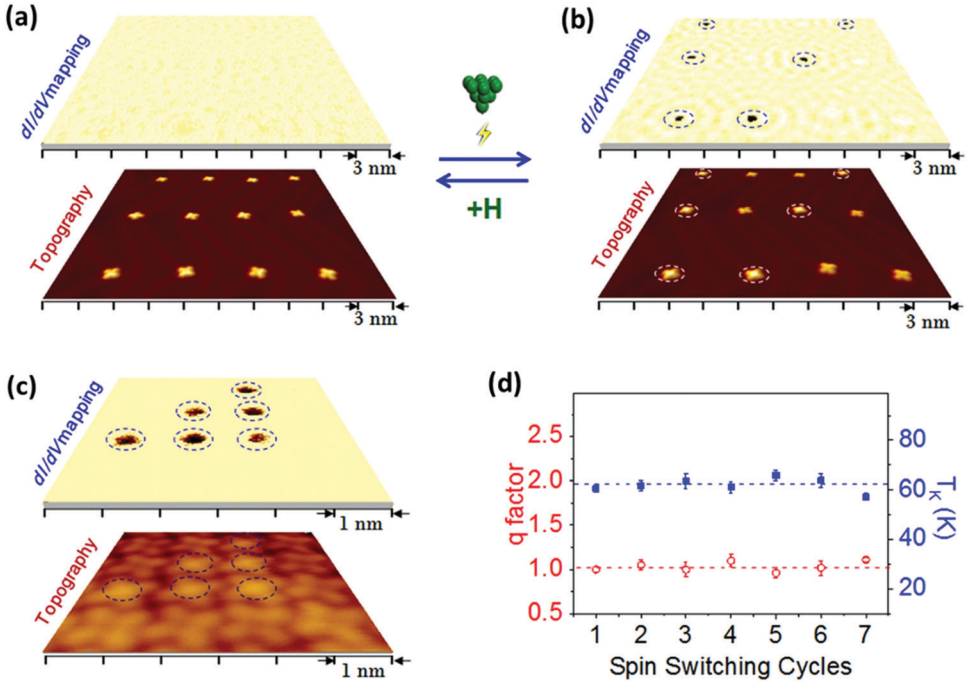

Fig. 5 Reversible spin switching in molecular arrays. The d*I*/d*V* mapping (upper panel) and simultaneously acquired topography (lower panel) of a H-MnPc molecular array (Kondo OFF state) (a) and selective conversion of H-MnPc molecules to the MnPc state (Kondo OFF) (b) by adsorption of additional hydrogen. (c) The d*I*/d*V* mapping (upper panel) and topography (lower panel) of a close-packed molecular array with a pre-designed Kondo pattern by switching selected molecules from the H-MnPc to MnPc states within the array. (d) The Fano factor q and Kondo temperature T_K of Kondo ON states after multiple-cycles of spin switching, indicating the robustness of the spin manipulation process. Adapted with permission from ref. 60. Copyright 2013, Springer Nature.

~3 nm that formed by the superposition of lattices of graphene and the Ru(0001) surface in a mismatched manner is shown in Fig. 6(h). Fig. 6(i) shows an atomic-resolution STM image of one unit cell of the moiré pattern outlined by the rhombus, clearly resolving the three different structural regions of rippled graphene on Ru(0001), including the atop region (the bright region indicated with a green circle), the hcp region of graphene (yellow dotted triangle), and the fcc region (white dashed triangle). The inset in Fig. 6(i) shows the atomic structure of the unit cell of the moiré pattern calculated by DFT, which is consistent with the STM image in Fig. 6(i). These results highlight that centimeter-scale and single-crystal graphene can be successfully prepared on Ru(0001) substrates by epitaxial growth, which meets the prerequisites of large-scale and defect-free graphene at the atomic level for device integration.

3.2 Insulating SiO_2 under centimeter-scale, single-crystal graphene

After high-quality and large-scale graphene films have been successfully epitaxially grown on Ru(0001), the key challenge for constructing high-performance graphene electronic devices lies in developing a transfer-free and Si-technology compatible method to place graphene on Si or SiO_2 substrates and realizing electrically insulating isolation from metal Ru substrates. Previous results have shown that by intercalating Si between epitaxial graphene and a metal substrate, graphene can be decoupled from the metal Ru substrate with the appearance of a graphene honeycomb lattice, while maintaining the large scale nature and high quality of graphene.[233] This non-destructive and transfer-free method can prevent graphene from quality degradation and possible contamination, ensuring the successful fabrication of graphene/silicene van der Waals heterostructures.[236] Vertical electrical transport measurement on such heterostructures shows a typical Schottky-like rectification behavior with an ideality factor of ~1.5, suggesting that after Si intercalation a good interface is formed between graphene and silicene.[233,235,236] By combination of STM imaging and DFT calculations, it has been found that cooperative interactions between heteroatoms, graphene, and substrates govern the intercalation process, which consists of four key steps: creation of defects, migration of heteroatoms, self-repairing of graphene, and growth of an intercalcaed monolayer.[235] Recently, insulating SiO_2 beneath centimeter-scale and single-crystal graphene has been successfully fabricated by stepwise intercalation of silicon and oxygen into the interface between graphene and the Ru(0001) substrate.[243]

Fig. 7 schematically shows the different stages of sample growth and the corresponding LEED patterns. The LEED pattern of graphene grown on Ru(0001) shown in Fig. 7(d) indicates that the as-grown graphene has high quality. After stepwise intercalation of Si and O and post-annealing at 850 K, diffraction spots from the moiré structure disappear, and a new set of diffraction spots with a 2×2 superstructure with respect to the Ru(0001) surface lattice appears, which comes

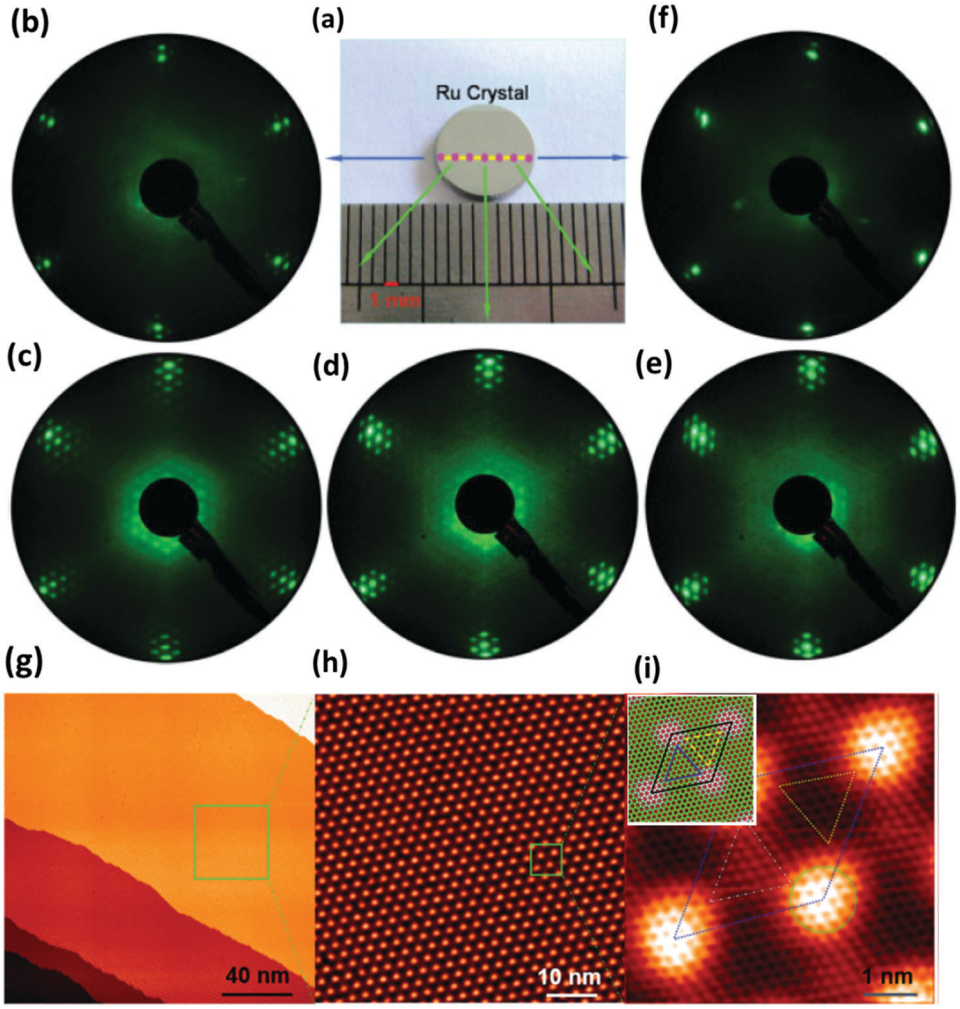

Fig. 6 LEED patterns and STM images of graphene epitaxially grown on Ru(0001). (a) Photograph of the sample with a diameter of 8 mm. (b–f) LEED patterns collected from the different regions of G/Ru(0001). The corresponding region is indicated by the pink spots in (a). In (b) and (f), the signal from graphene is rather weak, suggesting that no graphene is grown at the edges of the Ru(0001) substrate. (c)–(e) show the same LEED pattern, indicating that graphene is uniformly formed on the Ru(0001) substrate. (g) Large-scale STM image of graphene, showing its atomically flat nature. (h) Zoom-in image of (g), showing the moiré pattern formed by the superposition of the lattices of graphene and the Ru(0001) surface. (i) Atomic-resolution STM image of one unit cell of the moiré pattern, indicating a defect-free lattice structure. The upper inset shows the calculated atomic structure by DFT, which is consistent with the STM image in (i). Adapted with permission from ref. 125. Copyright 2009, Wiley-VCH Verlag GmbH & Co. KGaA, Weinheim.

from crystalline bilayer silica, as shown in Fig. 7(e). Repeated cycles of intercalation of Si and O result in the disappearance of diffraction spots related to crystalline silica due to the formation of a thick amorphous silica layer between graphene and the Ru(0001) substrate, as depicted in Fig. 7(f). In each stage of the above preparation process, the diffraction spots of graphene in the LEED pattern persist, revealing the non-destructive nature of such processes.

Fig. 8(a) shows a large-scale bright-field scanning tunneling electron microscopy (STEM) image of the cross section of a G/c-silica/Ru sample, revealing the formation of a silica layer with a thickness of ~1.1 nm. The high-resolution STEM image shown in Fig. 8(b) shows the atomic structure of the intercalated silica layer, which agrees well with the superimposed theoretical atomic structure of bilayer crystalline silica. The peak located at ~107.5 eV of Si-$L_{2,3}$ in the electron-energy-loss spectroscopy (EELS) curve in Fig. 8(c) is consistent with the Si^{4+} oxidization state of crystalline SiO_2,[244] further verifying the formation of crystalline bilayer silica. The clearly resolved perfect honeycomb lattice in the STM image and the absence of the D-peak in the Raman spectrum of graphene in Fig. 8(d) indicate that after c-silica intercalation graphene remains intact. Fig. 8(e) shows the STEM image of the cross-section of the G/a-silica/Ru(0001) sample after repeated cycles of intercalation of Si and O, showing a uniform amorphous layer with a thickness of ~1.8 nm between monolayer graphene and the Ru(0001) substrate. X-ray photoelectron spectroscopy performed on the intercalated layer reveals that the binding energies of the Si 2p and O 1s core levels are located at ~103.3 and ~532.5 eV (Fig. 8(f)), respectively, confirming the formation of SiO_2.[234] For *in situ* fabrication of electronic devices, electrically insulating isolation of graphene from the metal substrate is required.

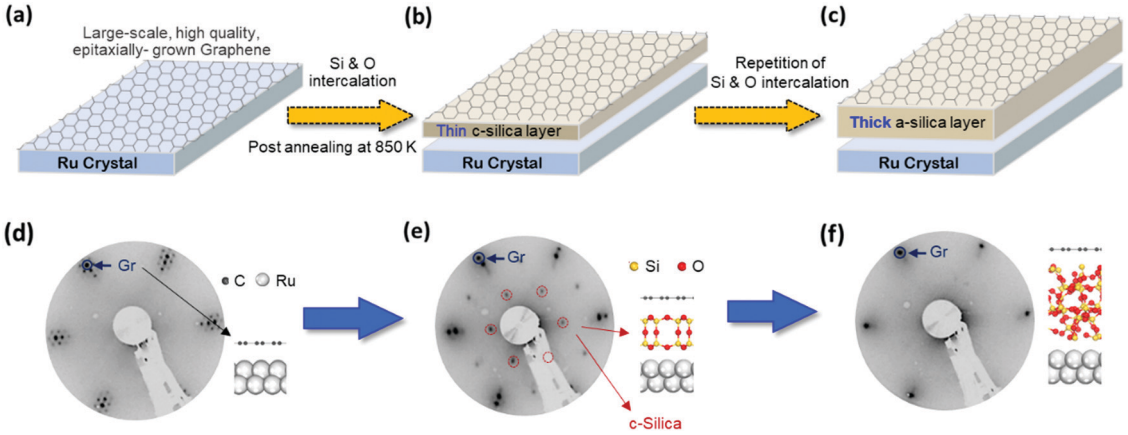

Fig. 7 Fabrication of insulating SiO_2 beneath centimeter-scale and single-crystal graphene. (a–c) Schematic diagram of different stages of sample preparation. (d–f) LEED patterns and structure models for the samples prepared in stages (a–c), respectively. (d) LEED pattern of stage (a), showing the formation of high-quality graphene and a moiré superlattice. (e) LEED pattern of sample (b) after the formation of a thin crystalline SiO_2 (c-silica) layer, indicating that graphene remains intact. (f) LEED pattern of sample (c), showing that, after repeated cycles of silicon and oxygen intercalation, thick amorphous silica is formed. Adapted with permission from ref. 243. Copyright 2020, American Chemical Society.

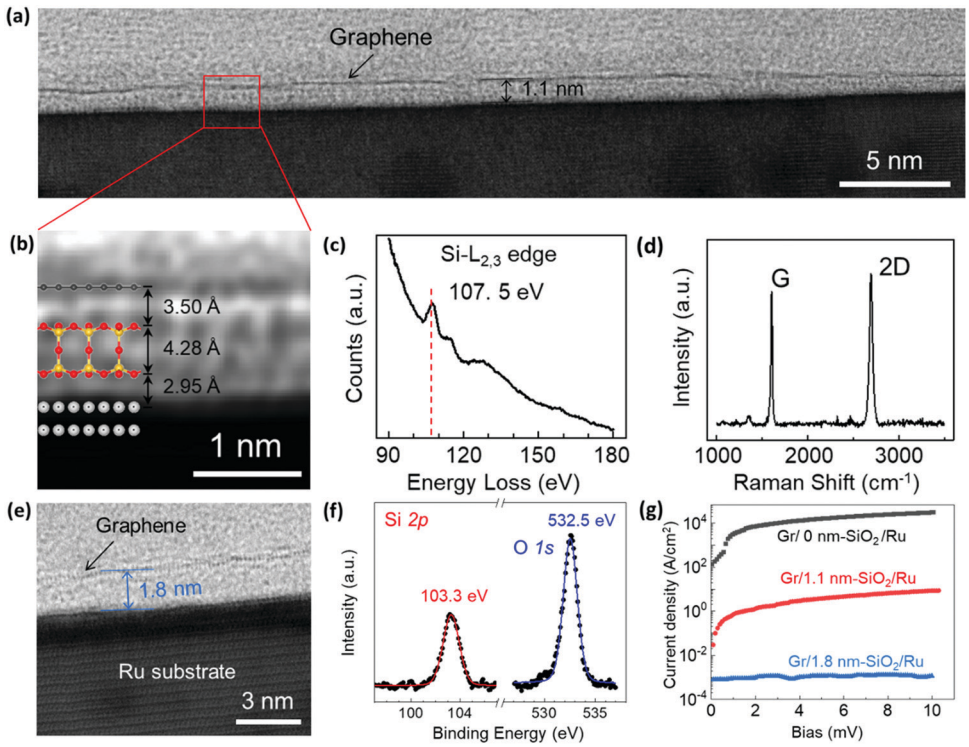

Fig. 8 Structural and elemental characterization of an intercalated silica layer. (a) Cross-sectional view of a large-scale STEM image of a G/c-silica/Ru(0001) sample, indicating the formation of a silica layer with a thickness of ~1.1 nm beneath the graphene. (b) High-resolution STEM image of interfacial silica with a superimposed theoretical atomic model of bilayer silica. (c) EELS curve of the Si-$L_{2,3}$ edge. (d) Raman spectrum of the graphene after c-silica intercalation, indicating the absence of the D-peak. (e) STEM image of the cross-section of the sample after repeated cycles of intercalation of Si and O. (f) XPS of the intercalated SiO_2 layer, showing the binding energies of the Si 2p and O 1s core levels, respectively. (g) *I–V* curves of Gr/Ru, Gr/1.1 nm-silica/Ru and Gr/1.8 nm-silica/Ru samples by vertical transport measurements at small bias (<10 mV), respectively. Adapted with permission from ref. 243. Copyright 2020, American Chemical Society.

Measurement of the vertical transport properties across the graphene and Ru(0001) substrate for Gr/Ru, Gr/1.1 nm-SiO_2 (c-silica)/Ru, and Gr/1.8 nm-SiO_2 (a-silica)/Ru indicates that the current density in the Gr/1.8 nm-SiO_2/Ru sample is as low as $\sim 10^{-4}$–10^{-3} A cm^{-2} (Fig. 8(g)), which is three orders of magnitude lower than that of Gr/1.1 nm-SiO_2 (c-silica)/Ru (~ 10 A cm^{-2}) and even four orders of magnitude lower than that of Gr/Ru ($\sim 10^4$ A cm^{-2}). The transmission coefficients of

the Gr/1.1 nm-SiO_2/Ru and Gr/1.8 nm-SiO_2/Ru samples calculated by DFT further verified the electrically insulating quality of the intercalated SiO_2 layers.

3.3 SdH oscillations and quantum Hall effects in centimeter-scale and single-crystal graphene

The successful insulation of graphene from metal Ru substrates has enabled the *in situ* fabrication of Hall bar devices on epitaxially grown graphene.[243] Shubnikov–de Haas (SdH) oscillations and quantum Hall effects represent the intrinsic electronic properties of 2D gas and Dirac Fermions in graphene.[221,222] As shown in Fig. 9(a), the measured longitudinal magnetoresistances (R_{xx}) on the *in situ* fabricated graphene Hall bar devices at different temperatures clearly show the presence of SdH oscillations. When the longitudinal magnetoresistance (R_{xx}) and Hall resistance (R_{xy}) are plotted in the same curve (Fig. 9(b)), R_{xy} exhibits a series of Hall plateaus at the positions R_{xx} shows minima and the quantized values of these plateaus match well with the Landau levels of graphene, which indicates the presence of an integer quantum Hall effect.[222] The Landau level fan diagram plotted with the Landau level index (n) against the inverse of the magnetic field ($1/B$) where the R_{xx} shows minima (maxima) is shown in Fig. 9(c). Linear fitting of this curve results in an intercept of the n-index axis close to 0.5, revealing strong evidence of a Berry phase of π of Dirac fermions in the graphene.[222] The cyclotron mass of graphene (m_c) can be extracted as $\sim 0.06\ m_e$ (where m_e is free electron mass) by fitting the amplitudes of the SdH oscillations with semi-classical fitting (as shown in Fig. 9(d)), which agrees well with that of mechanically exfoliated

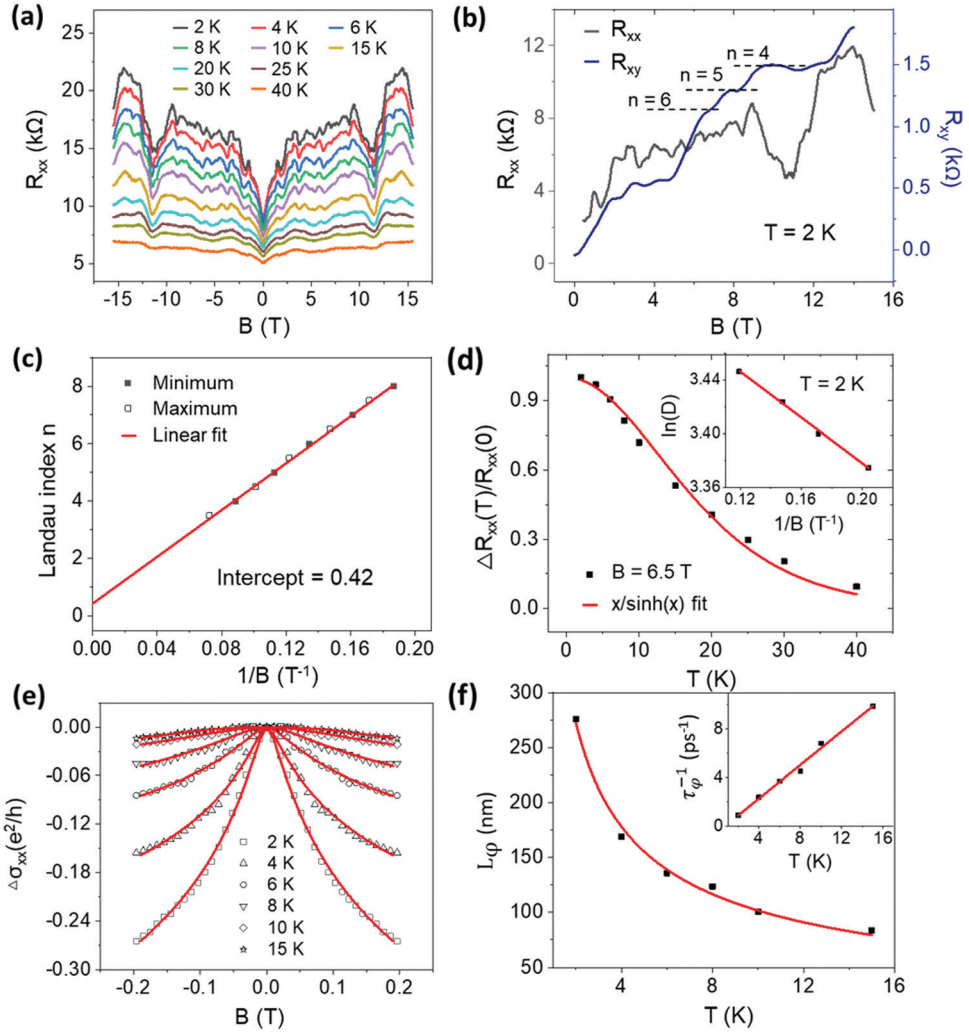

Fig. 9 SdH oscillations and quantum Hall effects in centimeter-scale and single-crystal graphene. (a) Magnetoresistances (R_{xx}) at different temperatures, showing the presence of SdH oscillations. (b) SdH oscillations in magnetoresistance R_{xx} (black) and quantum Hall effects in Hall resistance R_{xy} (blue) at 2 K. (c) Landau-level filling factors (n) as a function of the inverse of the magnetic field ($1/B$). Linear fitting of the curve gives an intercept close to 0.5, indicating a Berry phase of π. (d) Normalized amplitude of oscillations as a function of temperature. The inset shows a Dingle plot. (e) Temperature-dependent low-field magnetoconductivity ($\Delta\sigma_{xx}$) as a function of magnetic field, showing the appearance of a weak antilocalization effect. (f) Extracted power law dependence of phase coherence length L_ϕ and linear dependence of the scattering rate τ_φ^{-1} (inset) on temperature. Adapted with permission from ref. 243. Copyright 2020, American Chemical Society.

graphene.[221] The carrier mobility of $\sim$8500 $cm^2 V^{-1} s^{-1}$ can be estimated after extracting the lifetime from the Dingle plot shown in the inset of Fig. 9(d), which is larger than that of graphene directly grown on dielectrics.[119–121]

The weak (anti-)localization effect represented by quantum corrections to the low-field magnetoresistance (R_{xx}) can be used as a direct probe for measuring the quantum interference effect of epitaxial graphene during electron transport.[245,246] The weak antilocalization effect in epitaxial graphene is characterized by the cusp feature of R_{xx} under low magnetic fields, which is broadened and finally vanishes with increased temperatures, as shown in Fig. 9(e). The magnetic-field dependent magnetoconductivity ($\Delta\sigma_{xx}$) at different temperatures shown in Fig. 9(e) can be well fitted by the quantum interference theory,[247] which further confirms the presence of a weak anti-localization effect in epitaxial graphene. The extracted phase coherence length shows a clear power law dependence with an index of $-1/2$, and the scattering rate shows a linear dependence on temperature, indicating that the dominant dephasing mechanism in the epitaxial graphene is electron–electron scattering,[245] as shown in Fig. 9(f). The Berry phase of π and the weak antilocalization effect confirmed the chiral electronic nature in epitaxial graphene, suggesting the suppression of carrier scattering from short-range scatterers, such as point defects, verifying the high-quality of epitaxial graphene on SiO_2 films.

The successful development of *in situ* sample growth and device fabrication processes enables the straightforward utilization of high-quality graphene epitaxially grown on metal substrates in electronic applications. Although 1.8 nm thick amorphous SiO_2 can successfully insulate graphene from a Ru substrate, intercalation of a thicker and more uniform SiO_2 layer is highly required to fabricate field-effect transistors for future electronic device applications.

3.4 Electrical transport properties of grain-boundaries and wrinkles in millimeter-sized graphene

Millimeter-sized graphene films has been successfully grown on metal substrates by chemical vapor deposition (CVD).[115–118] However, these synthesized graphene films are polycrystalline in nature, and the presence of topological line defects of grain boundaries (GBs)/wrinkles formed during the growth or transfer process remains an obstacle to their electronic applications. Graphene GBs are mainly composed of non-ideal hexagonal rings,[135–138] such as pentagons, heptagons, and octagons. Compared with their geometric width, the electronic transition width of graphene GBs can be greatly extended to $\sim$10 nm.[133,135,137,248–250] The electronic structure near GBs is strongly perturbed,[224] resulting in the strong scattering of carriers and the degradation in carrier mobility.[133,138–141] Quantitative measurement of the degradation of electrical transport of these defects will have great implications for further applications of large-scale graphene to flexible and transparent electrodes in touch-screen panels, solar cells, *etc.* This has been demonstrated by either directly measuring the resistivity of GBs after subtracting the intrinsic resistivity of graphene from the intergrain resistivity in Hall bar devices based on an extended Drude transport model,[139,141,251] or by indirectly measuring the electronic properties of GBs through scanning probe microscopy (SPM) techniques.[136,250,252] Furthermore, the direct four-probe measurement on the resistivity and mobility of GBs by the four-probe STM technique in millimeter-sized graphene grown by CVD can retain the intrinsic electronic properties of GBs without introducing the complicated lithographic fabrication process.[133]

The sharp tips of the four-probe STM system can contact graphene noninvasively,[133,253–256] allowing for direct four-probe measurements on the transport properties of graphene GBs. Fig. 10(a–c) show the configurations of the direct-four probe measurement. By measuring the sheet resistances in individual graphene grains and intergrain sheet resistance across the GBs in the bi-crystal graphene flake, respectively, the sheet resistance of GBs can be extracted based on an extended Drude transport model, where the 1D GB is considered as an extension of the conductance channel and changed to an extended 2D area.[141] Due to the different inter-connecting ways of individual graphene grains during growth[141] or possible adsorbates attached to GBs,[137] the extracted resistivities of GBs of different bi-crystal graphene flakes deviate a lot ranging from several kΩ μm to tens of kΩ μm. The conductivity of one typical GB as a function of carrier density is shown in Fig. 10(d). The electron and hole mobilities can be extracted as $\sim$20.84 $cm^2 V^{-1} s^{-1}$ and $\sim$14.41 $cm^2 V^{-1} s^{-1}$, respectively, which indicates that due to the non-hexagonal carbon rings present in graphene GB, the carrier transport across the GB is strongly scattered. Statistics on the seven different graphene GBs show that the carrier mobility in the GB regions is decreased by over 90% compared to that of pristine graphene,[254] as shown in Fig. 10(f).

Graphene wrinkles are another kind of defect formed during the growth or transfer process[126,127] and composed of collapsed multilayer (bilayer, trilayer, or more) graphene.[128,129] These folded multi-stacked layers have much wider lateral sizes ($\sim$10 nm to several micrometers) than those of GBs and show large curvature and apparent height fluctuation,[130–132] which breaks the honeycomb lattice of graphene and introduces additional carrier scattering when electrons travel across them.[133,134,257] The sheet resistance of graphene wrinkles has been measured by direct four-probe measurement, as shown in Fig. 10(e). Based on the same method as that for graphene GBs, the carrier mobility in the wrinkle regions can also be extracted. Fig. 10(f) shows the carrier mobilities of two typical graphene wrinkles. Compared to those of pristine graphene, both the electron and hole mobilities are reduced by 30–70%, much lower than those of graphene GBs. However, when measuring the electrical transport properties along the graphene wrinkles, they show a much higher conductivity of up to $\sim$33.6 times compared to that of the flat pristine graphene region, revealing the formation of highly conductive channels induced by graphene wrinkles.[132]

Graphene GBs and wrinkles, which act as local carrier scatterers, have severely degraded the local electrical properties of millimeter-sized graphene. However, when measuring the local electrical transport properties of graphene in the region

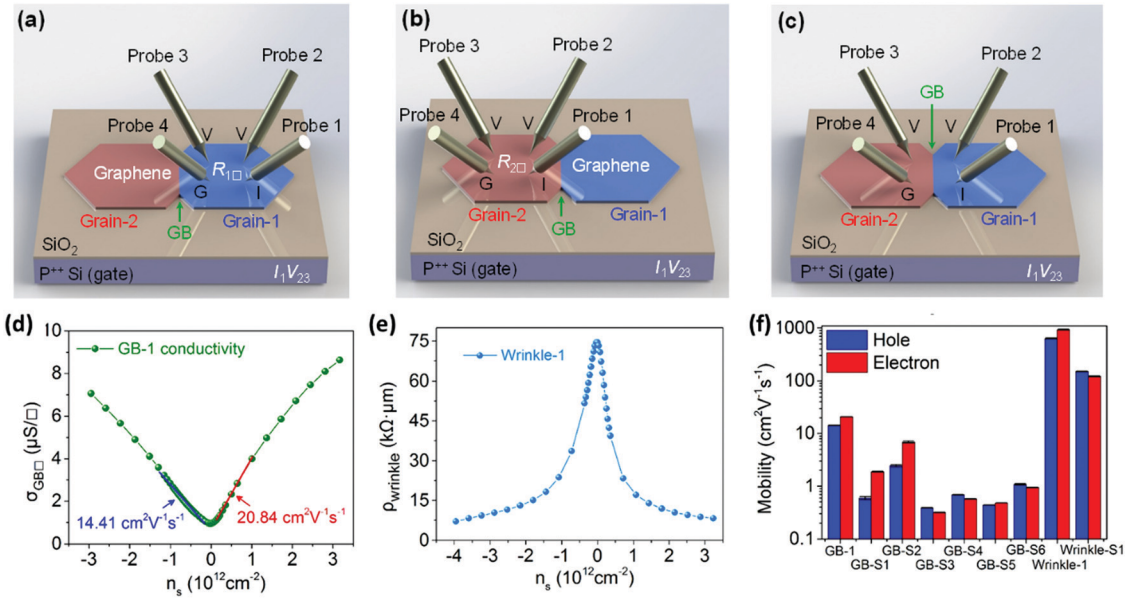

Fig. 10 (a–c) Schematic diagrams of *in situ* four-probe transport measurement on graphene after being transferred to a SiO_2/Si substrate. (a and b) Four-probe transport measurements on the two grains of a bi-crystal graphene flake on the SiO_2/Si substrate, respectively. (c) Four-probe transport measurement crossing the GB. (d) Carrier-density-dependent conductivity of GB of the bi-crystal graphene flake. The carrier mobility of electrons and holes can be extracted as ~20.84 and ~14.41 $cm^2 V^{-1} s^{-1}$, respectively. (e) Extracted resistivity of the graphene wrinkle as a function of carrier density. (f) Statistics of carrier mobility extracted from different graphene GBs and wrinkles. Adapted with permission from ref. 133. Copyright 2017, American Chemical Society.

far away from these imperfections,[255] such as GBs, wrinkles, multilayered islands, cracks, holes, and adsorbates, these imperfections have little degradation effect, suggesting the local nature of these imperfections. The impact of these imperfections to the whole graphene films has been studied by performing angle-dependent van der Pauw measurements.[255] Surprisingly, the measurements show that if the imperfections are not extended over the whole graphene film, the electrical homogeneity of the graphene film is not apparently influenced because the carriers can find the travelling path with least resistance by themselves.[258] From the perspective of practical applications of large-scale graphene, such as photodetectors and chemical sensors, the electrical uniformity and homogeneity of the devices can be guaranteed as long as these imperfections are found only in very local regions without extending to the entire graphene film.

4. Electrical transport properties of magnetic transition metal dichalcogenides

Beyond graphene, transition metal dichalcogenides (TMDCs) with the chemical formula of MX_2,[110,142] in which M stands for transition metals (such as Mo, W, Nb, V, and Cr) and X stands for chalcogen elements (such as S, Se, and Te), emerge as a family of materials with novel properties, such as thickness-dependent bandgaps,[110] strong spin–orbit coupling (SOC),[143] and valley polarization,[144] making them attract extensive research attention in not only their novel physical properties[145] but also their applications for nanoelectronics and nanophotonics.[146] In monolayer transition metal dichalcogenides, the inversion symmetry is broken and the strong SOC will induce degeneration of valley-locked spin-split,[145,147] allowing for control of the spin and valley polarization states for next generation spintronic and valleytronic devices.[144,148–150] Moreover, the experimental discovery of intrinsic ferromagnetism in mono- or few-layered CrI_3,[151] $Cr_2Ge_2Te_6$,[152] and VSe_2[153] has ignited intense exploitation of 2D magnetism in TMDCs.[154–156] For example, intrinsic ferromagnetism has been theoretically predicted in monolayer vanadium-based TMDCs (VX_2, X = S, Se, Te),[259–261] which breaks the time reversal symmetry and the degeneracy of two valleys, resulting in valley polarization induced by SOC.[262,263] The experimental observation of strong room-temperature ferromagnetism in monolayer VSe_2 epitaxially grown on HOPG and MoS_2[153] stimulated the study of the evolution of magnetic and electronic properties with thickness due to the paramagnetic nature of bulk VSe_2.[264,265] To reveal their transport signatures of magnetic and electronic properties with reduced thickness, high quality samples with tunable thickness grown on dielectric substrates are required. A sublimed-salt-assisted chemical vapor deposition (CVD) method has been successfully developed to grow few-layered V-based chalcogenides,[266,267] such as VS_2, VSe_2, and VTe_2, providing a promising route to study the transport features in the evolution of magnetic order with reduced thickness, interlayer stacking order, and other competing and coexisting ordered electronic states.[156] Beyond vanadium-based chalcogenides, few-layered cobalt-based chalcogenides (CoS_2, $CoSe_2$, and $CoTe_2$) have also been successfully grown on SiO_2/Si substrates by the CVD method using NaCl as the fluxing agent.[268] Magnetotransport measurements on these CoX_2 (X = Se, Te) nanoflakes revealed their metallic transport nature and nonsaturated and linear

magnetoresistance under magnetic fields up to 9 T. Paramagnetic order has been observed for CoX_2 nanoflakes with a broad range of thicknesses. As for chromium-based chalcogenides, such as $CrSe_2$[269] and $CrTe_2$,[270,271] mono- or few-layered samples have also been successfully grown on various substrates. Due to their strong magnetic anisotropy,[272] robust near room temperature ferromagnetism has been observed,[269–271,273] which provides a great avenue for future 2D magnet based spintronic applications.

4.1 Sublimed-salt-assisted growth of high-quality 2D magnetic transition metal dichalcogenides by chemical vapor deposition (CVD)

A sublimed-salt assisted CVD method has been successfully developed to grow high-quality TMDCs with tunable thickness,[266,274,275] in which ammonium chloride (NH_4Cl) was used as fluxing medium and the range of growth temperatures can be drastically shrunken to 400–500 °C compared to that prepared using vanadium chloride as reacting precursors.[276] The thickness of as-grown VSe_2 nanoflakes increases with temperature monotonically, as shown in Fig. 11(a). The thinnest VSe_2 nanoflake is 2.48 nm thick (Fig. 11(b)). The X-ray diffraction pattern of the as-grown VSe_2 flakes matches well with that of the 1T phase of VSe_2 (Fig. 11(d)). The Raman spectrum collected on a 4.2 nm thick VSe_2 flake shows two prominent peaks located at 207 and 139 cm^{-1}, respectively (Fig. 11(c)), which can be assigned to the out-of-plane A_{1g} mode and in-plane E_g mode of 1T-VSe_2.[277] Mapping the A_{1g} peak on the entire VSe_2 flake indicates a uniform contrast (inset in Fig. 11(c)). Fig. 11(e) shows a low-magnification TEM image of the VSe_2 flake. The inset shows the SAED pattern, which is in agreement with that of the 1T-VSe_2. The atomically resolved STEM image shown in Fig. 11(f) reveals the defect-free crystal lattices of 1T-VSe_2. Using this sublimed-salt-assisted CVD method, not only vanadium-based dichalcogenides, such as VS_2, VSe_2, and VTe_2, but also tungsten-based dichalcogenides, such as WSe_2, have been successfully grown on various dielectric substrates, including SiO_2/Si and flexible polyimide (PI).[266]

4.2 Magnetotransport properties of few-layered VSe_2 flakes. The successful growth of VSe_2 crystals on dielectric substrates with tunable thickness enables the study of their thickness-dependent transport properties.[266,276] Fig. 12(a) shows the temperature-dependent resistivity (ρ–T) of VSe_2 flakes with different thicknesses of 28 and 20 nm (bulk-like), 9.6, 6.0, and 5.5 nm (intermediate thick), and 4.6 nm (thinnest), respectively. The resistivities of all VSe_2 flakes monotonically decrease with decreasing temperature, indicating their metallic transport nature. The minima of the first derivatives of the resistivities with respect to temperatures ($d\rho/dT$) shown in Fig. 12(b) are due to the formation of charge density waves (CDWs), and T_{CDW} decreases monotonically with decreasing thickness[276–278] (Fig. 12(c)), revealing that the CDW state is preferably present in the 3D bulk due to strong interlayer coupling.[266,278,279] The high crystalline quality of the as-grown VSe_2 flakes is reflected in the large residual resistivity ratio (RRR, RRR = ρ_{300K}/ρ_{2K}), which ranges from 5 to 23, which is almost the largest compared to previous results.[276,278] As shown in Fig. 12(d and e), for VSe_2 flakes thicker than 5 nm, applying magnetic fields does not change the transport behavior except for the increase of resistivity. On the other hand, for the 4.6 nm thick VSe_2 flake, an upturn in the resistivity emerges at low temperatures, and after applying different magnetic fields, the resistivity upturn persists (Fig. 12(f)),

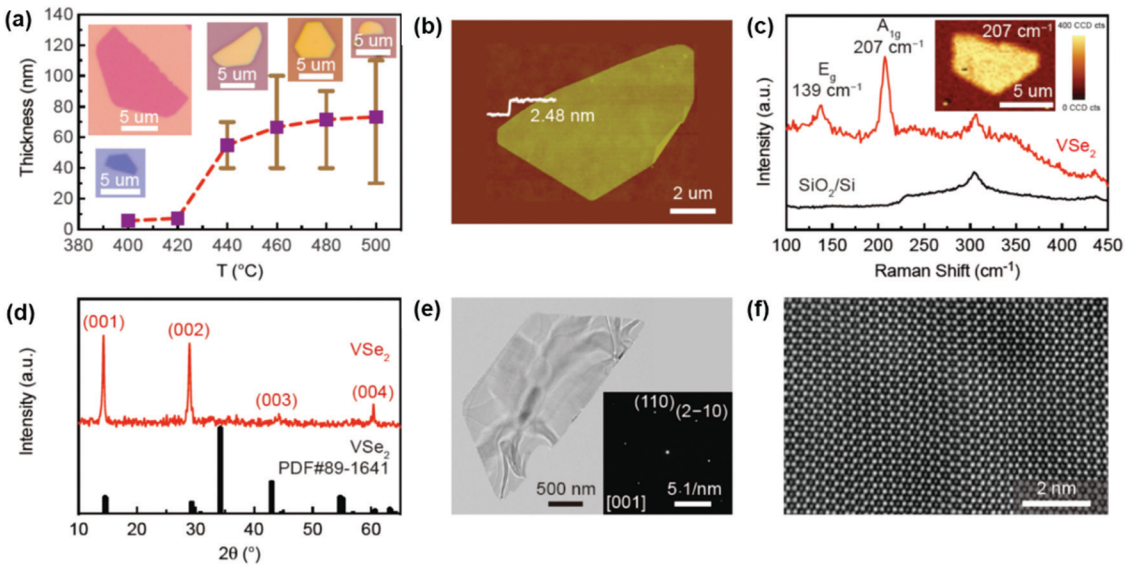

Fig. 11 CVD growth of high-quality VSe_2 nanosheets with tunable thickness. (a) Evolution of the thickness of VSe_2 nanosheets with growth temperature. (b) AFM image of a VSe_2 nanosheet with a thickness of 2.48 nm. (c) Raman spectrum of a VSe_2 nanosheet with a thickness of 4.2 nm, showing E_g and A_{1g} peaks located at ~139 cm^{-1} and ~207 cm^{-1}, respectively. The inset shows the mapping of the A_{1g} peak at ~207 cm^{-1}. (d) XRD spectrum of the as-grown VSe_2 nanosheets. (e and f) Low magnification and lattice-resolved transmission electron microscope (TEM) images of a VSe_2 nanosheet, respectively. The inset in (e) shows the selected-area electron diffraction (SAED) pattern. Adapted with permission from ref. 266. Copyright 2019, American Chemical Society.

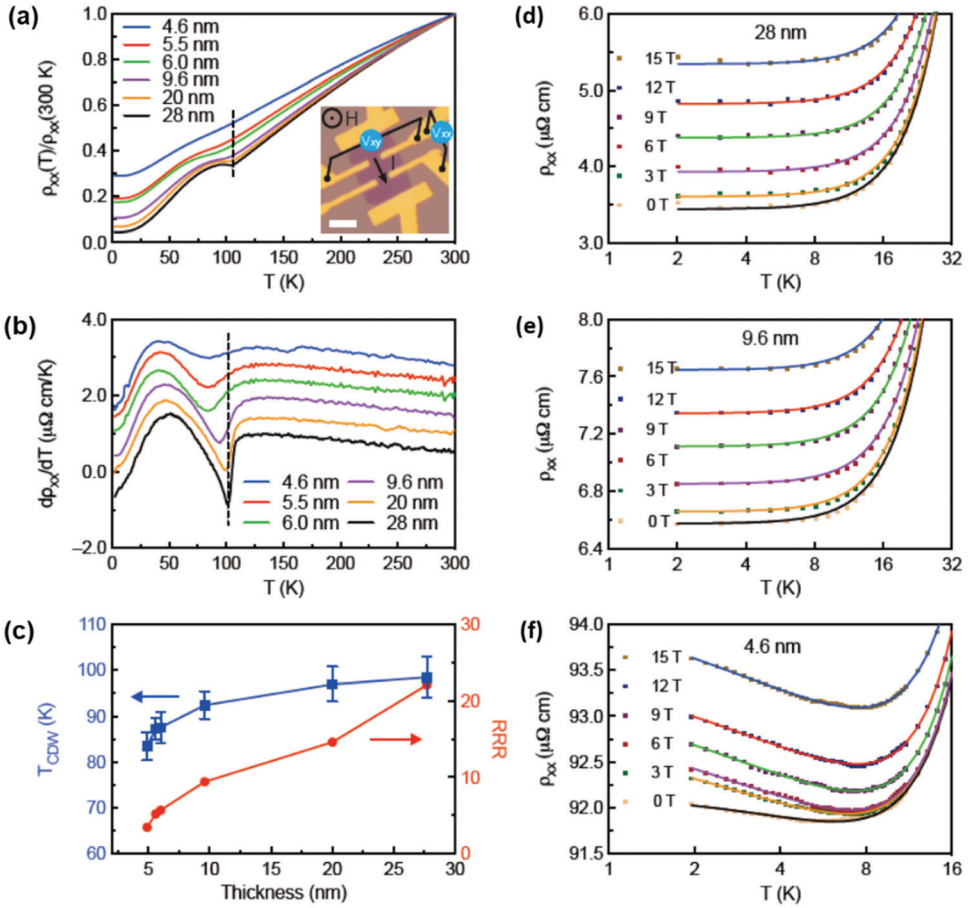

Fig. 12 Resistivity of VSe_2 nanosheets with different thicknesses. (a) Longitudinal resistivity (normalized) and (b) first derivatives of the resistivities of VSe_2 nanosheets with different thicknesses at different temperatures. The charge-density wave (CDW) transition temperature (T_{CDW}) is defined by the minimum of the first derivative of resistivity. The inset in (a) shows the optical image of one typical Hall bar device. Scale bar, 5 μm. (c) T_{CDW} and residual resistivity ratio (RRR = ρ_{300K}/ρ_{2K}) as a function of temperature. (d–f) Logarithmic temperature-dependent resistivity of the 28 nm (d), 9.6 nm (e), and 4.6 nm (f) thick VSe_2 nanosheets under different magnetic fields, respectively. Adapted with permission from ref. 266. Copyright 2019, American Chemical Society.

indicating the emergence of electron–electron (e–e) interactions instead of a weak localization effect[280,281] or the Kondo effect.[282] The e–e interactions will contribute to the temperature-dependent resistivity with additional terms in logarithmic form for 2D transport or power law form for 3D transport.[283] The agreement of fitting curves with experimental data shown in Fig. 12(d–f) indicates that with reduced thickness, the e–e interactions are greatly enhanced and the transport nature of VSe_2 is transformed from 3D to 2D, which coincides with the theoretical predications.[284]

Fig. 13(a) shows the magnetoconductance ($\Delta\sigma_{xx}$) as a function of magnetic field at different temperatures, in which the cusps coming from the weak antilocalization (WAL) effect can persist at temperatures up to 10 K. These cusps under magnetic fields below 2 T fit well with Hikami–Larkin–Nagaoka (HLN) theory,[285] as shown in Fig. 13(b). Fig. 13(c) shows the extracted characteristic dephasing field (B_ϕ) and spin–orbit scattering field (B_{SO}) as a function of temperature. B_{SO} is much larger than B_ϕ at all temperatures, revealing that the dephasing mechanism is Nyquist e–e interactions instead of electron–phonon interactions,[283] which is further verified by the inverse square root temperature dependence of phase coherent length (l_ϕ), as shown in Fig. 13(d). The spin–orbit scattering length (l_{SO}) remains constant and is much smaller than l_ϕ, further confirming the enhanced SOC in the 4.6 nm thick VSe_2 flake. The observation of the WAL effect in the 4.5 nm thick VSe_2 flake indicates that with continuous reduced thickness, the quantum confinement effect drives the transformation of the 3D electronic band structure of bulk VSe_2 to a quasi-2D one. With improved growth of VSe_2 flakes by the sublimed-salt-assisted CVD method, monolayer VSe_2 flakes are believed to be obtained, providing a unique platform to study the interplay of collective ordered states, such as valley polarization, spin polarization, and strong SOC, for spintronics and valleytronics applications.

4.3 Kondo effect in mutilayered VTe_2. Vanadium ions tend to intercalate into the van der Waals gap of vanadium-based dichalcogenides, and by this way local magnetic moments are introduced, which can be used to tune the magnetic ordered states in vanadium-based dichalcogenides.[286,287] For bulk VSe_2,

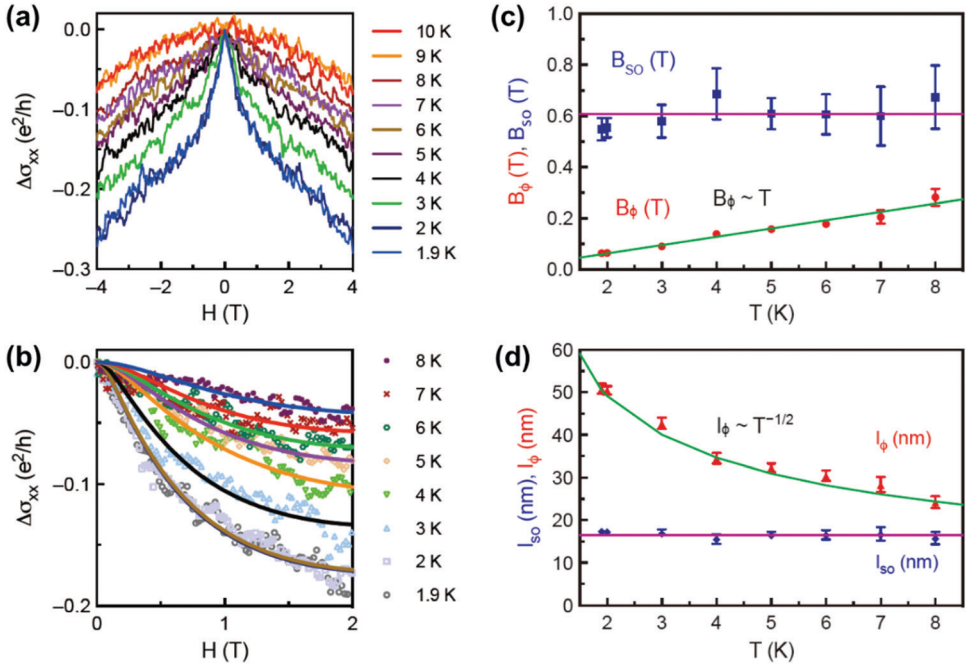

Fig. 13 Observation of a WAL effect in the 4.6 nm thick VSe_2 nanoflake. (a) Magnetic-field-dependent magnetoconductance ($\Delta\sigma_{xx}$) at temperatures below 10 K. (b) Fitting $\Delta\sigma_{xx}$ below 10 K with Hikami–Larkin–Nagaoka (HLN) theory. (c) HLN fitting extracted characteristic dephasing field (B_ϕ) and spin–orbit scattering field (B_{SO}). (d) HLN fitting extracted phase coherence length (l_ϕ) and spin–orbit scattering length (l_{SO}). Adapted with permission from ref. 266. Copyright 2019, American Chemical Society.

the magnetic properties are induced by the intercalated vanadium ions;[264,286] as a result, the Kondo effect has been observed.[282] On the other hand, for VS_2, after intercalation of vanadium ions, a lattice with the chemical formula of V_5S_8 is formed, leading to antiferromagnetism in the bulk and weak ferromagnetism when reduced to nanothick layers.[288,289] For VTe_2, intercalation of a trace amount of vanadium ions gives rise to the observation of the Kondo effect in multilayered VTe_2 plates.[267]

Fig. 14(a) shows the temperature-dependent resistivity of multilayered VTe_2 plates. In the whole temperature range, the resistivity decreases with decreasing temperature, indicating their metallic transport behavior. The residual resistivity ratio (RRR, defined as ρ_{300K}/ρ_{2K}) is 4.58, which is higher than that of VTe_2 single crystals,[287] suggesting the presence of intercalated vanadium ions.[267] At low temperatures, the resistivity shows an upturn, which can be gradually suppressed with increasing magnetic field, indicating that the Kondo effect or weak localization effect occurs in the VTe_2 nanoplates, as shown in Fig. 14(b). The presence of the Kondo effect can be confirmed by measuring the MRs at different temperatures under both vertical and parallel magnetic fields. The MRs show almost the same negative to positive MR transition behavior under both the vertical (Fig. 14(c)) and parallel (Fig. 14(d)) magnetic fields, from which weak localization behavior can be safely ruled out because it can be observed only under vertical magnetic fields.[280] Fig. 14(e) shows that both the vertical and parallel negative MRs are almost the same and quadratically dependent on magnetic fields. However, at 20 K, the positive MRs under the parallel magnetic fields vanish, as shown in Fig. 14(f), which reveals the isotropic nature of the negative MRs and further confirms the presence of the Kondo effect. The resistivity upturn can be fitted using the Hamann expression,[290] and a Kondo temperature (T_K) of ~6.2 K and a spin of magnetic impurities (S) of ~0.12 can be extracted. However, the resistivity upturn under different magnetic fields can be well fitted by a modified Hamann expression in which a Brillouin function with $S = 1/2$ is added.[291] The origin of the Kondo effect was attributed to the presence of the localized magnetic moment from intercalated V atoms, which was verified by DFT calculations. All the above results indicate that by intercalating VX_2 or other TMDCs with vanadium or other magnetic ions, the magnetic properties of VX_2 or TMDCs will change drastically, providing a rich material platform to study the Kondo effect, magnetic ordered states, correlation effects, and many-body physics in 2D TMDCs.

4.4 Linear magnetoresistance in $CoSe_2$ and $CoTe_2$ nanosheets

Ferromagnetism with a Curie temperature of 124 K has been observed in the non-layered pyrite-type cubic structure of CoS_2 single crystals.[292] However, for $CoSe_2$ with a similar crystal and electronic structure,[293,294] Pauli paramagnetism has been observed.[292] Measurement of the electrical transport properties on $CoTe_2$ nanosheets with tunable thickness revealed excellent electrical conductivities up to 4.0×10^5 S m^{-1} with a strong thickness dependence.[295] Due to the Na^+ intercalation into the lattice of $CoTe_2$ nanorods during the hydrothermal growth process, paramagnetic behavior has been observed in $CoTe_2$ nanorods.[296] The recent successful growth of $CoSe_2$ and $CoTe_2$

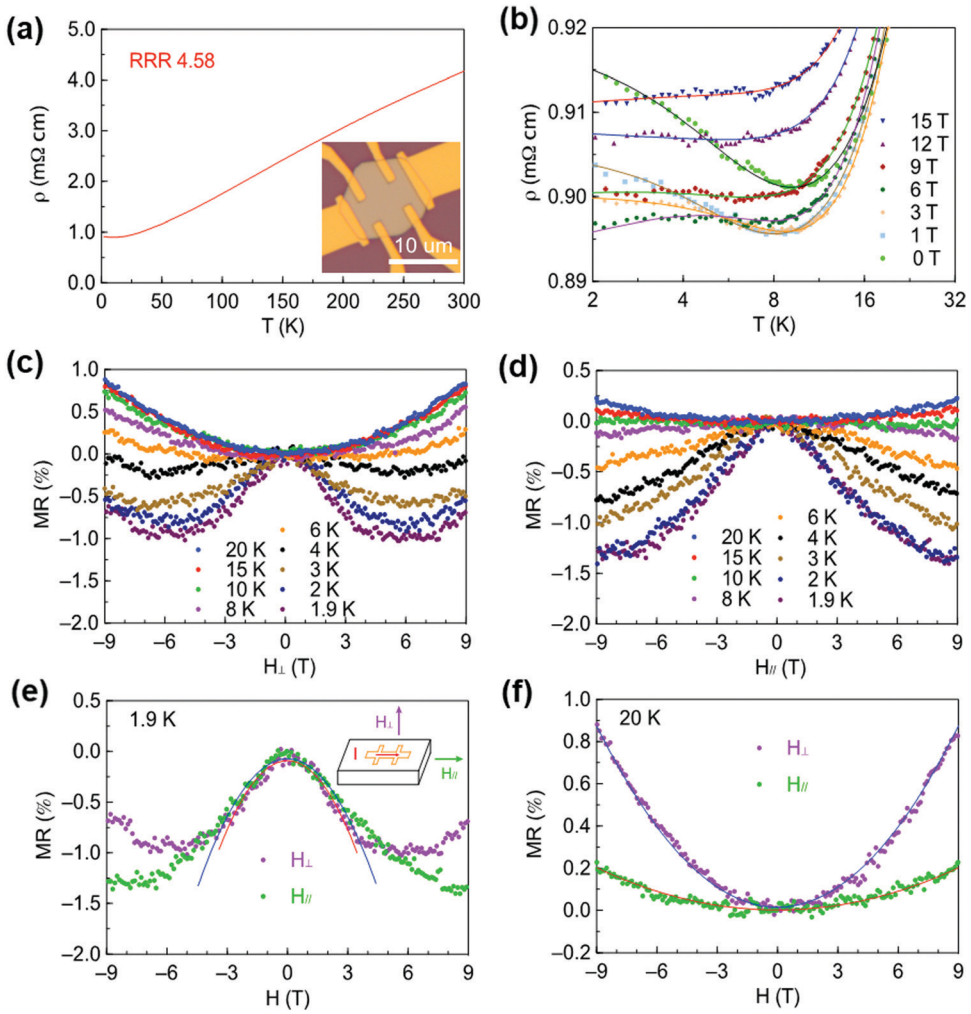

Fig. 14 Resistivity of multilayer VTe_2 nanoplates at different temperatures and magnetic fields. (a) Resistivity of multilayer VTe_2 nanoplates as a function of temperature. The inset shows the optical image of a typical Hall bar device based on VTe_2 nanoplates. (b) Temperature-dependent resistivity values under different magnetic fields (with temperature on a logarithmic scale). Magnetoresistances (MRs) at different temperatures under the vertical (c) and parallel (d) magnetic fields with respect to the plane of the sample, respectively. Vertical and parallel MRs with low magnetic fields fit at 1.9 K (e) and 20 K (f), respectively. Adapted with permission from ref. 267. Copyright 2019, American Chemical Society.

nanosheets with thicknesses ranging from 1.18 to 20 nm enables the study of their thickness-dependent electrical transport properties.[268]

Fig. 15(a) schematically shows the typical Hall bar devices made on $CoSe_2$ and $CoTe_2$ nanosheets. Fig. 15(b and c) show the temperature-dependent resistivity of $CoSe_2$ and $CoTe_2$ nanosheets, respectively. When the temperature is decreased from 300 to 2 K, the resistivity shows a monotonic decrease, indicating the metallic transport nature of $CoSe_2$ and $CoTe_2$ nanosheets. The magnetoresistances of $CoSe_2$ and $CoTe_2$ nanosheets with magnetic fields from 0 to 9 T show a linear dependence on the magnetic field at 2 K, as shown in Fig. 15(d and f), respectively. With the temperature increasing to ~20 K, the linear dependence (MR $\propto B$) is transformed to a conventional parabolic dependence (MR $\propto B^2$). The origin of linear MR was attributed to the uneven distribution of conductivity or disorder in the symmetry.[297] The linear dependence of the Hall resistance of $CoSe_2$ and $CoTe_2$ nanosheets on magnetic fields shown in Fig. 15(e) and (g), respectively, suggests that no ferromagnetic or antiferromagnetic order has been observed in $CoSe_2$ and $CoTe_2$ nanosheets. Compared with typical conductive 2D materials, bulk materials and conventional metals, the electrical conductivity of $CoSe_2$ and $CoTe_2$ reaches 5×10^6 and 1.8×10^6 S m^{-1}, respectively, close to that of silver, suggesting their potential application in 2D conductors, as shown in Fig. 15(h). Three devices of $CoTe_2$ nanosheets with typical thicknesses of 4, 7, and 13 nm were selected to study their thickness-dependent magnetotransport properties. As shown in Fig. 15(i), the magnitude of the linear MR at 2 K increases with reduced thickness, while the conductivity remains ~10^6 S m^{-1}, showing a weak thickness dependence. To reveal the electronic properties, magnetic order, and even quantum confinement effect in thin CoX_2 crystals, a more detailed study of thickness-dependent properties is required.

4.5 Anomalous thickness-dependent Curie temperature in air-stable 2D ferromagnetic 1T-$CrTe_2$. One key challenge in

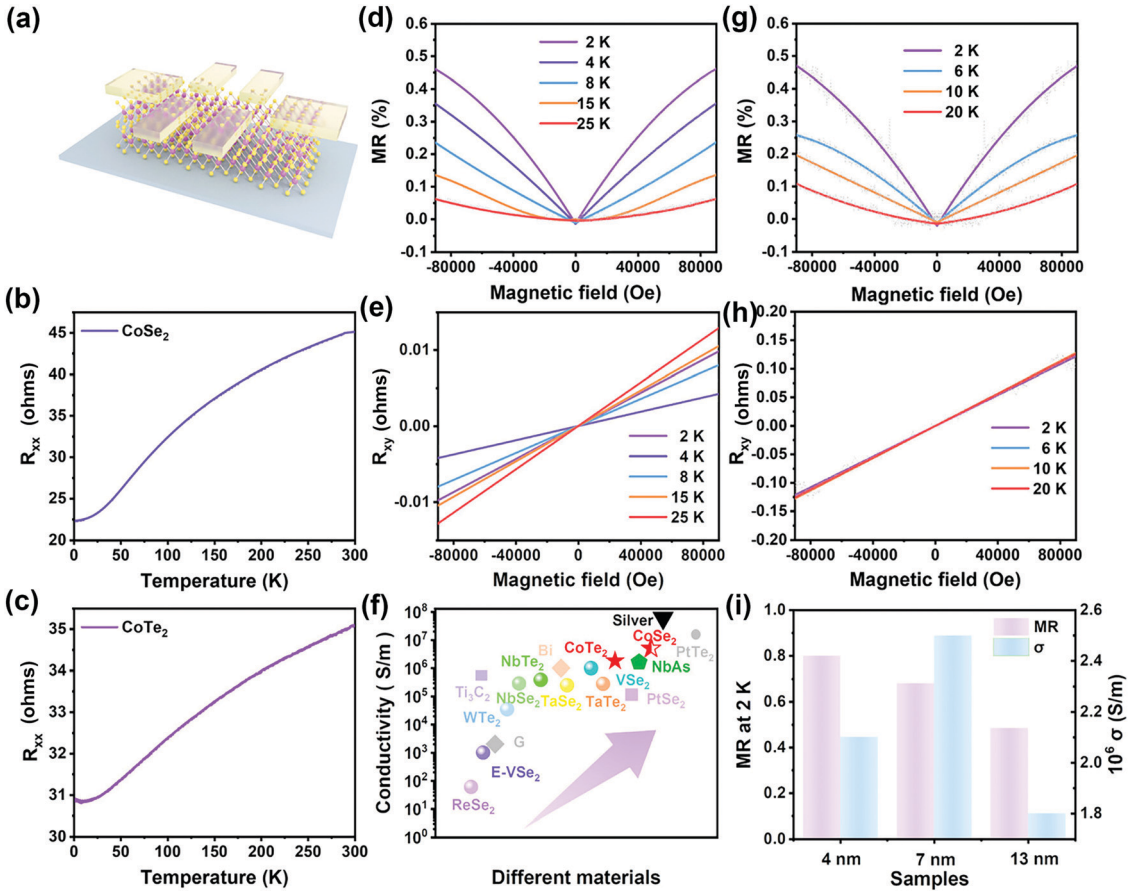

Fig. 15 Linear magnetoresistance in $CoSe_2$ and $CoTe_2$ nanosheets. (a) Schematic diagram of typical Hall bar devices made on $CoSe_2$ and $CoTe_2$ nanosheets. (b and c) Temperature-dependent resistivity of $CoSe_2$ and $CoTe_2$ nanoflakes from 300 K to 2 K, respectively. (d and f) The magnetoresistance (MR) ratios of $CoSe_2$ and $CoTe_2$ nanosheets at different temperatures, respectively. (e and g) Hall resistance (R_{xy}) curves of $CoSe_2$ and $CoTe_2$ nanoflakes at different temperatures, respectively. (h) Compared with typical conductive 2D materials, bulk materials and conventional metals, both $CoSe_2$ and $CoTe_2$ show very high conductivity close to that of silver. (i) MR at 2 K and conductivity of $CoTe_2$ nanosheets with various thicknesses. Adapted with permission from ref. 268. Copyright 2020, American Chemical Society.

studying the critical behavior and evolution of magnetic order with reduced thickness in 2D magnetic materials is their poor environmental stability. When exposed to air, many atomically thin 2D magnetic materials will rapidly degrade, such as CrI_3,[151] VSe_2,[153] and $Cr_2Ge_2Te_6$.[152] Monolayer 1T-$CrTe_2$ was theoretically predicted to be ferromagnetic,[298] and ferromagnetic order has been confirmed in both bulk crystals[299] and mechanically exfoliated few-layered nanosheets[300] with a high Curie temperature of ~310 K. Recently, mono- and few-layered 1T-$CrTe_2$ nanoflakes have been grown on SiO_2/Si substrates by a facile CVD method.[301] Raman spectroscopy characterization indicated that after being exposed to the ambient environment for 5 days the 1T-$CrTe_2$ nanoflakes still preserved their high crystallinity, suggesting the good air stability of 1T-$CrTe_2$ ultrathin crystals, which is a leap forward step towards the utilization of 2D magnets in future spintronic devices.

The long-range ferromagnetic order in 1T-$CrTe_2$ nanoflakes was confirmed by the robust magnetization hysteresis loop (M–H curve) under both vertical and parallel magnetic fields with respect to the crystalline plane at various temperatures. When reducing the thickness of the 1T-$CrTe_2$ nanoflakes to below 10 nm, a magnetization hysteresis loop was only observed under the vertical magnetic fields, indicating that the easy-axis changes to along the out-of-plane direction. The Curie temperature shows an anomalous monotonic increase when reducing the thickness from ~130 to 7.6 nm. This was also verified by the magnetotransport and polar reflective magnetic circular dichroism (RMCD) spectroscopy measurements on 1T-$CrTe_2$ nanoflakes with different thicknesses. An apparent kink at ~200 K was observed in the temperature-dependent resistivity, indicating a magnetic transition from paramagnetism to ferromagnetism.

Fig. 16(a) shows the Hall resistance of a 10 nm thick 1T-$CrTe_2$ nanoflake at various temperatures. A clear hysteresis loop due to the presence of an anomalous Hall effect is observed, which persists up to 200 K. The coercive field can reach ~1 T at 2 K and decreases with temperature, while the saturated zero-field Hall resistance remains the same for temperatures ranging from 2 to 170 K, indicating robust ferromagnetism. The spin flip process was also observed in the butterfly-shape hysteresis behavior in the magnetoresistance

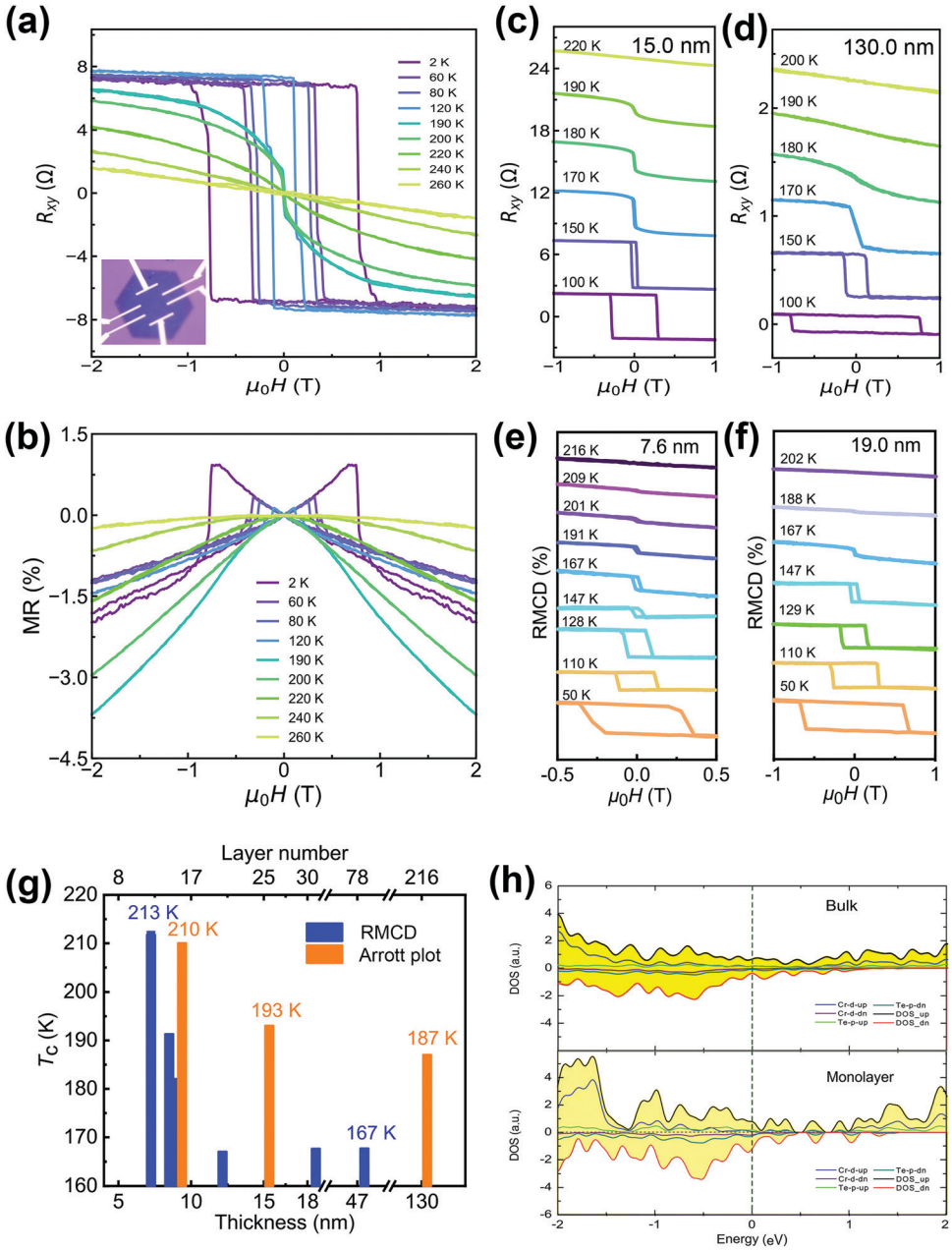

Fig. 16 Magneto-transport properties and polar RMCD spectra of 1T-$CrTe_2$ nanoflakes. (a and b) Hall resistance and magnetoresistance as a function of magnetic field in a 10.0 nm thick 1T-$CrTe_2$ nanoflake. The inset shows the optical image of the Hall device. (c and d) Hall resistance of 15.0 and 130.0 nm thick 1T-$CrTe_2$ nanoflakes at various temperatures, respectively. (e and f) RMCD spectra of 7.6 and 19.0 nm thick 1T-$CrTe_2$ nanoflakes as a function of out-of-plane magnetic field at different temperatures, respectively. (g) Thickness-dependence of the Curie temperature (T_c) of 1T-$CrTe_2$. Blue and orange columns represent the T_c values extracted from the RMCD and Arrott plots, respectively. (h) Density of states (DOS) for monolayer and bulk 1T-$CrTe_2$ calculated by DFT, respectively. The green dotted line indicates the calculated Fermi levels. Adapted with permission from ref. 301. Copyright 2021, Springer Nature.

curves shown in Fig. 16(b). Fig. 16(c and d) display the Hall resistance of 15.0 and 130.0 nm thick 1T-$CrTe_2$ nanoflakes, respectively. The T_c value of the 15.0 nm thick sample is ~193 K, which is higher than ~187 K of the 130.0 nm thick sample. For the 10.0 nm thick sample, the T_c value increases to ~210 K, suggesting an enhanced T_c with reduced thickness. The polar RMCD spectra of 7.6 and 19.0 nm thick 1T-$CrTe_2$ nanoflakes are shown in Fig. 16(e) and (f), respectively. For the 7.6 nm thick sample, the T_c value extracted from the RMCD spectrum is ~212 K, while for the 19.0 nm thick sample, T_c is reduced to ~167 K, also indicating enhanced T_c with reduced thickness. Fig. 16(g) summarizes the T_c values of 1T-$CrTe_2$ nanoflakes with different thicknesses extracted from both Arrott plots and RMCD spectra, revealing an anomalous thickness dependence of the T_c. The possible itinerant ferromagnetic properties in 1T-$CrTe_2$ were revealed by the partial

occupation of d orbitals of Cr atoms in the calculated density of states (DOS) for both bulk and T-$CrTe_2$ samples, as shown in Fig. 16(f). Towards their application for future room-temperature spintronic devices, an in-plane room-temperature negative anisotropic magnetoresistance (AMR) was obtained in devices based on 1T-$CrTe_2$ ultrathin crystals and a sign change in AMR was observed at lower temperature with −0.6% and +5% at 300 and 10 K, respectively.[300]

5. Construction of nanoscale electronic devices based on 2D semiconductors

In the past decades, two-dimensional (2D) semiconductors have attracted tremendous attention due to their atomically thin thickness and the confinement of electron transport to the 2D plane, enabling their high carrier mobility even at the 2D limit and facilitating the continuous channel length scaling in transistors.[111–113,146] A large family of 2D semiconductors, such as graphene-like Xenes (black phosphorus (BP),[302] silicene[303]), transition metal dichalcogenides (TMDCs, *e.g.* MoS_2,[304] $MoSe_2$,[305] $MoTe_2$,[306] WS_2,[307] WSe_2[308]), and metal mono- and dichalcogenides (InSe,[309] SnS,[310] SnS_2,[311] $SnSe_2$[311]), have been demonstrated as alternative channel materials in field-effect transistors. However, due to their atomically thin nature, charge carriers suffer from severe scattering due to external environmental factors, such as from trapped charges and surface roughness in the dielectric substrate and adsorbates in the air.[312] By optimization of interface properties, such as channel–contact interfaces[313,314] and channel–dielectric interfaces,[315]

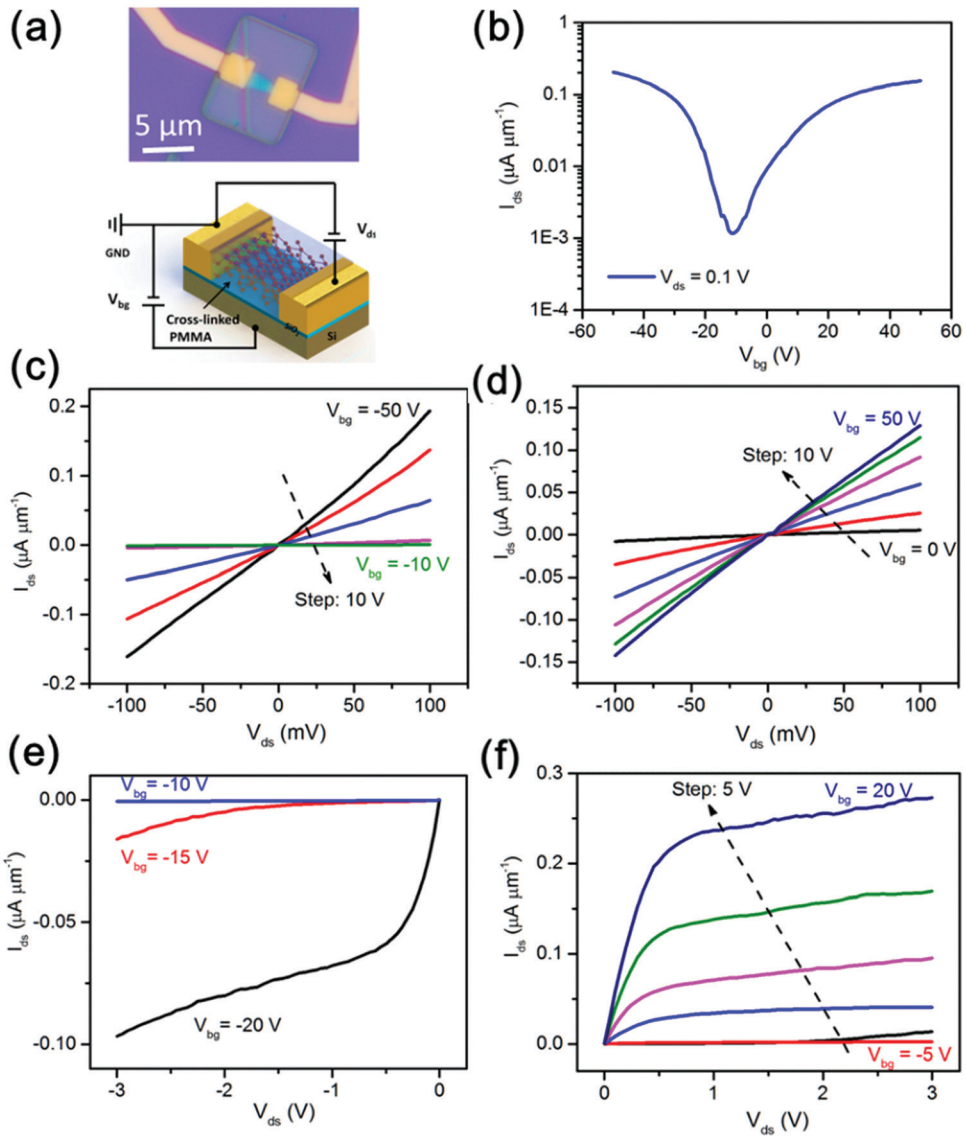

Fig. 17 Transfer and output characteristics of a BP FET capped with cross-linked PMMA with Ni/Au as contact electrodes. (a) Optical image (upper panel) and schematic (lower panel) of the cross-linked PMMA capped BP FET, respectively. (b) Transfer characteristics of the BP FET capped with cross-linked PMMA with a source–drain voltage of 0.1 V, showing symmetric ambipolar transport behavior. (c and d) Output characteristics of the device at small V_{ds}. (e) and (f) Output characteristics of the device at large V_{ds}. Adapted with permission from ref. 325. Copyright 2016, American Chemical Society.

the performances of electronic devices based on 2D semiconductors have been greatly enhanced. The incompatible contact interface properties between 3D metals and 2D channels can be eliminated by either using van der Waals (vdW) contact to decouple the metal–2D semiconductor interaction[316] or using semimetal contact to suppress the metal induced gap states,[317] yielding a low contact resistance and improved carrier mobility. Insulating 2D hexagonal boron nitride (hBN) has an atomically flat and dangling-bond free surface, which has been proved to greatly improve carrier mobility by effectively suppressing carrier scattering from trapped charges and impurities, and is considered to be the ideal dielectric.[318,319] Using all 2D material components, specifically, MoS_2 as the active channel, graphene as the source/drain and top-gate contact electrodes, and hBN as the top-gate dielectric, field-effect transistors with excellent performance have been made,[320] showing their great promise in constructing integrated circuits.[114]

For construction of complementary metal–oxide–semiconductor (CMOS) and beyond CMOS devices, a reliable complementary doping technique for 2D semiconductors is a prerequisite. Unfortunately, due to their atomically thin nature, using conventional doping techniques, such as ion implantation and thermal diffusion, the lattice of 2D semiconductors will be damaged, resulting in degraded device performance.[321,322] In the past few years, a non-destructive surface charge transfer doping technique has been successfully developed by capping 2D semiconductors with organic molecules,[323–325] metals,[326–328] metal oxides,[329–331] and gas molecules,[332,333] and complementary doping profiles have been achieved.[334] Beyond surface charge transfer doping, electrostatically doping 2D semiconductors with split local gates,[335–338] semi-floating gates,[339] and ferroelectric polarization[340,341] has also been developed, enabling them to be used in diodes,[337–339] memories,[339–341] optoelectronic devices,[336,339,340] and logic[339,341] device applications.

Thanks to the continuous optimized dry-transfer method,[319,342] van der Waals (vdW) heterostructures with atomically clean and sharp interfaces can be formed by layer-by-layer stacking of 2D materials with different band profiles.[157,158] Benefitting from the wide range of band gaps in 2D semiconductors from 0.4 to 2.0 eV, type I (straddling gap), type II (staggered gap), and type III (broken gap) band alignments can all be realized in vdW heterostructures.[159] The sharp and steep band edge profiles in van der Waals heterostuctures give rise to revolutionary possibilities of quantum engineering the transport of charge carriers and excitons.[161] Moreover, vdW heterostructures can be formed by either vertically or laterally stacking 2D semiconductors, enabling the construction of novel proof-of-principle devices.[162–168] Due to their atomically clean and sharp interface properties, these electronic and optoelectronic devices showed extraordinary performance and unique functionality.[169]

5.1 Construction of black phosphorus (BP) planar devices by interface charge transfer doping. As a typical 2D layered semiconductor, black phosphorus (BP) has a moderate bandgap ranging from 0.3 eV for the bulk to 2.0 eV for the monolayer, and a high hole mobility of $\sim$1000 $cm^2 V^{-1} s^{-1}$.[302,343,344] Due to the Schottky barrier formed between metal contacts and the BP channel, asymmetric transport for electrons and holes was observed in BP FETs.[302,345–347] By capping BP with metals,[326,327,348,349] oxides,[330] and organic molecules,[325,350] complementary doping of BP has been realized through a

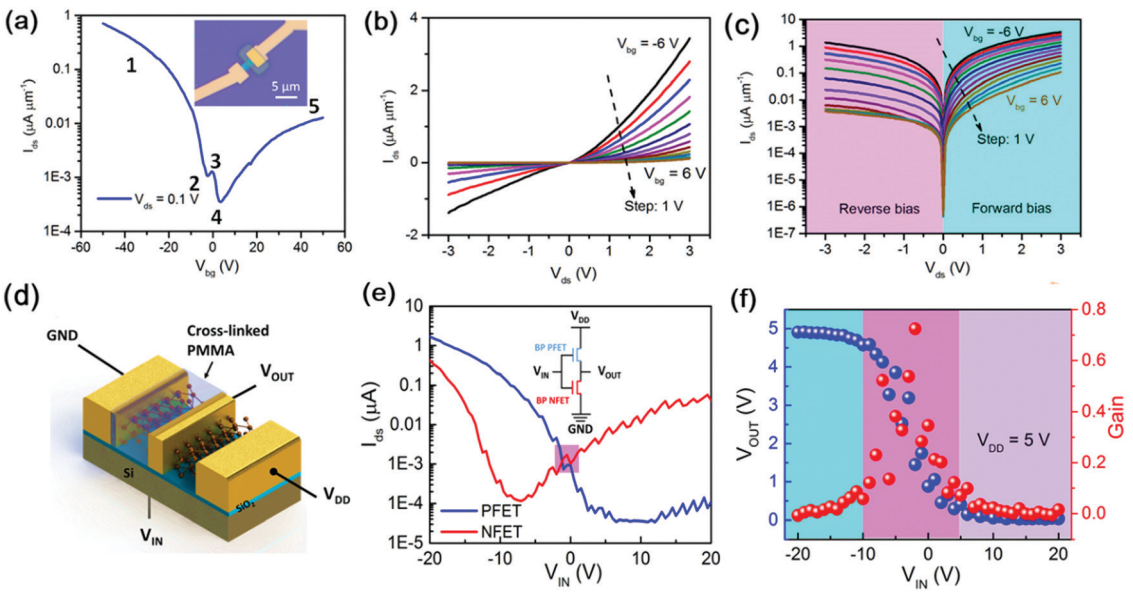

Fig. 18 Electrical characteristics of BP gated diodes and logic inverters. (a) The transfer curve of BP diode current at V_{ds} = 0.1 V. The featured points labeled "1" and "5" represent the p–p and n–n junctions, respectively, "2" and "4" indicate flat-band conditions for the BP PFET and NFET, respectively, and "3" indicates the formation of a potential barrier between the N(capped) and P(uncapped) conduction regions. The inset shows an optical image of the BP diode. (b) *I*–*V* curves of the BP diode under different gate voltages ranging from −6 to 6 V with a step of 1 V. (c) Logarithmic plot of the *I*–*V* curves in (b). (d) Schematic diagram of the logic inverter. (e) Transfer curves of the BP PFET and NFET, respectively. The inset shows the schematic of an equivalent circuit. (f) Output characteristics of the BP logic inverter. Adapted with permission from ref. 325. Copyright 2016, American Chemical Society.

surface charge transfer doping process,[334] enabling the construction of BP complementary devices.[325,348]

When partially capping the BP channel with cross-linked poly(methyl methacrylate) (PMMA), the transfer characteristics of BP FETs with capping show a negative shift of threshold voltage compared to those without capping, indicating an effective electron doping to the BP channel.[325] Fig. 17(a) shows the optical image and device configuration of a cross-linked PMMA capped BP FET. A symmetric ambipolar transport nature was observed in the transfer characteristics (Fig. 17(b)) and the ON/OFF ratio for both electrons and holes can reach $\sim 10^2$–10^3. The good ohmic contact behavior was characterized by the linear relationship in output characteristics for both holes (Fig. 17(c), $V_{bg} < 0$ V) and electrons (Fig. 17(d), $V_{bg} > 0$ V). Under large V_{ds}, an apparent current saturation behavior was observed for both electron and hole conduction, as shown in Fig. 17(e and f), respectively.

The successful complementary doping allows for the construction of a BP diode by partially capping the channel with cross-linked PMMA. Fig. 18(a) shows the transfer characteristics of the BP diode, in which the BP diode undergoes a transition from the p–p junction ($V_{bg} = -50$ V, labelled "1") to an n–n junction ($V_{bg} = 50$ V, labelled "5"). The two valleys located at $V_{bg} = -2$ V (labelled "2") and $V_{bg} = 3.5$ V (labelled "4") can be assigned to the flat band condition of the BP N-FET (capped region) and BP P-FET (region without capping), respectively. The peak at $V_{bg} = -0.4$ V (labelled "3") indicates the formation of potential barriers between the N (capped) and P (uncapped) regions. The output characteristics of the BP diode on both linear (Fig. 18(b)) and logarithmic scales (Fig. 18(c)) clearly reveal gate-tunable current rectification behavior with the rectification ratio ranging from ~ 2 to ~ 70, much smaller than other BP diodes,[327,335,348] which is probably due to the heavily doping to the contact of the electron conduction side. However, for both electron (reverse bias, magenta shaded region) and hole conduction (forward bias, cyan shaded region) sides, the BP diode shows a current on/off ratio of $>10^3$, suggesting that such a BP diode can work as a bipolar switch. When capping the central part of the BP channel in the FET with cross-linked PMMA, two BP diodes back-to-back in series are formed. The output characteristics of this device show a pronounced current rectification behavior with a gate tunable rectification ratio of 10^3–10^4. Moreover, due to the symmetric configuration of the device, the current rectification is not dependent on the polarity of voltage bias; namely, it works as a bidirectional rectifier. The introduction of interfacial charges into the BP channel by cross-linked PMMA can be considered as an effective "top gate", which tunes the Fermi level of the capped region. Combined with the global back gate together, different transport regimes can be reached and a polarity controllable BP FET was constructed.[351] The successful access to the electron and hole doping of BP channels enables the construction of a complementary logic inverter, as schematically shown in Fig. 18(d). Fig. 18(e) shows the transfer characteristics of the BP PFET (blue) and NFET (red), respectively, indicating that by tuning the carrier density in the BP channel, inverted V_{OUT} can be generated in the transition region (highlighted with a pink square). The output characteristics of the BP logic inverter are shown in Fig. 18(f). When V_{IN} is in the range of -20 to -10 V (cyan region), V_{OUT} shows a "high" state to drop with a flat slope. The voltage gain, defined as $G = dV_{OUT}/dV_{IN}$, is gently increased. For V_{IN} in the range of -10 to 5 V (pink region), V_{OUT} shows a "high" state to "low" state

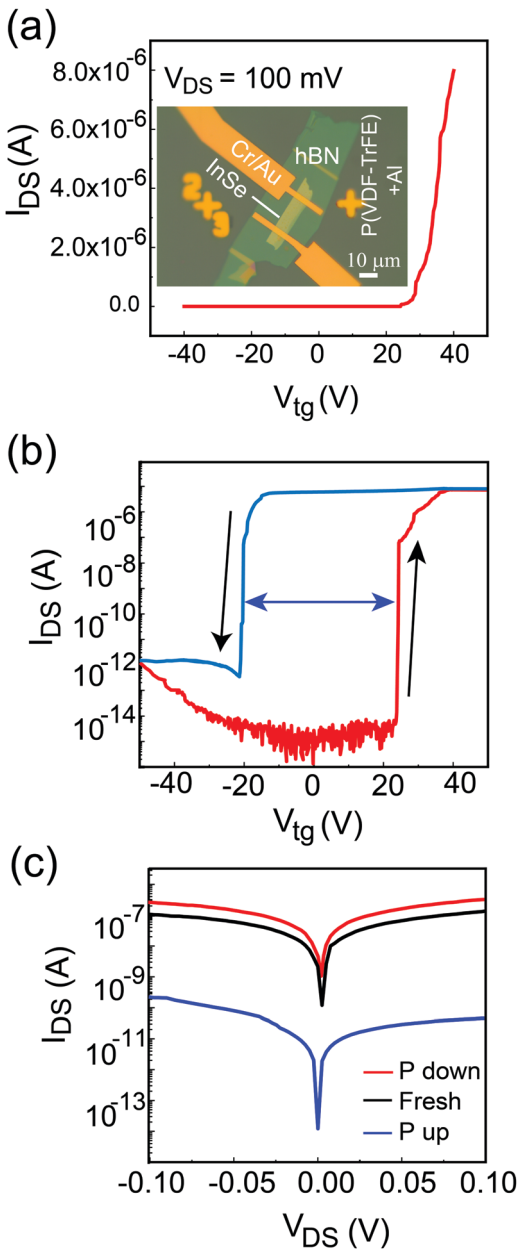

Fig. 19 Transfer and output characteristics of the ferroelectric P(VDF-TrFE) gated InSe FET measured in a dark environment. (a) Linear-scale transfer curve of the ferroelectric P(VDF-TrFE) gated InSe FET. The inset shows the optical image of a typical device. (b) Logarithmic-scale dual-sweeping transfer curves of the ferroelectric P(VDF-TrFE) gated InSe FET. A large memory window of ~ 40 V is clearly presented. (c) The output curves of the InSe FET in three polarization states of the ferroelectric P(VDF-TrFE) layer with $V_{tg} = 0$ V. Adapted with permission from ref. 365. Copyright 2020, American Chemical Society.

($V_{OUT} \approx 0$ V) transition, indicating the inversion of input voltages. The voltage gain shows a peak value of ~0.75. Further increasing V_{IN} results in the steady state of V_{OUT} at around 0 V. Compared with other BP inverters,[352–354] the voltage gain is rather low. One limiting factor of the voltage gain comes from the ambipolar transport of the BP NFET. For a steep switch of V_{OUT}, a real BP NFET is required. Other limiting factors include the contact resistance and the matching of output and input voltages in the transfer characteristics.

5.2 Construction of InSe photodetectors with high on/off ratios and photoresponsivity by ferroelectric gating

Photodetectors are key elementary components for optoelectronic device applications.[355] Photodetectors based on 2D semiconductors, such as transition metal dichalcogenides (TMDCs) and black phosphorus (BP), due to their thickness-dependent sizable bandgaps, show greatly enhanced performance compared to those of graphene with zero bandgap.[356,357] The bottleneck of photodetectors based on 2D semiconductors lies in how to suppress the large dark current to further improve the small photoswitch ratio and photoresponsivity. Compared to conventional dielectrics, such as Al_2O_3, SiO_2 and HfO_2, ferroelectric dielectrics, such as transparent organics P(VDF-TrFE), have much higher dielectric constants, allowing for the effective suppression of dark current and 3–4 orders of magnitude enhancement of photoresponsivity.[340,358,359]

Indium selenide (InSe), as a typical 2D metal monochalcogenide, shows broadband photoresponse with the wavelength ranging from ultraviolet to near-infrared due to its thickness-dependent direct bandgap.[360,361] Photodetectors based on few-layered InSe gated with conventional dielectrics show an on/off ratio of 4.7×10^4, a responsivity of 157 A W^{-1}, and a detectivity of 1.07×10^{11} Jones.[362–364] After replacing the conventional dielectric with a ferroelectric P(VDF-TrFE), the ferroelectric-gated InSe photodetectors show an on/off ratio of over 10^8, a photoresponsivity of ~14 250 A W^{-1}, and a detectivity of ~1.63×10^{13} Jones.[365] Fig. 19(a) shows the linear-scale transfer curve of the ferroelectric P(VDF-TrFE) gated InSe transistor at V_{ds} = 100 mV measured in a dark environment, showing the monotonically increasing channel current with increasing top-gate voltage (V_{tg}), indicating the electron conduction nature in the InSe channel. A large anti-clockwise memory window of ~40 V that resulted from the gradual switching of ferroelectric polarization[358] was observed in the transfer curve of the device in Fig. 19(b). Due to the improved interface properties between InSe and hBN, the on/off ratio reaches ~10^8, which is three orders of magnitude higher than that of the ferroelectric P(VDF-TrFE) gated InSe transistor on a SiO_2/Si substrate.[366] Fig. 19(c) shows the output curves of the InSe FET under different polarization states of the ferroelectric P(VDF-TrFE). Although the current for the P up state is smallest, the off (dark) current can be reduced to ~10^{-14} A, which is critical for improving the photoresponse properties of photodetectors.

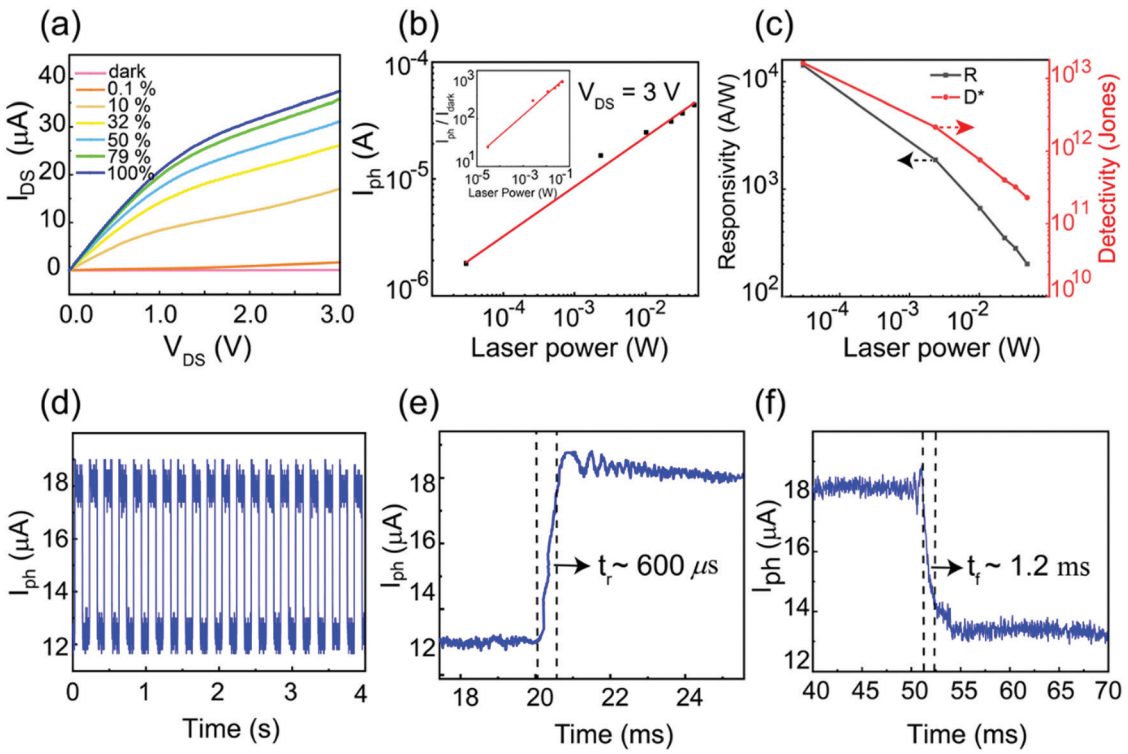

Fig. 20 Photoresponse properties of the ferroelectric P(VDF-TrFE) gated InSe photodetector in the P up state. (a) Output curves of the photodetector under laser illumination with different power levels. (b) Double-logarithmic plot of photocurrent as a function of illumination power. The inset shows the ratio of the photocurrent to dark current under different illumination powers. (c) Photoresponsivity and detectivity of the InSe photodetector as a function of illumination power. (d and f) Periodical switching of the photocurrent under 532 nm laser illumination, revealing that the rise (t_r) and fall (t_f) times are ~600 μs and 1.2 ms, respectively. Adapted with permission from ref. 365. Copyright 2020, American Chemical Society.

The optoelectronic response characteristics of the ferroelectric P(VDF-TrFE) gated InSe transistor in the P up state at V_{ds} = 3 V are shown in Fig. 20(a). The photocurrent I_{ph} shows a power law dependence on laser power (P) of $I \sim P^{0.44}$ (Fig. 20(b)), indicating that the photogenerated carriers are recombined with the trap states coming from the defects, charge impurities, and adsorbates in the InSe channel.[358,359,362] The photoresponsivity and detectivity of the ferroelectric P(VDF-TrFE) gated InSe transistor at a laser power level of 0.04 mW cm^{-2} can reach 14 250 A W^{-1} and 1.63 $\times 10^{13}$ Jones, respectively, which are two orders of magnitude higher than those of SiO_2 back gated InSe transistors,[362] as shown in Fig. 20(c). The fast decay of both photoresponsivity and detectivity may result from the recombination process occurred at the interface between the InSe channel and top-gate P(VDF-TrFE) film. By periodically switching the photocurrent under 532 nm laser illumination, the rise (t_r) and fall (t_f) times can be measured as ~600 μs and ~1.2 ms, respectively, which are higher than those of previously reported ferroelectric-gated 2D photodetectors,[358,359,367] as depicted in Fig. 20(d–f).

5.3 Construction of high-performance electronic devices based on InSe/hBN/graphite heterostructures

In the past decades, 2D materials with sizable bandgaps, such as TMDCs,[146] BP,[302] and group IIIA chalcogenides,[361] have been employed as channel materials to overcome the scaling limits in Si devices.[113] InSe, as a typical member of group IIIA chalcogenides, has high electron mobility and a tunable bandgap, making it a promising channel material for 2D electronic[309,328,368–370] and optoelectronic devices.[360,371–374] hBN has an atomically flat surface with large surface optical phonon energies, and when serving as a gate dielectric for a 2D-material channel, the carrier scattering at the interface between the 2D-material and gate dielectric can be greatly suppressed compared to those of conventional dielectrics.[319,375] High-performance field-effect transistors have been fabricated based on InSe/hBN/graphite heterostructures with electron mobilities up to 1146 cm^2 V^{-1} s^{-1} and on/off ratios up to 10^{10} due to the atomically sharp interface between hBN and the InSe channel.[366]

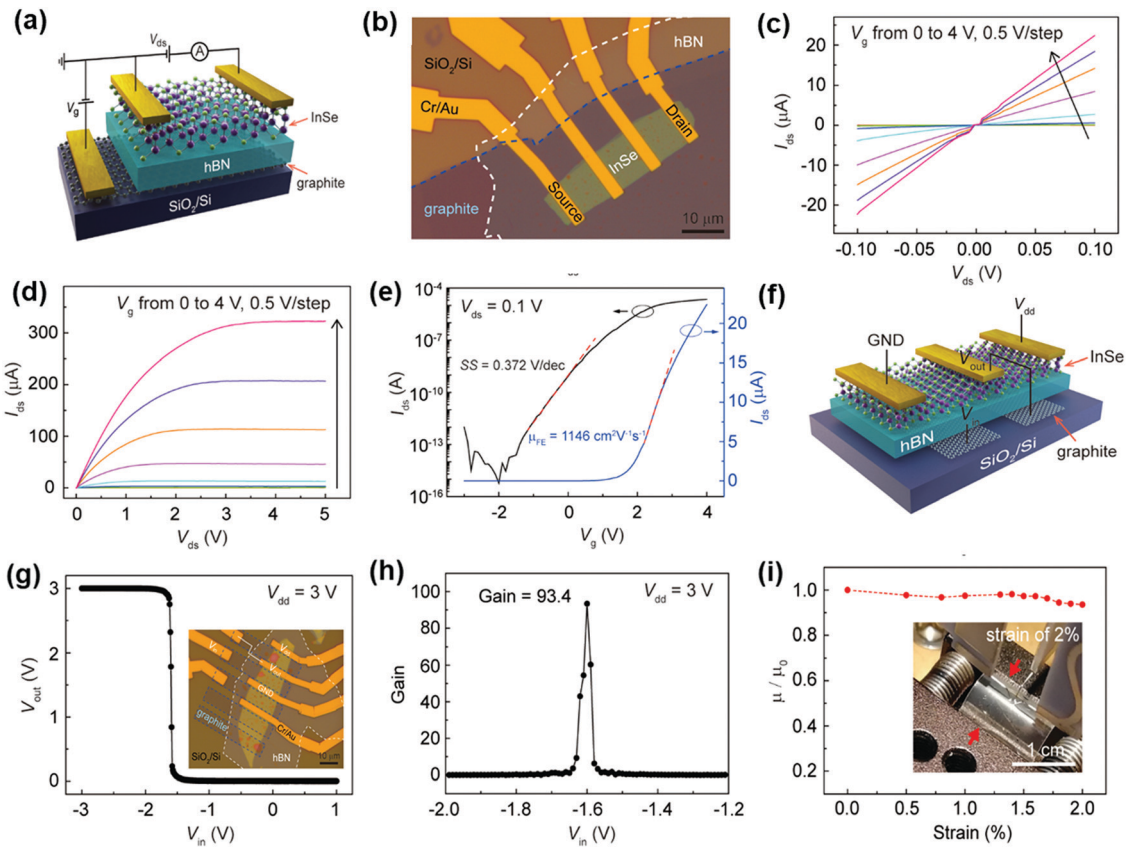

Fig. 21 High-performance electronic devices based on an InSe/hBN/graphite van der Waals heterostructure. (a) Schematic and (b) optical image of the FET based on the InSe/hBN/graphite van der Waals heterostructure. (c and d) Output curves of the heterostructure FET under different gate voltages from 0 to 4 V with a step of 0.5 V at small (c) and large (d) V_{ds}. (e) Linear (blue) and logarithmic (black) scale transfer curves of the heterostructure FET at V_{ds} = 0.1 V. Linear fitting of the curves yields an electron mobility of 1146 cm^2 V^{-1} s^{-1} and a subthreshold swing slope of 0.372 V dec^{-1}, respectively. (f) Schematic of the logic inverter based on the InSe/hBN/graphite van der Waals heterostructure. (g) Output characteristics of the heterostructure inverter at V_{dd} = 3 V. The inset shows an optical image of the inverter. (h) Voltage gain of the heterostructure inverter under different input voltages (V_{IN}) at V_{dd} = 3 V. (i) Ratio of electron mobility in the heterostructure FET placed on a flexible substrate under different strains. Adapted with permission from ref. 366. Copyright 2020, Springer Nature.

Fig. 21(a and b) show the schematic and optical image of an InSe/hBN/graphite heterostructure FET, respectively. The output characteristics of the device at small (Fig. 21(c)) and large (Fig. 21(d)) source–drain bias reveal the good ohmic contact nature and current saturation behaviors, respectively. The transfer curves of the device shown in Fig. 21(e) indicate the electron conduction nature of InSe with an on/off ratio of $\sim 10^{10}$ and an electron mobility of ~ 1146 cm^2 V^{-1} s^{-1}. Due to the greatly reduced density of interfacial trapped charges in the InSe/hBN/graphite heterostructure, the subthreshold swing slope of the device was reduced to ~ 0.372 V dec^{-1} from 6.09 V dec^{-1} of the InSe FET on a SiO_2 (300 nm)/Si substrate. Based on the high performance of the heterostructure FET, a prototype 2D logic inverter was constructed by integrating two InSe heterostructure FETs together using split gates. Fig. 21(f) schematically shows the device configuration. The output characteristics of the logic inverter shown in Fig. 21(g) reveal that when $V_{IN} > -1.6$ V, V_{OUT} is close to 0 V and the logic state of the inverter can be labelled "0", while when $V_{IN} < -2$ V, V_{OUT} is around 3V (V_{dd}) and the logic state can be labelled "1". At a supply voltage of 3 V, the peak voltage gain reaches ~ 93.4 (Fig. 21(h)), which is larger than those of previously reported 2D inverters.[376–383] Benefiting from the superior flexibility of InSe,[384,385] hBN, and graphite, a flexible FET based on the InSe/hBN/graphite heterostructure was fabricated. Fig. 21(i) shows that for a strain level of 2%, there is only a 6.5% drop in electron mobility. The above results suggest that an InSe/hBN/graphite heterostructure device is a promising device configuration for future 2D electronics and flexible electronics as long as high-quality wafer-scaled channel materials and hBN gate dielectrics are available.

5.4 Construction of ultrahigh-speed nonvolatile memory devices

As a mainstream non-volatile memory, a flash memory device suffers from the low-switching speed (~ 75 μs) due to the large tunnel barrier (~ 3–4 eV) and the unavoidable interface dangling bond for the Si/SiO_2 interface.[111] van der Waals heterostructures formed by layer-by-layer stacking 2D materials have atomically sharp and clean interfaces, and by construction of a small tunneling barrier, ultrafast operation of the flash memory device could be achieved. Most recently, ultrafast (~ 20 ns) program/erase operation of floating-gated transistors has been successfully realized based on InSe/hBN/graphite[386] and MoS_2/hBN/graphite heterostructures.[386,387]

Fig. 22(a and b) show the schematic and optical image of a nonvolatile floating-gate device based on the InSe/hBN/graphite heterostructure stacked on a SiO_2/Si substrate, respectively, where InSe, hBN, graphite, SiO2, and Si serve as the channel, tunnel layer, floating gate, control-gate dielectric, and control-gate electrode, respectively. The interface properties between layers were characterized by HAADF-STEM, where atomically flat, sharp, and clean interface properties between functional layers were revealed, as shown in Fig. 22(c–e). A large memory window, defined as the shift of the threshold voltage, proportional to the control gate voltage (V_{cg}) was observed in

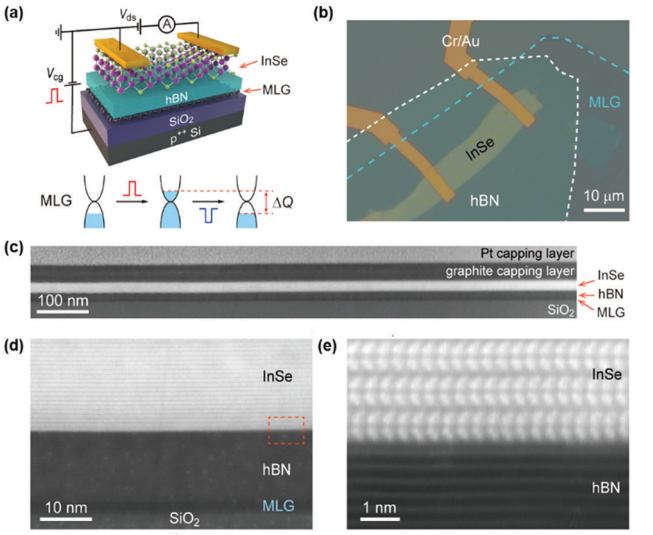

Fig. 22 Nonvolatile memory device based on a van der Waals heterostructure with a floating-gate configuration. (a and b) Schematic and optical image of a floating-gate memory device based on the InSe/hBN/MLG heterostructure stacked on a SiO_2/Si substrate, respectively. (c) Cross-sectional HAADF-STEM image of the InSe/hBN/MLG heterostructure on SiO_2 with graphite and Pt capping layers, indicating uniform in-plane interfaces. (d and e) Higher-resolution HAADF-STEM images of the same heterostructure on different length scales, revealing its atomically sharp and clean interface characteristics. Adapted with permission form ref. 386. Copyright 2021, Springer Nature.

the dually sweeping transfer curve of the floating gate FET. A large charge density of 4.6×10^{12} cm^{-2} can be stored in the graphite floating gate when sweeping V_{cg} from -40 to $+40$ V, which is larger than those of conventional flash memory cells.[388] This was attributed to the higher work function of graphite (~ 4.6 eV) independent of thickness[389,390] and the significant reduction of interference in the floating-gate.[391]

Fig. 23(a) schematically shows the energy band diagrams of the floating-gate memory device for program, read, and erase operations. The electrons can be dragged/filled to/in the InSe channel by tunneling through the hBN barrier when a positive/negative V_{cg} is applied, defined as program/erase operations. An ultrahigh erase/program ratio of $\sim 10^{10}$ was achieved by applying a +17.7/−17.7 V voltage pulse with a full width at half-maximum (FWHM) of 160 ns, as shown in Fig. 23(b), which is much larger than those of previously reported floating-gate memory devices based on 2D materials.[389,390,392,393] The retention characteristics of the floating-gate memory devices characterized by the evolution of the threshold voltage with time after the program/erase operations are shown in Fig. 23(c), where only 14.6% and 27.1% drops in the threshold voltages of the program/erase states were found after extrapolation to 10 years, indicating a robust retention performance of the heterostructure floating gate memory. Fig. 23(d) shows the endurance performance of the floating gate memory device under repeat program and erase operations, clearly showing that no apparent change occurs for both the program and erase states after 2000 cycles. Such robust retention and endurance performance

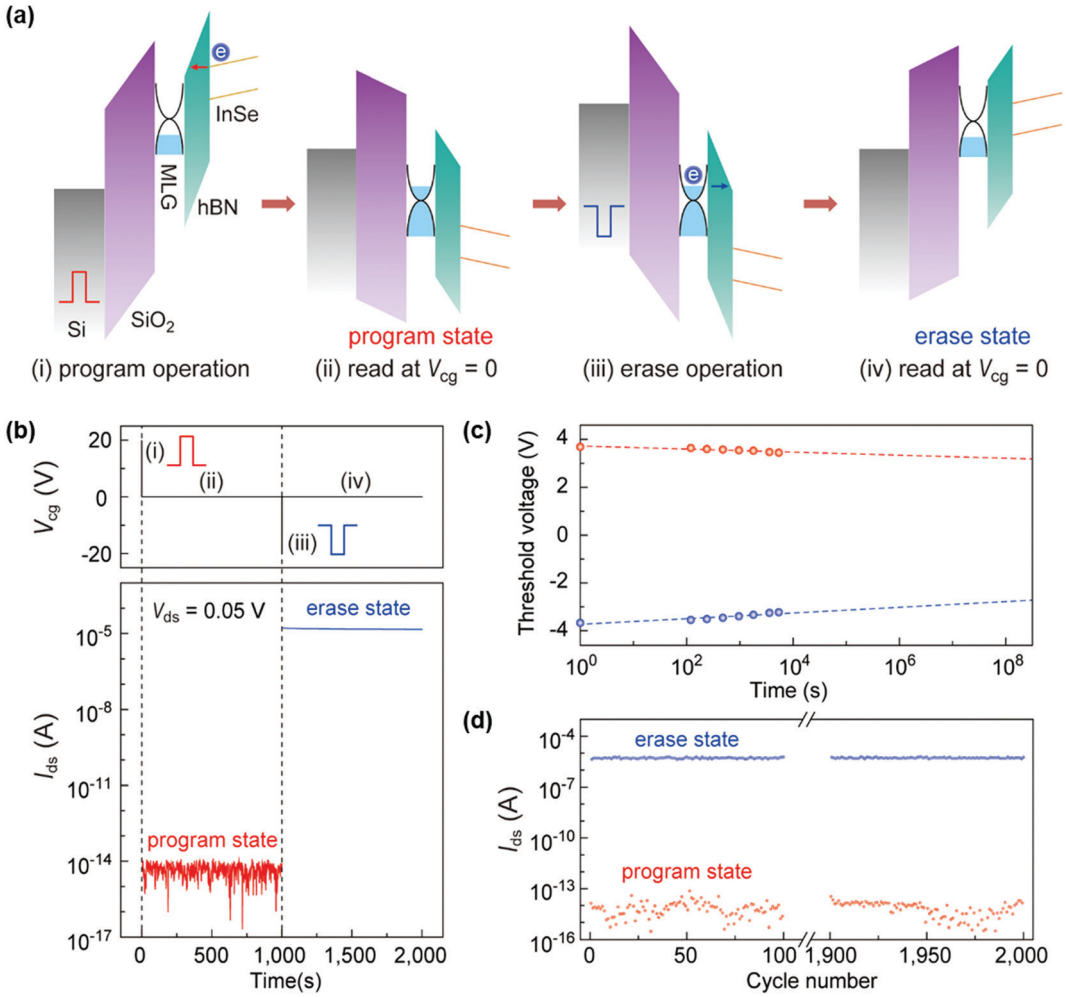

Fig. 23 Program and erase operations of nonvolatile InSe floating-gate memory devices. (a) Schematic of the energy-band diagrams of the floating-gate memory device for program, read and erase operations. (b) The current of the InSe channel after program (low-current state, red) and erase (high-current state, black) operations by applying a single +17.7 V or −17.7 V voltage pulse with 160 ns FWHM, respectively. (c) Evolution of the threshold voltage with time after program/erase operations. (d) Endurance of the channel current in the floating-gate memory device after alternative program/erase operations. Adapted with permission form ref. 386. Copyright 2021, Springer Nature.

was attributed to the adoption of defect-free hBN as a tunneling barrier.[394,395]

The time to program/erase the floating gate memory device has been further reduced to ~21 ns, maintaining the ultrahigh extinction ratio of 10^{10} by applying a +20.2/−20.8 V voltage pulse to V_{cg}, which is almost ~5000 times faster than those of commercial flash memories and comparable to those of volatile dynamic random access memories,[396] as shown in Fig. 24(a). Most importantly, the response time of the ultrafast operation also reached the nanosecond range, which was defined as the time needed to reach $1/e$ of the peak pulse voltage for the program/erase states and estimated as 36 ns and 43 ns for the program and erase operations, respectively, as shown in Fig. 24(b and c). This ultrafast transient response enabled the ultra-frequency operation of the device by sequential program/erase operations up to 5 MHz, as presented in Fig. 24(d). The physical mechanism for the ultrafast operation was attributed to the Fowler–Nordheim tunneling process, in which the tunneling probability/current is greatly enhanced due to the successful reduction of the barrier height in the InSe/hBN van der Waals heterostructure. Choosing a different channel material with a similar work function to that of InSe (~4.7 eV), such as MoS_2 (~4.6 eV), ultrafast program/erase operations with an ultrahigh extinction ratio of ~10^{10} have also successfully achieved.[386,387] The ultrahigh erase/program ratio of 10^{10} allows for multi-bit memory storage. As depicted in Fig. 23(e), distinguishable programmed states labelled (10), (01), and (00) with large enough erase/program ratios can be achieved and all programmed states can be erased back to the (11) state, demonstrating the capability of robust two-bit storage. Although the device was fabricated by a layer-by-layer van der Waals stacking process based on the mechanical exfoliation method, the adoption of a commercial floating gate memory device configuration is compatible with existing industry standards. For future device scale up, the development of wafer-scale synthesis of van der Waals

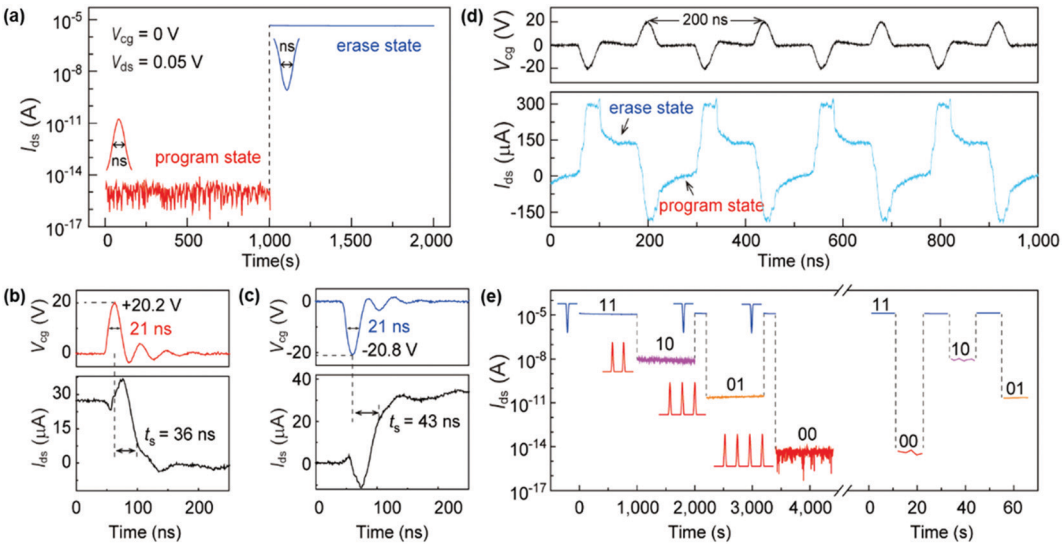

Fig. 24 Ultrafast operation and multi-bit storage of the floating-gate memory. (a) Program and erase of the InSe floating-gate memory device with a 10 nm thick hBN tunnel layer with a positive/negative voltage (+20.2 V/−20.8 V) pulse with a pulse width of ∼20 ns, showing that a high extinction ratio of 10^{10} can be maintained. (b) and (c) Ultrafast response of the InSe floating-gate memory device after applying program (b) and erase (c) pulses. (d) Ultrahigh frequency program and erase operations of the floating-gate memory device with ∼100 ns intervals. (e) Multi-bit storage realized by applying different numbers of ultrafast pulses to program the device with a thicker hBN tunneling layer (∼12 nm) to different current levels. Adapted with permission form ref. 386. Copyright 2021, Springer Nature.

heterostructures with atomic-scale precision and high material quality is required.[397]

6. Summary and outlook

We have reviewed the recent progress in construction of nanoscale electronic devices based on low-dimensional structures and their charge transport properties, including molecules and 2D materials. We started with construction of molecular devices at the single molecule level by precisely controlling the self-assembled structures of molecules on metal surfaces. By tuning the chemical bond between an atom of the molecule and an adatom on the surface, molecular motor arrays with a fixed rotation axis have been achieved. Furthermore, by STM manipulation, the spin state of a single molecule can be reversibly switched, providing a robust and effective way to atomically precisely manipulate the single spin states of a single molecule and will have great implications for information recording and storage at the molecular level. Then we reviewed construction of nanoscale electronic devices based on the high-quality and single-crystal graphene epitaxially grown on a Ru(0001) substrate. By stepwise intercalation of silicon and oxygen followed by post-annealing, thin (∼1 nm) crystalline and thicker (∼2 nm) amorphous SiO_2 layers have been created between graphene and the Ru(0001) substrate, which effectively insulates graphene from the metal substrate, enabling the *in situ* fabrication of graphene Hall devices and the successful observation of SdH oscillations and quantum Hall effects. This method paves the way for directly synthesizing high-quality graphene on insulating substrates and provides a promising platform for graphene electronics. We also discussed the progress of the electrical transport properties of 2D novel magnetic TMDCs, including VX_2, CoX_2, and CrX_2 (X = S, Se, or Te). When their thickness was reduced to the 2D limit, these materials show novel spin-related transport properties, such as a 2D weak antilocalization effect in few-layer VSe_2 due to strong spin–orbit coupling, the Kondo effect induced by intercalated localized moments in multi-layered VTe_2, and linear and non-saturated magnetoresistance in mono- or few-layer CoX_2. Importantly, strong room-temperature ferromagnetism has been discovered in mono- or few-layer $CrTe_2$, providing an ideal platform to investigate intriguing physical properties and offering promising possibilities to construct 2D magnet based spintronic devices. Finally we reviewed construction of nanoscale electronic devices based on 2D semiconductors. An interfacial charge transfer method has been developed for complementary doping of black phosphorus, enabling the fabrication of a family of planar devices. By successful suppression of carrier scattering from the interface between 2D channel materials and dielectric substrates, high performance electronic devices with high mobility and low subthreshold voltages and optoelectronic devices with high on/off ratios, high responsivity, and high detectivity have been demonstrated. Surprisingly, benefitting from the atomically sharp interface between van der Waals heterostructures, an ultrafast-speed nonvolatile memory device with an ultrahigh extinction ratio of $\sim 10^{10}$, a program/erase time of ∼20 ns, and long-term storage capability (>10 years) has been described. These achievements demonstrate the remarkable engineering possibilities of 2D semiconductors and their layer-by-layer assembled van der Waals heterostructures.

From the device point of view, the emerging novel physical properties of low-dimensional structures continuously encouraged

the scientists of multi-disciplinary research fields to devote tremendous efforts towards the precise control, understanding, and construction of nanoelectronic devices. Despite the great success in the fabrication of proof-of-concept devices, many challenges still remain. For single molecule devices, STM has been employed as a powerful tool for precisely imaging, resolving the electronic structure, and manipulating the self-assembled ordered molecular structures at the single-molecule level. However, switching the motion or electronic/spin states of single molecules can only be performed one by one. A more efficient parallel method capable of switching multiple molecules each time is required. Another main challenge lies in the real-time imaging of the molecular configuration during their motion. The mismatch between the STM scanning rate and the timescale of molecular motion makes the tracking of the real-time configuration of molecular motion rather challenging. The development of preamplifiers with broader bandwidths will enable the fast STM scanning of the molecular configuration and capture the molecular motion without delay. Moreover, for practical applications of single-molecule devices, the mass production of molecular motors and switches under ambient conditions is a prerequisite. Investigation of the manipulation of molecular motors and switches on inert substrates and understanding of the underlying mechanism are required. For construction of nanoelectronic devices based on graphene and other 2D materials, the development of the reliable and Si-technology compatible method to synthesize high-quality and large-scale 2D materials is required. In the past decade, big progress has been made in wafer-scale growth of graphene, MoS_2, and WS_2. However, effective doping and low-barrier contact are still big challenges. Furthermore, hBN has been proven to be an interface compatible dielectric for 2D materials, which greatly improves the device performance due to the effective suppression of trapped charge and surface roughness. However, the synthesis of wafer-scale hBN with superior dielectric properties is yet to be developed. As an alternative route, dielectric engineering of high-*k* gate dielectrics by deposition of a seed layer on 2D materials has pushed the thickness of gate dielectrics to an equivalent oxide thickness of 1 nm with a reduced roughness, interface states and leakage current, enabling greatly enhanced performance in field-effect transistors based on graphene, MoS_2 and WSe_2. A unique advantage of 2D materials is that lateral or vertical van der Waals heterostructures can be constructed by layer-by-layer stacking of 2D materials with different band profiles, enabling the fabrication of novel proof-of-concept devices. However, the aligned transfer process is unscalable. Growth of wafer-scale and high-quality lateral or vertical heterostructures must be fulfilled for their future heterointegration with Si technology. By properly addressing these challenges faced in the construction of nanoelectronic devices, both single-molecule devices and nanoelectronic devices based on 2D materials will be indispensable in future nanotechnology.

Conflicts of interest

There are no conflicts to declare.

Acknowledgements

We would like to thank the main members in our group including staff and former students, Profs. Shixuan Du, Chengmin Shen, Dongxia Shi, Xiao Lin, Li Gao, Yeliang Wang, Haitao Yang, Zhihui Qin, Qing Huan, Wei Ji, Yu-Yang Zhang, Zhaihai Cheng, Yi Pan; and Drs Qi Liu, Liwei Liu, Haitao Zhou, Yuan Huang, Geng Li, Kai Yang, Hui Chen, Jianchen Lu, Ruisong Ma, Jiahao Yan, Hongtao Liu, Liangmei Wu, Aiwei Wang for their great effort on these works. We also thank our collaborators in the past studies, Prof. Stephen J. Pennycook, Prof. Sokrates T. Pantelides, Prof. Harald Fuchs, Prof. Karl-Heinz Ernst, Prof. H.-J. Freund, Prof. Werner A. Hofer, Prof. Hong Guo, Prof. Feng Liu, Prof. Min Ouyang, Prof. Antonio H. Castro Neto, Prof. Yongji Gong, Prof. Changzhi Gu, and Prof. Yunqi Liu. We thank the National Key Research & Development Projects of China (Grant No. 2016YFA0202300 & 2018YFA0305800), the National Natural Science Foundation of China (Grant No. 61888102), the Strategic Priority Research Program of the Chinese Academy of Sciences (CAS; Grant No. XDB 30000000 & XDB 28000000), the CAS Project for Young Scientists in Basic Research (YSBR-003), and the Youth Innovation Promotion Association of CAS (Y201902).

References

1 S. De Franceschi and L. Kouwenhoven, *Nature*, 2002, **417**, 701–702.
2 M. Ratner, *Nature*, 2005, **435**, 575–577.
3 W. Lu, P. Xie and C. M. Lieber, *IEEE Trans. Electron Devices*, 2008, **55**, 2859–2876.
4 L. Meng, R. Wu, L. Zhang, L. Li, S. Du, Y. Wang and H. J. Gao, *J. Phys.: Condens. Matter*, 2012, **24**, 314214.
5 L. Gao, J. R. Guest and N. P. Guisinger, *Nano Lett.*, 2010, **10**, 3512–3516.
6 H. Guo, R. Zhang, H. Li, X. Wang, H. Lu, K. Qian, G. Li, L. Huang, X. Lin, Y.-Y. Zhang, H. Ding, S. Du, S. T. Pantelides and H.-J. Gao, *Nano Lett.*, 2020, **20**, 2674–2680.
7 H. J. Gao, Z. Q. Xue, K. Z. Wang, Q. D. Wu and S. Pang, *Appl. Phys. Lett.*, 1996, **68**, 2192–2194.
8 H. J. Gao, K. Sohlberg, Z. Q. Xue, H. Y. Chen, S. M. Hou, L. P. Ma, X. W. Fang, S. J. Pang and S. J. Pennycook, *Phys. Rev. Lett.*, 2000, **84**, 1780–1783.
9 M. Feng, X. Guo, X. Lin, X. He, W. Ji, S. Du, D. Zhang, D. Zhu and H. Gao, *J. Am. Chem. Soc.*, 2005, **127**, 15338–15339.
10 M. Feng, L. Gao, Z. Deng, W. Ji, X. Guo, S. Du, D. Shi, D. Zhang, D. Zhu and H. Gao, *J. Am. Chem. Soc.*, 2007, **129**, 2204–2205.
11 H. J. Gao and L. Gao, *Prog. Surf. Sci.*, 2010, **85**, 28–91.
12 Y. L. Wang, W. Ji, D. X. Shi, S. X. Du, C. Seidel, Y. G. Ma, H. J. Gao, L. F. Chi and H. Fuchs, *Phys. Rev. B: Condens. Matter Mater. Phys.*, 2004, **69**, 075408.
13 S. X. Du, H. J. Gao, C. Seidel, L. Tsetseris, W. Ji, H. Kopf, L. F. Chi, H. Fuchs, S. J. Pennycook and S. T. Pantelides, *Phys. Rev. Lett.*, 2006, **97**, 156105.

14 Z. H. Cheng, L. Gao, Z. T. Deng, N. Jiang, Q. Liu, D. X. Shi, S. X. Du, H. M. Guo and H. J. Gao, *J. Phys. Chem. C*, 2007, **111**, 9240–9244.
15 S. A. Burke, W. Ji, J. M. Mativetsky, J. M. Topple, S. Fostner, H. J. Gao, H. Guo and P. Grütter, *Phys. Rev. Lett.*, 2008, **100**, 186104.
16 L. Gao, Q. Liu, Y. Y. Zhang, N. Jiang, H. G. Zhang, Z. H. Cheng, W. F. Qiu, S. X. Du, Y. Q. Liu, W. A. Hofer and H. J. Gao, *Phys. Rev. Lett.*, 2008, **101**, 197209.
17 Z. T. Deng, H. M. Guo, W. Guo, L. Gao, Z. H. Cheng, D. X. Shi and H. J. Gao, *J. Phys. Chem. C*, 2009, **113**, 11223–11227.
18 D. Shi, W. Ji, B. Yang, H. Cun, S. Du, L. Chi, H. Fuchs, W. A. Hofer and H.-J. Gao, *J. Phys. Chem. C*, 2009, **113**, 17643–17647.
19 B. Yang, Y. Wang, G. Li, H. Cun, Y. Ma, S. Du, M. Xu, Y. Song and H. J. Gao, *J. Phys. Chem. C*, 2009, **113**, 17590–17594.
20 N. Jiang, Y. Wang, Q. Liu, Y. Zhang, Z. Deng, K.-H. Ernst and H.-J. Gao, *Phys. Chem. Chem. Phys.*, 2010, **12**, 1318–1322.
21 L. Zhang, D. Shi, S. Du, L. Chi, H. Fuchs and H.-J. Gao, *J. Phys. Chem. C*, 2010, **114**, 11180–11184.
22 Y. H. Jiang, W. D. Xiao, L. W. Liu, L. Z. Zhang, J. C. Lian, K. Yang, S. X. Du and H. J. Gao, *J. Phys. Chem. C*, 2011, **115**, 21750–21754.
23 J. T. Sun, L. Gao, X. B. He, Z. H. Cheng, Z. T. Deng, X. Lin, H. Hu, S. X. Du, F. Liu and H. J. Gao, *Phys. Rev. B: Condens. Matter Mater. Phys.*, 2011, **83**, 115419.
24 H. G. Zhang, J. T. Sun, T. Low, L. Z. Zhang, Y. Pan, Q. Liu, J. H. Mao, H. T. Zhou, H. M. Guo, S. X. Du, F. Guinea and H. J. Gao, *Phys. Rev. B: Condens. Matter Mater. Phys.*, 2011, **84**, 245436.
25 Y. Y. Zhang, S. X. Du and H. J. Gao, *Phys. Rev. B: Condens. Matter Mater. Phys.*, 2011, **84**, 125446.
26 H. Cun, Y. Wang, S. Du, L. Zhang, L. Zhang, B. Yang, X. He, Y. Wang, X. Zhu, Q. Yuan, Y.-P. Zhao, M. Ouyang, W. A. Hofer, S. J. Pennycook and H.-J. Gao, *Nano Letters*, 2012, **12**, 1229–1234.
27 G. Li, H. T. Zhou, L. D. Pan, Y. Zhang, J. H. Mao, Q. Zou, H. M. Guo, Y. L. Wang, S. X. Du and H.-J. Gao, *Appl. Phys. Lett.*, 2012, **100**, 013304.
28 L. W. Liu, K. Yang, W. D. Xiao, Y. H. Jiang, B. Q. Song, S. X. Du and H.-J. Gao, *Appl. Phys. Lett.*, 2013, **103**, 023110.
29 H. Zhou, L. Zhang, J. Mao, G. Li, Y. Zhang, Y. Wang, S. Du, W. A. Hofer and H.-J. Gao, *Nano Res.*, 2013, **6**, 131–137.
30 K. Yang, W. Xiao, L. Liu, X. Fei, H. Chen, S. Du and H.-J. Gao, *Nano Res.*, 2014, **7**, 79–84.
31 H. Zhou, J. Liu, S. Du, L. Zhang, G. Li, Y. Zhang, B. Z. Tang and H.-J. Gao, *J. Am. Chem. Soc.*, 2014, **136**, 5567–5570.
32 R. Wu, L. Yan, Y. Zhang, J. Ren, D. Bao, H. Zhang, Y. Wang, S. Du, Q. Huan and H.-J. Gao, *J. Phys. Chem. C*, 2015, **119**, 8208–8212.
33 Y. Zhang, Y. Zhang, G. Li, J. Lu, X. Lin, Y. Tan, X. Feng, S. Du, K. Müllen and H.-J. Gao, *J. Chem. Phys.*, 2015, **142**, 101911.
34 J. Lu, D.-L. Bao, H. Dong, K. Qian, S. Zhang, J. Liu, Y. Zhang, X. Lin, S.-X. Du, W. Hu and H.-J. Gao, *J. Phys. Chem. Lett.*, 2017, **8**, 326–331.
35 J. Ren, D.-L. Bao, L. Dong, L. Gao, R. Wu, L. Yan, A. Wang, J. Yan, Y. Wang, Q. Huan, J.-T. Sun, S. Du and H.-J. Gao, *J. Phys. Chem. C*, 2017, **121**, 21650–21657.
36 T. Pope, S. Du, H.-J. Gao and W. A. Hofer, *Chem. Commun.*, 2018, **54**, 5508–5517.
37 R. Wu, L. Yan, D.-L. Bao, J. Ren, S. Du, Y. Wang, Q. Huan and H.-J. Gao, *J. Phys. Chem. C*, 2019, **123**, 7202–7208.
38 H. Chen, L. Tao, D. Wang, Z.-Y. Wu, J.-L. Zhang, S. Gao, W. Xiao, S. Du, K.-H. Ernst and H.-J. Gao, *Angew. Chem., Int. Ed.*, 2020, **59**, 17413–17416.
39 J. Qi, Y. Gao, H. Jia, M. Richter, L. Huang, Y. Cao, H. Yang, Q. Zheng, R. Berger, J. Liu, X. Lin, H. Lu, Z. Cheng, M. Ouyang, X. Feng, S. Du and H.-J. Gao, *J. Am. Chem. Soc.*, 2020, **142**, 10673–10680.
40 J. V. Barth, G. Costantini and K. Kern, *Nature*, 2005, **437**, 671–679.
41 L. Gao, S.-X. Du and H.-J. Gao, *Int. J. Mol. Sci.*, 2010, **11**, 656–671.
42 Z. T. Deng, H. Lin, W. Ji, L. Gao, X. Lin, Z. H. Cheng, X. B. He, J. L. Lu, D. X. Shi, W. A. Hofer and H. J. Gao, *Phys. Rev. Lett.*, 2006, **96**, 156102.
43 D. X. Shi, W. Ji, X. Lin, X. B. He, J. C. Lian, L. Gao, J. M. Cai, H. Lin, S. X. Du, F. Lin, C. Seidel, L. F. Chi, W. A. Hofer, H. Fuchs and H. J. Gao, *Phys. Rev. Lett.*, 2006, **96**, 226101.
44 L. Gao, J. T. Sun, Z. H. Cheng, Z. T. Deng, X. Lin, S. X. Du and H. J. Gao, *Surf. Sci.*, 2007, **601**, 3179–3185.
45 W. Ji, Z.-Y. Lu and H.-J. Gao, *Phys. Rev. B: Condens. Matter Mater. Phys.*, 2008, 77, 113406.
46 N. Jiang, Y. Y. Zhang, Q. Liu, Z. H. Cheng, Z. T. Deng, S. X. Du, H. J. Gao, M. J. Beck and S. T. Pantelides, *Nano Lett.*, 2010, **10**, 1184–1188.
47 Q. Liu, Y. Y. Zhang, N. Jiang, H. G. Zhang, L. Gao, S. X. Du and H. J. Gao, *Phys. Rev. Lett.*, 2010, **104**, 166101.
48 Z. H. Cheng, S. X. Du, N. Jiang, Y. Y. Zhang, W. Guo, W. A. Hofer and H. J. Gao, *Surf. Sci.*, 2011, **605**, 415–418.
49 L. Zhang, Z. Cheng, Q. Huan, X. He, X. Lin, L. Gao, Z. Deng, N. Jiang, Q. Liu, S. Du, H. Guo and H.-j. Gao, *J. Phys. Chem. C*, 2011, **115**, 10791–10796.
50 H. T. Zhou, J. H. Mao, G. Li, Y. L. Wang, X. L. Feng, S. X. Du, K. Müllen and H.-J. Gao, *Appl. Phys. Lett.*, 2011, **99**, 153101.
51 K. Yang, W. D. Xiao, Y. H. Jiang, H. G. Zhang, L. W. Liu, J. H. Mao, H. T. Zhou, S. X. Du and H. J. Gao, *J. Phys. Chem. C*, 2012, **116**, 14052–14056.
52 K. Yang, L. Liu, L. Zhang, W. Xiao, X. Fei, H. Chen, S. Du, K.-H. Ernst and H.-J. Gao, *ACS Nano*, 2014, **8**, 2246–2251.
53 Y. Y. Zhang, Y.-L. Wang, L. Meng, S. B. Zhang and H.-J. Gao, *J. Phys. Chem. C*, 2014, **118**, 6278–6282.
54 L. Liu, K. Yang, Y. Jiang, B. Song, W. Xiao, S. Song, S. Du, M. Ouyang, W. A. Hofer, A. H. Castro Neto and H.-J. Gao, *Phys. Rev. Lett.*, 2015, **114**, 126601.
55 H. Chen, T. Pope, Z.-Y. Wu, D. Wang, L. Tao, D.-L. Bao, W. Xiao, J.-L. Zhang, Y.-Y. Zhang, S. Du, S. Gao,

S. T. Pantelides, W. A. Hofer and H.-J. Gao, *Nano Lett.*, 2017, **17**, 4929–4933.
56 H.-L. Lu, Y. Cao, J. Qi, A. Bakker, C. A. Strassert, X. Lin, K.-H. Ernst, S. Du, H. Fuchs and H.-J. Gao, *Nano Lett.*, 2018, **18**, 4704–4709.
57 Q. Liu, S. Du, Y. Zhang, N. Jiang, D. Shi and H.-J. Gao, *Small*, 2012, **8**, 796–806.
58 H. Gao, W. Ji and M. Feng, *J. Comput. Theor. Nanosci.*, 2006, **3**, 970–981.
59 L. Cai, M. Feng, H. Guo, W. Ji, S. Du, L. Chi, H. Fuchs and H.-j. Gao, *J. Phys. Chem. C*, 2008, **112**, 17038–17041.
60 L. Liu, K. Yang, Y. Jiang, B. Song, W. Xiao, L. Li, H. Zhou, Y. Wang, S. Du, M. Ouyang, W. A. Hofer, A. H. Castro Neto and H.-J. Gao, *Sci. Rep.*, 2013, **3**, 1210.
61 K. Yang, H. Chen, T. Pope, Y. Hu, L. Liu, D. Wang, L. Tao, W. Xiao, X. Fei, Y.-Y. Zhang, H.-G. Luo, S. Du, T. Xiang, W. A. Hofer and H.-J. Gao, *Nat. Commun.*, 2019, **10**, 3599.
62 Y. Xing, H. Chen, B. Hu, Y. Ye, W. A. Hofer and H.-J. Gao, *Nano Res.*, 2022, **15**, 1466–1471.
63 M. F. Crommie, *Science*, 2005, **309**, 1501–1502.
64 J. R. Heath, *Annu. Rev. Mater. Res.*, 2009, **39**, 1–23.
65 H. Song, M. A. Reed and T. Lee, *Adv. Mater.*, 2011, **23**, 1583–1608.
66 S. Sanvito, *Chem. Soc. Rev.*, 2011, **40**, 3336–3355.
67 L. Bogani and W. Wernsdorfer, *Nat. Mater.*, 2008, **7**, 179–186.
68 N. Roch, S. Florens, T. A. Costi, W. Wernsdorfer and F. Balestro, *Phys. Rev. Lett.*, 2009, **103**, 197202.
69 S. Pan, A. Zhao, B. Wang, J. Yang and J. Hou, *Adv. Mater.*, 2010, **22**, 1967–1971.
70 W. Y. Kim, Y. C. Choi, S. K. Min, Y. Cho and K. S. Kim, *Chem. Soc. Rev.*, 2009, **38**, 2319–2333.
71 L. Sun, Y. A. Diaz-Fernandez, T. A. Gschneidtner, F. Westerlund, S. Lara-Avila and K. Moth-Poulsen, *Chem. Soc. Rev.*, 2014, **43**, 7378–7411.
72 N. Xin, J. Guan, C. Zhou, X. Chen, C. Gu, Y. Li, M. A. Ratner, A. Nitzan, J. F. Stoddart and X. Guo, *Nat. Rev. Phys.*, 2019, **1**, 211–230.
73 S. Kubatkin, A. Danilov, M. Hjort, J. Cornil, J. L. Bredas, N. Stuhr-Hansen, P. Hedegard and T. Bjornholm, *Nature*, 2003, **425**, 698–701.
74 H. B. Yu, Y. Luo, K. Beverly, J. F. Stoddart, H. R. Tseng and J. R. Heath, *Angew. Chem., Int. Ed.*, 2003, **42**, 5706–5711.
75 L. H. Yu, Z. K. Keane, J. W. Ciszek, L. Cheng, M. P. Stewart, J. M. Tour and D. Natelson, *Phys. Rev. Lett.*, 2004, **93**, 266802.
76 A. V. Danilov, S. E. Kubatkin, S. G. Kafanov, K. Flensberg and T. Bjornholm, *Nano Lett.*, 2006, **6**, 2184–2190.
77 A. Baratz and R. Baer, *J. Phys. Chem. Lett.*, 2012, **3**, 498–502.
78 M. Xue and K. L. Wang, *Sensors*, 2012, **12**, 11612–11637.
79 J. L. Zhang, J. Q. Zhong, J. D. Lin, W. P. Hu, K. Wu, G. Q. Xu, A. T. S. Wee and W. Chen, *Chem. Soc. Rev.*, 2015, **44**, 2998–3022.
80 X. Yin, Y. Zang, L. Zhu, J. Z. Low, Z.-F. Liu, J. Cui, J. B. Neaton, L. Venkataraman and L. M. Campos, *Sci. Adv.*, 2017, **3**, eaao2615.
81 S.-X. Du, Y.-L. Wang, Q. Liu, H.-G. Zhang, H.-M. Guo and H. J. Gao, *Front. Phys. China*, 2010, **5**, 380–386.
82 M. Schliwa and G. Woehlke, *Nature*, 2003, **422**, 759–765.
83 S. P. Fletcher, F. Dumur, M. M. Pollard and B. L. Feringa, *Science*, 2005, **310**, 80–82.
84 G. S. Kottas, L. I. Clarke, D. Horinek and J. Michl, *Chem. Rev.*, 2005, **105**, 1281–1376.
85 W. R. Browne and B. L. Feringa, *Nat. Nanotechnol.*, 2006, **1**, 25–35.
86 E. R. Kay, D. A. Leigh and F. Zerbetto, *Angew. Chem., Int. Ed.*, 2007, **46**, 72–191.
87 Z. Li, C. Y. Gao, D. Su, C. Jia and X. Guo, *ACS Mater. Lett.*, 2021, **3**, 1484–1502.
88 Y. Shirai, A. J. Osgood, Y. M. Zhao, K. F. Kelly and J. M. Tour, *Nano Lett.*, 2005, **5**, 2330–2334.
89 T. Kudernac, N. Ruangsupapichat, M. Parschau, B. Maciá, N. Katsonis, S. R. Harutyunyan, K.-H. Ernst and B. L. Feringa, *Nature*, 2011, **479**, 208–211.
90 G. J. Simpson, V. Garcia-Lopez, P. Petermeier, L. Grill and J. M. Tour, *Nat. Nanotechnol.*, 2017, **12**, 604–606.
91 Y. Tabe and H. Yokoyama, *Nat. Mater.*, 2003, **2**, 806–809.
92 T. Benincori, G. Celentano, T. Pilati, A. Ponti, S. Rizzo and F. Sannicolo, *Angew. Chem., Int. Ed.*, 2006, **45**, 6193–6196.
93 Y. Zhang, J. P. Calupitan, T. Rojas, R. Tumbleson, G. Erbland, C. Kammerer, T. M. Ajayi, S. Wang, L. A. Curtiss, A. T. Ngo, S. E. Ulloa, G. Rapenne and S. W. Hla, *Nat. Commun.*, 2019, **10**, 3742.
94 F. Chiaravalloti, L. Gross, K.-H. Rieder, S. M. Stojkovic, A. Gourdon, C. Joachim and F. Moresco, *Nat. Mater.*, 2007, **6**, 30–33.
95 C. Manzano, W. H. Soe, H. S. Wong, F. Ample, A. Gourdon, N. Chandrasekhar and C. Joachim, *Nat. Mater.*, 2009, **8**, 576–579.
96 M. Baroncini and A. Credi, *Science*, 2017, **356**, 906–907.
97 R. A. van Delden, M. K. J. ter Wiel, M. M. Pollard, J. Vicario, N. Koumura and B. L. Feringa, *Nature*, 2005, **437**, 1337–1340.
98 L. Grill, K. H. Rieder, F. Moresco, G. Rapenne, S. Stojkovic, X. Bouju and C. Joachim, *Nat. Nanotechnol.*, 2007, **2**, 95–98.
99 H. L. Tierney, C. J. Murphy, A. D. Jewell, A. E. Baber, E. V. Iski, H. Y. Khodaverdian, A. F. McGuire, N. Klebanov and E. C. H. Sykes, *Nat. Nanotechnol.*, 2011, **6**, 625–629.
100 U. G. E. Perera, F. Ample, H. Kersell, Y. Zhang, G. Vives, J. Echeverria, M. Grisolia, G. Rapenne, C. Joachim and S. W. Hla, *Nat. Nanotechnol.*, 2013, **8**, 46–51.
101 J. C. M. Kistemaker, P. Stacko, J. Visser and B. L. Feringa, *Nat. Chem.*, 2015, **7**, 890–896.
102 Y. Zhang, H. Kersell, R. Stefak, J. Echeverria, V. Iancu, U. G. E. Perera, Y. Li, A. Deshpande, K. F. Braun, C. Joachim, G. Rapenne and S. W. Hla, *Nat. Nanotechnol.*, 2016, **11**, 706–712.
103 B. S. L. Collins, J. C. M. Kistemaker, E. Otten and B. L. Feringa, *Nat. Chem.*, 2016, **8**, 860–866.
104 J. Ren, M. Freitag, C. Schwermann, A. Bakker, S. Amirjalayer, A. Rühling, H.-Y. Gao, N. L. Doltsinis, F. Glorius and H. Fuchs, *Nano Lett.*, 2020, **20**, 5922–5928.

105 K. S. Novoselov, D. Jiang, F. Schedin, T. J. Booth, V. V. Khotkevich, S. V. Morozov and A. K. Geim, *Proc. Natl. Acad. Sci. U. S. A.*, 2005, **102**, 10451–10453.
106 Y. Pan, L. Zhang, L. Huang, L. Li, L. Meng, M. Gao, Q. Huan, X. Lin, Y. Wang, S. Du, H.-J. Freund and H.-J. Gao, *Small*, 2014, **10**, 2215–2225.
107 G. Li, Y.-Y. Zhang, H. Guo, L. Huang, H. Lu, X. Lin, Y.-L. Wang, S. Du and H.-J. Gao, *Chem. Soc. Rev.*, 2018, **47**, 6073–6100.
108 K. S. Novoselov, A. K. Geim, S. V. Morozov, D. Jiang, Y. Zhang, S. V. Dubonos, I. V. Grigorieva and A. A. Firsov, *Science*, 2004, **306**, 666–669.
109 A. K. Geim and K. S. Novoselov, *Nat. Mater.*, 2007, **6**, 183–191.
110 S. Manzeli, D. Ovchinnikov, D. Pasquier, O. V. Yazyev and A. Kis, *Nat. Rev. Mater.*, 2017, **2**, 17033.
111 M. Chhowalla, D. Jena and H. Zhang, *Nat. Rev. Mater.*, 2016, **1**, 16052.
112 Y. Liu, X. Duan, H.-J. Shin, S. Park, Y. Huang and X. Duan, *Nature*, 2021, **591**, 43–53.
113 G. Fiori, F. Bonaccorso, G. Iannaccone, T. Palacios, D. Neumaier, A. Seabaugh, S. K. Banerjee and L. Colombo, *Nat. Nanotechnol.*, 2014, **9**, 768–779.
114 S. Das, A. Sebastian, E. Pop, C. J. McClellan, A. D. Franklin, T. Grasser, T. Knobloch, Y. Illarionov, A. V. Penumatcha, J. Appenzeller, Z. Chen, W. Zhu, I. Asselberghs, L.-J. Li, U. E. Avci, N. Bhat, T. D. Anthopoulos and R. Singh, *Nat. Electron.*, 2021, **4**, 786–799.
115 X. Li, W. Cai, J. An, S. Kim, J. Nah, D. Yang, R. Piner, A. Velamakanni, I. Jung, E. Tutuc, S. K. Banerjee, L. Colombo and R. S. Ruoff, *Science*, 2009, **324**, 1312–1314.
116 L. Gao, W. Ren, H. Xu, L. Jin, Z. Wang, T. Ma, L.-P. Ma, Z. Zhang, Q. Fu, L.-M. Peng, X. Bao and H.-M. Cheng, *Nat. Commun.*, 2012, **3**, 699.
117 S. Chen, W. Cai, R. D. Piner, J. W. Suk, Y. Wu, Y. Ren, J. Kang and R. S. Ruoff, *Nano Lett.*, 2011, **11**, 3519–3525.
118 D. Geng, B. Wu, Y. Guo, L. Huang, Y. Xue, J. Chen, G. Yu, L. Jiang, W. Hu and Y. Liu, *Proc. Natl. Acad. Sci. U. S. A.*, 2012, **109**, 7992.
119 H. Kim, I. Song, C. Park, M. Son, M. Hong, Y. Kim, J. S. Kim, H.-J. Shin, J. Baik and H. C. Choi, *ACS Nano*, 2013, **7**, 6575–6582.
120 R. Vishwakarma, M. S. Rosmi, K. Takahashi, Y. Wakamatsu, Y. Yaakob, M. I. Araby, G. Kalita, M. Kitazawa and M. Tanemura, *Sci. Rep.*, 2017, **7**, 43756.
121 S. Wei, L.-P. Ma, M.-L. Chen, Z. Liu, W. Ma, D.-M. Sun, H.-M. Cheng and W. Ren, *Carbon*, 2019, **148**, 241–248.
122 J. Chen, Y. Guo, L. Jiang, Z. Xu, L. Huang, Y. Xue, D. Geng, B. Wu, W. Hu, G. Yu and Y. Liu, *Adv. Mater.*, 2014, **26**, 1348–1353.
123 P. Yi, S. Dong-Xia and G. Hong-Jun, *Chinese Physics*, 2007, **16**, 3151–3153.
124 P. W. Sutter, J.-I. Flege and E. A. Sutter, *Nat. Mater.*, 2008, **7**, 406–411.
125 Y. Pan, H. Zhang, D. Shi, J. Sun, S. Du, F. Liu and H.-j. Gao, *Adv. Mater.*, 2009, **21**, 2777–2780.
126 W. Chen, X. Gui, L. Yang, H. Zhu and Z. Tang, *Nanoscale Horiz.*, 2019, **4**, 291–320.
127 Y. Zhang, T. Gao, Y. Gao, S. Xie, Q. Ji, K. Yan, H. Peng and Z. Liu, *ACS Nano*, 2011, **5**, 4014–4022.
128 K. Kim, Z. Lee, B. D. Malone, K. T. Chan, B. Aleman, W. Regan, W. Gannett, M. F. Crommie, M. L. Cohen and A. Zettl, *Phys. Rev. B: Condens. Matter Mater. Phys.*, 2011, **83**, 245433.
129 S. U. Yu, B. Park, Y. Cho, S. Hyun, J. K. Kim and K. S. Kim, *ACS Nano*, 2014, **8**, 8662–8668.
130 B. Vasić, A. Zurutuza and R. Gajić, *Carbon*, 2016, **102**, 304–310.
131 P. Xu, M. Neek-Amal, S. D. Barber, J. K. Schoelz, M. L. Ackerman, P. M. Thibado, A. Sadeghi and F. M. Peeters, *Nat. Commun.*, 2014, **5**, 3720.
132 R. S. Ma, J. J. Ma, J. H. Yan, L. M. Wu, W. Guo, S. Wang, Q. Huan, L. H. Bao, S. T. Pantelides and H. J. Gao, *Nanoscale*, 2020, **12**, 12038–12045.
133 R. Ma, Q. Huan, L. Wu, J. Yan, W. Guo, Y.-Y. Zhang, S. Wang, L. Bao, Y. Liu, S. Du, S. T. Pantelides and H.-J. Gao, *Nano Lett.*, 2017, **17**, 5291–5296.
134 G.-X. Ni, Y. Zheng, S. Bae, H. R. Kim, A. Pachoud, Y. S. Kim, C.-L. Tan, D. Im, J.-H. Ahn, B. H. Hong and B. Özyilmaz, *ACS Nano*, 2012, **6**, 1158–1164.
135 J. Lahiri, Y. Lin, P. Bozkurt, I. I. Oleynik and M. Batzill, *Nat. Nanotechnol.*, 2010, **5**, 326–329.
136 P. Y. Huang, C. S. Ruiz-Vargas, A. M. van der Zande, W. S. Whitney, M. P. Levendorf, J. W. Kevek, S. Garg, J. S. Alden, C. J. Hustedt, Y. Zhu, J. Park, P. L. McEuen and D. A. Muller, *Nature*, 2011, **469**, 389–392.
137 L. Tapasztó, P. Nemes-Incze, G. Dobrik, K. J. Yoo, C. Hwang and L. P. Biró, *Appl. Phys. Lett.*, 2012, **100**, 053114.
138 W. Guo, B. Wu, Y. Li, L. Wang, J. Chen, B. Chen, Z. Zhang, L. Peng, S. Wang and Y. Liu, *ACS Nano*, 2015, **9**, 5792–5798.
139 Q. Yu, L. A. Jauregui, W. Wu, R. Colby, J. Tian, Z. Su, H. Cao, Z. Liu, D. Pandey, D. Wei, T. F. Chung, P. Peng, N. P. Guisinger, E. A. Stach, J. Bao, S.-S. Pei and Y. P. Chen, *Nat. Mater.*, 2011, **10**, 443–449.
140 L. A. Jauregui, H. Cao, W. Wu, Q. Yu and Y. P. Chen, *Solid State Commun.*, 2011, **151**, 1100–1104.
141 A. W. Tsen, L. Brown, M. P. Levendorf, F. Ghahari, P. Y. Huang, R. W. Havener, C. S. Ruiz-Vargas, D. A. Muller, P. Kim and J. Park, *Science*, 2012, **336**, 1143–1146.
142 M. Chhowalla, H. S. Shin, G. Eda, L.-J. Li, K. P. Loh and H. Zhang, *Nat. Chem.*, 2013, **5**, 263–275.
143 K. Premasiri and X. P. A. Gao, *J. Phys.: Condens. Matter*, 2019, **31**, 193001.
144 J. R. Schaibley, H. Yu, G. Clark, P. Rivera, J. S. Ross, K. L. Seyler, W. Yao and X. Xu, *Nat. Rev. Mater.*, 2016, **1**, 16055.
145 X. Xu, W. Yao, D. Xiao and T. F. Heinz, *Nat. Phys.*, 2014, **10**, 343–350.
146 Q. H. Wang, K. Kalantar-Zadeh, A. Kis, J. N. Coleman and M. S. Strano, *Nat. Nanotechnol.*, 2012, **7**, 699–712.

147 D. Xiao, G.-B. Liu, W. Feng, X. Xu and W. Yao, *Phys. Rev. Lett.*, 2012, **108**, 196802.
148 H. Yuan, M. S. Bahramy, K. Morimoto, S. Wu, K. Nomura, B.-J. Yang, H. Shimotani, R. Suzuki, M. Toh, C. Kloc, X. Xu, R. Arita, N. Nagaosa and Y. Iwasa, *Nat. Phys.*, 2013, **9**, 563–569.
149 H. Zeng, J. Dai, W. Yao, D. Xiao and X. Cui, *Nat. Nanotechnol.*, 2012, **7**, 490–493.
150 K. F. Mak, K. He, J. Shan and T. F. Heinz, *Nat. Nanotechnol.*, 2012, **7**, 494–498.
151 B. Huang, G. Clark, E. Navarro-Moratalla, D. R. Klein, R. Cheng, K. L. Seyler, D. Zhong, E. Schmidgall, M. A. McGuire, D. H. Cobden, W. Yao, D. Xiao, P. Jarillo-Herrero and X. Xu, *Nature*, 2017, **546**, 270–273.
152 C. Gong, L. Li, Z. Li, H. Ji, A. Stern, Y. Xia, T. Cao, W. Bao, C. Wang, Y. Wang, Z. Q. Qiu, R. J. Cava, S. G. Louie, J. Xia and X. Zhang, *Nature*, 2017, **546**, 265–269.
153 M. Bonilla, S. Kolekar, Y. Ma, H. C. Diaz, V. Kalappattil, R. Das, T. Eggers, H. R. Gutierrez, M.-H. Phan and M. Batzill, *Nat. Nanotechnol.*, 2018, **13**, 289–293.
154 D. R. Klein, D. MacNeill, J. L. Lado, D. Soriano, E. Navarro-Moratalla, K. Watanabe, T. Taniguchi, S. Manni, P. Canfield, J. Fernández-Rossier and P. Jarillo-Herrero, *Science*, 2018, **360**, 1218–1222.
155 C. Gong and X. Zhang, *Science*, 2019, **363**, eaav4450.
156 K. S. Burch, D. Mandrus and J.-G. Park, *Nature*, 2018, **563**, 47–52.
157 K. S. Novoselov and A. H. Castro Neto, *Phys. Scr.*, 2012, **T146**, 014006.
158 A. K. Geim and I. V. Grigorieva, *Nature*, 2013, **499**, 419–425.
159 S. Fan, R. Cao, L. Wang, S. Gao, Y. Zhang, X. Yu and H. Zhang, *Sci. China Mater.*, 2021, **64**, 2359–2387.
160 S. Wu, Q. Zhang, H. Yang, Y. Ma, T. Zhang, L. Liu, H.-J. Gao and Y. Wang, *Prog. Surf. Sci.*, 2021, **96**, 100637.
161 G. Iannaccone, F. Bonaccorso, L. Colombo and G. Fiori, *Nat. Nanotechnol.*, 2018, **13**, 183–191.
162 T. Georgiou, R. Jalil, B. D. Belle, L. Britnell, R. V. Gorbachev, S. V. Morozov, Y.-J. Kim, A. Gholinia, S. J. Haigh, O. Makarovsky, L. Eaves, L. A. Ponomarenko, A. K. Geim, K. S. Novoselov and A. Mishchenko, *Nat. Nanotechnol.*, 2013, **8**, 100–103.
163 W. J. Yu, Z. Li, H. Zhou, Y. Chen, Y. Wang, Y. Huang and X. Duan, *Nat. Mater.*, 2013, **12**, 246–252.
164 W. J. Yu, Y. Liu, H. Zhou, A. Yin, Z. Li, Y. Huang and X. Duan, *Nat. Nanotechnol.*, 2013, **8**, 952–958.
165 Y. Deng, Z. Luo, N. J. Conrad, H. Liu, Y. Gong, S. Najmaei, P. M. Ajayan, J. Lou, X. Xu and P. D. Ye, *ACS Nano*, 2014, **8**, 8292–8299.
166 F. Withers, O. Del Pozo-Zamudio, A. Mishchenko, A. P. Rooney, A. Gholinia, K. Watanabe, T. Taniguchi, S. J. Haigh, A. K. Geim, A. I. Tartakovskii and K. S. Novoselov, *Nat. Mater.*, 2015, **14**, 301–306.
167 M. Huang, S. Li, Z. Zhang, X. Xiong, X. Li and Y. Wu, *Nat. Nanotechnol.*, 2017, **12**, 1148–1154.
168 X. Xiong, M. Huang, B. Hu, X. Li, F. Liu, S. Li, M. Tian, T. Li, J. Song and Y. Wu, *Nat. Electron.*, 2020, **3**, 106–112.
169 Y. Liu, N. O. Weiss, X. Duan, H.-C. Cheng, Y. Huang and X. Duan, *Nat. Rev. Mater.*, 2016, **1**, 16042.
170 D. Xiang, X. Wang, C. Jia, T. Lee and X. Guo, *Chem. Rev.*, 2016, **116**, 4318–4440.
171 X. B. He, J. M. Cai, D. X. Shi, Y. Wang and H. J. Gao, *J. Phys. Chem. C*, 2008, **112**, 7138–7144.
172 R. Wu, D.-L. Bao, L. Yan, J. Ren, Y. Zhang, Q. Zheng, Y.-L. Wang, Q. Huan, S. Du and H.-J. Gao, *Nano Res.*, 2021, **14**, 4563–4568.
173 Y. Selzer and D. L. Allara, *Annu. Rev. Phys. Chem.*, 2006, **57**, 593–623.
174 Z. Cheng, S. Du, W. Guo, L. Gao, Z. Deng, N. Jiang, H. Guo, H. Tang and H. J. Gao, *Nano Res.*, 2011, **4**, 523–530.
175 Y. H. Jiang, W. D. Xiao, L. W. Liu, L. Z. Zhang, J. C. Lian, K. Yang, S. X. Du and H. J. Gao, *J. Phys. Chem. C*, 2011, **115**, 21750–21754.
176 L. Zhang, Z. Cheng, Q. Huan, X. He, X. Lin, L. Gao, Z. Deng, N. Jiang, Q. Liu, S. Du, H. Guo and H.-j. Gao, *J. Phys. Chem. C*, 2011, **115**, 10791–10796.
177 L. Liu, K. Yang, Y. Jiang, B. Song, W. Xiao, L. Li, H. Zhou, Y. Wang, S. Du, M. Ouyang, W. A. Hofer, A. H. Castro Neto and H.-J. Gao, *Sci. Rep.*, 2013, **3**, 1210.
178 L. W. Liu, K. Yang, W. D. Xiao, Y. H. Jiang, B. Q. Song, S. X. Du and H. J. Gao, *Appl. Phys. Lett.*, 2013, **103**, 023110.
179 K. Yang, L. Liu, L. Zhang, W. Xiao, X. Fei, H. Chen, S. Du, K.-H. Ernst and H.-J. Goo, *ACS Nano*, 2014, **8**, 2246–2251.
180 L. Liu, K. Yang, Y. Jiang, B. Song, W. Xiao, S. Song, S. Du, O. Min, W. A. Hofer, A. H. Castro Neto and H.-J. Gao, *Phys. Rev. Lett.*, 2015, **114**, 126601.
181 J. V. Barth, H. Brune, G. Ertl and R. J. Behm, *Phys. Rev. B: Condens. Matter Mater. Phys.*, 1990, **42**, 9307–9318.
182 S. Yan, Z. Ding, N. Xie, H. Gong, Q. Sun, Y. Guo, X. Shan, S. Meng and X. Lu, *ACS Nano*, 2012, **6**, 4132–4136.
183 C. Joachim, J. K. Gimzewski and A. Aviram, *Nature*, 2000, **408**, 541–548.
184 L. Venkataraman, J. E. Klare, C. Nuckolls, M. S. Hybertsen and M. L. Steigerwald, *Nature*, 2006, **442**, 904–907.
185 K. Moth-Poulsen and T. Bjornholm, *Nat. Nanotechnol.*, 2009, **4**, 551–556.
186 S. V. Aradhya and L. Venkataraman, *Nat. Nanotechnol.*, 2013, **8**, 399–410.
187 S. Wagner, F. Kisslinger, S. Ballmann, F. Schramm, R. Chandrasekar, T. Bodenstein, O. Fuhr, D. Secker, K. Fink, M. Ruben and H. B. Weber, *Nat. Nanotechnol.*, 2013, **8**, 575–579.
188 G. Ke, C. Duan, F. Huang and X. Guo, *InfoMat*, 2020, **2**, 92–112.
189 S. Bouvron, R. Maurand, A. Graf, P. Erler, L. Gragnaniello, M. Skripnik, D. Wiedmann, C. Engesser, C. Nef, W. Fu, C. Schonenberger, F. Pauly and M. Fonin, *Nanoscale*, 2018, **10**, 1487–1493.
190 W. Liang, M. P. Shores, M. Bockrath, J. R. Long and H. Park, *Nature*, 2002, **417**, 725–729.
191 P. S. Cornaglia, H. Ness and D. R. Grempel, *Phys. Rev. Lett.*, 2004, **93**, 147201.
192 J. R. Petta, S. K. Slater and D. C. Ralph, *Phys. Rev. Lett.*, 2004, **93**, 136601.

193 T. Dadosh, Y. Gordin, R. Krahne, I. Khivrich, D. Mahalu, V. Frydman, J. Sperling, A. Yacoby and I. Bar-Joseph, *Nature*, 2005, **436**, 677–680.
194 P. G. Piva, G. A. DiLabio, J. L. Pitters, J. Zikovsky, M. d. Rezeq, S. Dogel, W. A. Hofer and R. A. Wolkow, *Nature*, 2005, **435**, 658–661.
195 N. J. Tao, *Nat. Nanotechnol.*, 2006, **1**, 173–181.
196 L. Venkataraman, *Nat. Nanotechnol.*, 2008, **3**, 187–188.
197 Y. Kitaguchi, S. Habuka, H. Okuyama, S. Hatta, T. Aruga, T. Frederiksen, M. Paulsson and H. Ueba, *Sci. Rep.*, 2015, **5**, 11796.
198 J. Martinez-Blanco, C. Nacci, S. C. Erwin, K. Kanisawa, E. Locane, M. Thomas, F. von Oppen, P. W. Brouwer and S. Foelsch, *Nat. Phys.*, 2015, **11**, 640–644.
199 M. L. Perrin, E. Burzuri and H. S. J. van der Zant, *Chem. Soc. Rev.*, 2015, **44**, 902–919.
200 A. R. Garrigues, L. Wang, E. del Barco and C. A. Nijhuis, *Nat. Commun.*, 2016, **7**, 11595.
201 J. de Bruijckere, P. Gehring, M. Palacios-Corella, M. Clemente-Leon, E. Coronado, J. Paaske, P. Hedegard and H. S. J. van der Zant, *Phys. Rev. Lett.*, 2019, **122**, 197701.
202 P. Gehring, J. M. Thijssen and H. S. J. van der Zant, *Nat. Rev. Phys.*, 2019, **1**, 381–396.
203 I. Fernandez-Torrente, D. Kreikemeyer-Lorenzo, A. Strozecka, K. J. Franke and J. I. Pascual, *Phys. Rev. Lett.*, 2012, **108**, 036801.
204 S. Katano, Y. Kim, M. Hori, M. Trenary and M. Kawai, *Science*, 2007, **316**, 1883–1886.
205 L. Gao, W. Ji, Y. B. Hu, Z. H. Cheng, Z. T. Deng, Q. Liu, N. Jiang, X. Lin, W. Guo, S. X. Du, W. A. Hofer, X. C. Xie and H. J. Gao, *Phys. Rev. Lett.*, 2007, **99**, 106402.
206 J. J. Parks, A. R. Champagne, T. A. Costi, W. W. Shum, A. N. Pasupathy, E. Neuscamman, S. Flores-Torres, P. S. Cornaglia, A. A. Aligia, C. A. Balseiro, G. K.-L. Chan, H. D. Abruña and D. C. Ralph, *Science*, 2010, **328**, 1370–1373.
207 N. Roch, S. Florens, V. Bouchiat, W. Wernsdorfer and F. Balestro, *Nature*, 2008, **453**, U633.
208 S. Schmaus, A. Bagrets, Y. Nahas, T. K. Yamada, A. Bork, M. Bowen, E. Beaurepaire, F. Evers and W. Wulfhekel, *Nat. Nanotechnol.*, 2011, **6**, 185–189.
209 B. Warner, F. El Hallak, H. Prüser, J. Sharp, M. Persson, A. J. Fisher and C. F. Hirjibehedin, *Nat. Nanotechnol.*, 2015, **10**, 259–263.
210 V. Madhavan, W. Chen, T. Jamneala, M. F. Crommie and N. S. Wingreen, *Science*, 1998, **280**, 567–569.
211 G. D. Scott and D. Natelson, *ACS Nano*, 2010, **4**, 3560–3579.
212 A. Zhao, Q. Li, L. Chen, H. Xiang, W. Wang, S. Pan, B. Wang, X. Xiao, J. Yang, J. G. Hou and Q. Zhu, *Science*, 2005, **309**, 1542–1544.
213 Y. Jiang, Y. N. Zhang, J. X. Cao, R. Q. Wu and W. Ho, *Science*, 2011, **333**, 324–328.
214 Y.-S. Fu, S.-H. Ji, X. Chen, X.-C. Ma, R. Wu, C.-C. Wang, W.-H. Duan, X.-H. Qiu, B. Sun, P. Zhang, J.-F. Jia and Q.-K. Xue, *Phys. Rev. Lett.*, 2007, **99**, 256601.
215 P. Wahl, L. Diekhöner, G. Wittich, L. Vitali, M. A. Schneider and K. Kern, *Phys. Rev. Lett.*, 2005, **95**, 166601.
216 V. Iancu, A. Deshpande and S.-W. Hla, *Phys. Rev. Lett.*, 2006, **97**, 266603.
217 R. Robles, N. Lorente, H. Isshiki, J. Liu, K. Katoh, B. K. Breedlove, M. Yamashita and T. Komeda, *Nano Lett.*, 2012, **12**, 3609–3612.
218 N. Atodiresei, J. Brede, P. Lazić, V. Caciuc, G. Hoffmann, R. Wiesendanger and S. Blügel, *Phys. Rev. Lett.*, 2010, **105**, 066601.
219 T. Komeda, H. Isshiki, J. Liu, Y.-F. Zhang, N. Lorente, K. Katoh, B. K. Breedlove and M. Yamashita, *Nat. Commun.*, 2011, **2**, 217.
220 J. Tersoff and D. R. Hamann, *Phys. Rev. Lett.*, 1983, **50**, 1998–2001.
221 K. S. Novoselov, A. K. Geim, S. V. Morozov, D. Jiang, M. I. Katsnelson, I. V. Grigorieva, S. V. Dubonos and A. A. Firsov, *Nature*, 2005, **438**, 197–200.
222 Y. Zhang, Y.-W. Tan, H. L. Stormer and P. Kim, *Nature*, 2005, **438**, 201–204.
223 A. C. Ferrari, J. C. Meyer, V. Scardaci, C. Casiraghi, M. Lazzeri, F. Mauri, S. Piscanec, D. Jiang, K. S. Novoselov, S. Roth and A. K. Geim, *Phys. Rev. Lett.*, 2006, **97**, 187401.
224 A. H. Castro Neto, F. Guinea, N. M. R. Peres, K. S. Novoselov and A. K. Geim, *Rev. Mod. Phys.*, 2009, **81**, 109–162.
225 I. Meric, M. Y. Han, A. F. Young, B. Ozyilmaz, P. Kim and K. L. Shepard, *Nat. Nanotechnol.*, 2008, **3**, 654–659.
226 L. Liao, Y.-C. Lin, M. Bao, R. Cheng, J. Bai, Y. Liu, Y. Qu, K. L. Wang, Y. Huang and X. Duan, *Nature*, 2010, **467**, 305–308.
227 Y. Wu, Y.-m. Lin, A. A. Bol, K. A. Jenkins, F. Xia, D. B. Farmer, Y. Zhu and P. Avouris, *Nature*, 2011, **472**, 74–78.
228 Y. M. Lin, A. Valdes-Garcia, S. J. Han, D. B. Farmer, I. Meric, Y. N. Sun, Y. Q. Wu, C. Dimitrakopoulos, A. Grill, P. Avouris and K. A. Jenkins, *Science*, 2011, **332**, 1294–1297.
229 J. Yan, M. H. Kim, J. A. Elle, A. B. Sushkov, G. S. Jenkins, H. M. Milchberg, M. S. Fuhrer and H. D. Drew, *Nat. Nanotechnol.*, 2012, **7**, 472–478.
230 H. Yang, J. Heo, S. Park, H. J. Song, D. H. Seo, K.-E. Byun, P. Kim, I. Yoo, H.-J. Chung and K. Kim, *Science*, 2012, **336**, 1140–1143.
231 Y. Huang, E. Sutter, N. N. Shi, J. Zheng, T. Yang, D. Englund, H.-J. Gao and P. Sutter, *ACS Nano*, 2015, **9**, 10612–10620.
232 Y. Hernandez, V. Nicolosi, M. Lotya, F. M. Blighe, Z. Sun, S. De, I. T. McGovern, B. Holland, M. Byrne, Y. K. Gun'Ko, J. J. Boland, P. Niraj, G. Duesberg, S. Krishnamurthy, R. Goodhue, J. Hutchison, V. Scardaci, A. C. Ferrari and J. N. Coleman, *Nat. Nanotechnol.*, 2008, **3**, 563–568.
233 J. Mao, L. Huang, Y. Pan, M. Gao, J. He, H. Zhou, H. Guo, Y. Tian, Q. Zou, L. Zhang, H. Zhang, Y. Wang, S. Du, X. Zhou, A. H. C. Neto and H.-J. Gao, *Appl. Phys. Lett.*, 2012, **100**, 093101.
234 S. Lizzit, R. Larciprete, P. Lacovig, M. Dalmiglio, F. Orlando, A. Baraldi, L. Gammelgaard, L. Barreto,

M. Bianchi, E. Perkins and P. Hofmann, *Nano Lett.*, 2012, **12**, 4503–4507.
235 G. Li, H. Zhou, L. Pan, Y. Zhang, L. Huang, W. Xu, S. Du, M. Ouyang, A. C. Ferrari and H.-J. Gao, *J. Am. Chem. Soc.*, 2015, **137**, 7099–7103.
236 G. Li, L. Zhang, W. Xu, J. Pan, S. Song, Y. Zhang, H. Zhou, Y. Wang, L. Bao, Y.-Y. Zhang, S. Du, M. Ouyang, S. T. Pantelides and H.-J. Gao, *Adv. Mater.*, 2018, **30**, 1804650.
237 L. Meng, R. Wu, H. Zhou, G. Li, Y. Zhang, L. Li, Y. Wang and H.-J. Gao, *Appl. Phys. Lett.*, 2012, **100**, 083101.
238 M. Gao, Y. Pan, C. Zhang, H. Hu, R. Yang, H. Lu, J. Cai, S. Du, F. Liu and H.-J. Gao, *Appl. Phys. Lett.*, 2010, **96**, 053109.
239 Y. S. Dedkov, M. Fonin, U. Rüdiger and C. Laubschat, *Phys. Rev. Lett.*, 2008, **100**, 107602.
240 A. Varykhalov, J. Sánchez-Barriga, A. M. Shikin, C. Biswas, E. Vescovo, A. Rybkin, D. Marchenko and O. Rader, *Phys. Rev. Lett.*, 2008, **101**, 157601.
241 M. Gao, Y. Pan, L. Huang, H. Hu, L. Z. Zhang, H. M. Guo, S. X. Du and H.-J. Gao, *Appl. Phys. Lett.*, 2011, **98**, 033101.
242 L. Huang, Y. Pan, L. Pan, M. Gao, W. Xu, Y. Que, H. Zhou, Y. Wang, S. Du and H.-J. Gao, *Appl. Phys. Lett.*, 2011, **99**, 163107.
243 H. Guo, X. Wang, L. Huang, X. Jin, Z. Yang, Z. Zhou, H. Hu, Y.-Y. Zhang, H. Lu, Q. Zhang, C. Shen, X. Lin, L. Gu, Q. Dai, L. Bao, S. Du, W. Hofer, S. T. Pantelides and H.-J. Gao, *Nano Lett.*, 2020, **20**, 8584–8591.
244 P. Y. Huang, S. Kurasch, A. Srivastava, V. Skakalova, J. Kotakoski, A. V. Krasheninnikov, R. Hovden, Q. Mao, J. C. Meyer, J. Smet, D. A. Muller and U. Kaiser, *Nano Lett.*, 2012, **12**, 1081–1086.
245 X. Wu, X. Li, Z. Song, C. Berger and W. A. de Heer, *Phys. Rev. Lett.*, 2007, **98**, 136801.
246 F. V. Tikhonenko, A. A. Kozikov, A. K. Savchenko and R. V. Gorbachev, *Phys. Rev. Lett.*, 2009, **103**, 226801.
247 E. McCann, K. Kechedzhi, V. I. Fal'ko, H. Suzuura, T. Ando and B. L. Altshuler, *Phys. Rev. Lett.*, 2006, **97**, 146805.
248 P. Nemes-Incze, P. Vancsó, Z. Osváth, G. I. Márk, X. Jin, Y.-S. Kim, C. Hwang, P. Lambin, C. Chapelier and L. PéterBiró, *Carbon*, 2013, **64**, 178–186.
249 J. C. Koepke, J. D. Wood, D. Estrada, Z.-Y. Ong, K. T. He, E. Pop and J. W. Lyding, *ACS Nano*, 2013, **7**, 75–86.
250 K. W. Clark, X. G. Zhang, I. V. Vlassiouk, G. He, R. M. Feenstra and A.-P. Li, *ACS Nano*, 2013, **7**, 7956–7966.
251 A. W. Cummings, D. L. Duong, V. L. Nguyen, D. V. Tuan, J. Kotakoski, J. E. B. Vargas, Y. H. Lee and S. Roche, *Adv. Mater.*, 2014, **26**, 5079–5094.
252 P. Willke, C. Möhle, A. Sinterhauf, T. Kotzott, H. K. Yu, A. Wodtke and M. Wenderoth, *Carbon*, 2016, **102**, 470–476.
253 T. Nakayama, O. Kubo, Y. Shingaya, S. Higuchi, T. Hasegawa, C.-S. Jiang, T. Okuda, Y. Kuwahara, K. Takami and M. Aono, *Adv. Mater.*, 2012, **24**, 1675–1692.
254 R.-S. Ma, Q. Huan, L.-M. Wu, J.-H. Yan, Y.-Y. Zhang, L.-H. Bao, Y.-Q. Liu, S.-X. Du and H.-J. Gao, *Chin. Phys. B*, 2017, **26**, 066801.
255 R.-S. Ma, J. Ma, J. Yan, L. Wu, H. Liu, W. Guo, S. Wang, Q. Huan, X. Lin, L. Bao, S. T. Pantelides and H.-J. Gao, *2D Mater.*, 2019, **6**, 045033.
256 R.-S. Ma, J. Ma, J. Yan, L. Wu, W. Guo, S. Wang, Q. Huan, L. Bao, S. T. Pantelides and H.-J. Gao, *Nanoscale*, 2020, **12**, 12038–12045.
257 K. Xu, P. Cao and J. R. Heath, *Nano Lett.*, 2009, **9**, 4446–4451.
258 Y.-N. Wu, X. G. Zhang and S. T. Pantelides, *Semicond. Sci. Technol.*, 2016, **31**, 115016.
259 Y. Ma, Y. Dai, M. Guo, C. Niu, Y. Zhu and B. Huang, *ACS Nano*, 2012, **6**, 1695–1701.
260 H. Zhang, L.-M. Liu and W.-M. Lau, *J. Mater. Chem. A*, 2013, **1**, 10821–10828.
261 A. H. M. A. Wasey, S. Chakrabarty and G. P. Das, *J. Appl. Phys.*, 2015, **117**, 064313.
262 W.-Y. Tong, S.-J. Gong, X. Wan and C.-G. Duan, *Nat. Commun.*, 2016, **7**, 13612.
263 J. Liu, W.-J. Hou, C. Cheng, H.-X. Fu, J.-T. Sun and S. Meng, *J. Phys.: Condens. Matter*, 2017, **29**, 255501.
264 C. F. van Bruggen and C. Haas, *Solid State Commun.*, 1976, **20**, 251–254.
265 F. J. DiSalvo and J. V. Waszczak, *Phys. Rev. B: Condens. Matter Mater. Phys.*, 1981, **23**, 457–461.
266 H. Liu, L. Bao, Z. Zhou, B. Che, R. Zhang, C. Bian, R. Ma, L. Wu, H. Yang, J. Li, C. Gu, C.-M. Shen, S. Du and H.-J. Gao, *Nano Lett.*, 2019, **19**, 4551–4559.
267 H. Liu, Y. Xue, J.-A. Shi, R. A. Guzman, P. Zhang, Z. Zhou, Y. He, C. Bian, L. Wu, R. Ma, J. Chen, J. Yan, H. Yang, C.-M. Shen, W. Zhou, L. Bao and H.-J. Gao, *Nano Lett.*, 2019, **19**, 8572–8580.
268 X. Wang, Z. Zhou, P. Zhang, S. Zhang, Y. Ma, W. Yang, H. Wang, B. Li, L. Meng, H. Jiang, S. Cui, P. Zhai, J. Xiao, W. Liu, X. Zou, L. Bao and Y. Gong, *Chem. Mater.*, 2020, **32**, 2321–2329.
269 B. Li, Z. Wan, C. Wang, P. Chen, B. Huang, X. Cheng, Q. Qian, J. Li, Z. W. Zhang, G. Z. Sun, B. Zhao, H. F. Ma, R. X. Wu, Z. M. Wei, Y. Liu, L. Liao, Y. Ye, Y. Huang, X. D. Xu, X. D. Duan, W. Ji and X. F. Duan, *Nat. Mater.*, 2021, **20**, 818–825.
270 L. Meng, Z. Zhou, M. Xu, S. Yang, K. Si, L. Liu, X. Wang, H. Jiang, B. Li, P. Qin, P. Zhang, J. Wang, Z. Liu, P. Tang, Y. Ye, W. Zhou, L. Bao, H.-J. Gao and Y. Gong, *Nat. Commun.*, 2021, **12**, 809.
271 X. Zhang, Q. Lu, W. Liu, W. Niu, J. Sun, J. Cook, M. Vaninger, P. F. Miceli, D. J. Singh, S.-W. Lian, T.-R. Chang, X. He, J. Du, L. He, R. Zhang, G. Bian and Y. Xu, *Nat. Commun.*, 2021, **12**, 2492.
272 M. Huang, Z. Ma, S. Wang, S. Li, M. Li, J. Xiang, P. Liu, G. Hu, Z. Zhang, Z. Sun, Y. Lu, Z. Sheng, G. Chen, Y .-L. Chueh, S. A. Yang and B. Xiang, *2D Mater.*, 2021, **8**, 031003.
273 X. Sun, W. Li, X. Wang, Q. Sui, T. Zhang, Z. Wang, L. Liu, D. Li, S. Feng, S. Zhong, H. Wang, V. Bouchiat, M. N. Regueiro, N. Rougemaille, J. Coraux, A. Purbawati, A. Hadj-Azzem, Z. Wang, B. Dong, X. Wu, T. Yang, G. Yu,

B. Wang, Z. Han, X. Han and Z. Zhang, *Nano Res.*, 2020, **13**, 3358–3363.
274 C. Xie, P. Yang, Y. Huan, F. Cui and Y. Zhang, *Dalton Trans.*, 2020, **49**, 10319–10327.
275 H. Jiang, P. Zhang, X. Wang and Y. Gong, *Nano Res.*, 2021, **14**, 1789–1801.
276 Z. Zhang, J. Niu, P. Yang, Y. Gong, Q. Ji, J. Shi, Q. Fang, S. Jiang, H. Li, X. Zhou, L. Gu, X. Wu and Y. Zhang, *Adv. Mater.*, 2017, **29**, 1702359.
277 S. Sugai, K. Murase, S. Uchida and S. Tanaka, *J. Phys.*, 1981, **42**, 740–742.
278 J. Yang, W. Wang, Y. Liu, H. Du, W. Ning, G. Zheng, C. Jin, Y. Han, N. Wang, Z. Yang, M. Tian and Y. Zhang, *Appl. Phys. Lett.*, 2014, **105**, 063109.
279 V. N. Strocov, M. Shi, M. Kobayashi, C. Monney, X. Wang, J. Krempasky, T. Schmitt, L. Patthey, H. Berger and P. Blaha, *Phys. Rev. Lett.*, 2012, **109**, 086401.
280 G. Bergmann, *Phys. Rep.*, 1984, **107**, 1–58.
281 Q. Cao, F. F. Yun, L. Sang, F. Xiang, G. Liu and X. Wang, *Nanotechnology*, 2017, **28**, 475703.
282 S. Barua, M. C. Hatnean, M. R. Lees and G. Balakrishnan, *Sci. Rep.*, 2017, **7**, 10964.
283 P. A. Lee and T. V. Ramakrishnan, *Rev. Mod. Phys.*, 1985, **57**, 287–337.
284 H.-R. Fuh, B. Yan, S.-C. Wu, C. Felser and C.-R. Chang, *New J. Phys.*, 2016, **18**, 113038.
285 S. Hikami, A. I. Larkin and Y. Nagaoka, *Prog. Theor. Phys.*, 1980, **63**, 707–710.
286 A. H. Thompson and B. G. Silbernagel, *J. Appl. Phys.*, 1978, **49**, 1477–1479.
287 X. Ding, J. Xing, G. Li, L. Balicas, K. Gofryk and H.-H. Wen, *Phys. Rev. B: Condens. Matter Mater. Phys.*, 2021, **103**, 125115.
288 W. J. Hardy, J. Yuan, H. Guo, P. Zhou, J. Lou and D. Natelson, *ACS Nano*, 2016, **10**, 5941–5946.
289 J. Niu, B. Yan, Q. Ji, Z. Liu, M. Li, P. Gao, Y. Zhang, D. Yu and X. Wu, *Phys. Rev. B: Condens. Matter Mater. Phys.*, 2017, **96**, 075402.
290 D. R. Hamann, *Phys. Rev.*, 1967, **158**, 570–580.
291 T. A. Costi, *Phys. Rev. Lett.*, 2000, **85**, 1504–1507.
292 A. Teruya, F. Suzuki, D. Aoki, F. Honda, A. Nakamura, M. Nakashima, Y. Amako, H. Harima, K. Uchima, M. Hedo, T. Nakama and Y. Ōnuki, *J. Phys.: Conf. Ser.*, 2017, **807**, 012001.
293 H. Sato, F. Nagasaki, Y. Kani, S. Senba, Y. Ueda, A. Kimura and M. Taniguchi, *Solid State Commun.*, 2001, **118**, 563–567.
294 H. Sato, F. Nagasaki, Y. Kani, S. Senba, Y. Ueda, A. Kimura and M. Taniguchi, *Surf. Rev. Lett.*, 2002, **09**, 1315–1319.
295 H. Ma, W. Dang, X. Yang, B. Li, Z. Zhang, P. Chen, Y. Liu, Z. Wan, Q. Qian, J. Luo, K. Zang, X. Duan and X. Duan, *Chem. Mater.*, 2018, **30**, 8891–8896.
296 Y.-X. Lei, N.-X. Miao, J.-P. Zhou, Q. U. Hassan and J.-Z. Wang, *Sci. Technol. Adv. Mater.*, 2017, **18**, 325–333.
297 A. A. Abrikosov, *Phys. Rev. B: Condens. Matter Mater. Phys.*, 1998, **58**, 2788–2794.
298 H. Y. Lv, W. J. Lu, D. F. Shao, Y. Liu and Y. P. Sun, *Phys. Rev. B: Condens. Matter Mater. Phys.*, 2015, **92**, 214419.
299 D. C. Freitas, R. Weht, A. Sulpice, G. Remenyi, P. Strobel, F. Gay, J. Marcus and M. Núñez-Regueiro, *J. Phys.: Condens. Matter*, 2015, **27**, 176002.
300 X. Sun, W. Li, X. Wang, Q. Sui, T. Zhang, Z. Wang, L. Liu, D. Li, S. Feng, S. Zhong, H. Wang, V. Bouchiat, M. Nunez Regueiro, N. Rougemaille, J. Coraux, A. Purbawati, A. Hadj-Azzem, Z. Wang, B. Dong, X. Wu, T. Yang, G. Yu, B. Wang, Z. Han, X. Han and Z. Zhang, *Nano Res.*, 2020, **13**, 3358–3363.
301 L. Meng, Z. Zhou, M. Xu, S. Yang, K. Si, L. Liu, X. Wang, H. Jiang, B. Li, P. Qin, P. Zhang, J. Wang, Z. Liu, P. Tang, Y. Ye, W. Zhou, L. Bao, H.-J. Gao and Y. Gong, *Nat. Commun.*, 2021, **12**, 809.
302 L. Li, Y. Yu, G. J. Ye, Q. Ge, X. Ou, H. Wu, D. Feng, X. H. Chen and Y. Zhang, *Nat. Nanotechnol.*, 2014, **9**, 372–377.
303 L. Tao, E. Cinquanta, D. Chiappe, C. Grazianetti, M. Fanciulli, M. Dubey, A. Molle and D. Akinwande, *Nat. Nanotechnol.*, 2015, **10**, 227–231.
304 B. Radisavljevic, A. Radenovic, J. Brivio, V. Giacometti and A. Kis, *Nat. Nanotechnol.*, 2011, **6**, 147–150.
305 S. Larentis, B. Fallahazad and E. Tutuc, *Appl. Phys. Lett.*, 2012, **101**, 223104.
306 Y.-F. Lin, Y. Xu, S.-T. Wang, S.-L. Li, M. Yamamoto, A. Aparecido-Ferreira, W. Li, H. Sun, S. Nakaharai, W.-B. Jian, K. Ueno and K. Tsukagoshi, *Adv. Mater.*, 2014, **26**, 3263–3269.
307 D. Ovchinnikov, A. Allain, Y.-S. Huang, D. Dumcenco and A. Kis, *ACS Nano*, 2014, **8**, 8174–8181.
308 H. Fang, S. Chuang, T. C. Chang, K. Takei, T. Takahashi and A. Javey, *Nano Lett.*, 2012, **12**, 3788–3792.
309 W. Feng, W. Zheng, W. Cao and P. Hu, *Adv. Mater.*, 2014, **26**, 6587–6593.
310 Z. Deng, D. Cao, J. He, S. Lin, S. M. Lindsay and Y. Liu, *ACS Nano*, 2012, **6**, 6197–6207.
311 H. T. Yuan, M. Toh, K. Morimoto, W. Tan, F. Wei, H. Shimotani, C. Kloc and Y. Iwasa, *Appl. Phys. Lett.*, 2011, **98**, 012102.
312 S.-L. Li, K. Tsukagoshi, E. Orgiu and P. Samorì, *Chem. Soc. Rev.*, 2016, **45**, 118–151.
313 A. Allain, J. Kang, K. Banerjee and A. Kis, *Nat. Mater.*, 2015, **14**, 1195–1205.
314 D. S. Schulman, A. J. Arnold and S. Das, *Chem. Soc. Rev.*, 2018, **47**, 3037–3058.
315 X. Zou, C.-W. Huang, L. Wang, L.-J. Yin, W. Li, J. Wang, B. Wu, Y. Liu, Q. Yao, C. Jiang, W.-W. Wu, L. He, S. Chen, J. C. Ho and L. Liao, *Adv. Mater.*, 2016, **28**, 2062–2069.
316 Y. Liu, J. Guo, E. Zhu, L. Liao, S.-J. Lee, M. Ding, I. Shakir, V. Gambin, Y. Huang and X. Duan, *Nature*, 2018, **557**, 696–700.
317 P.-C. Shen, C. Su, Y. Lin, A.-S. Chou, C.-C. Cheng, J.-H. Park, M.-H. Chiu, A.-Y. Lu, H.-L. Tang, M. M. Tavakoli, G. Pitner, X. Ji, Z. Cai, N. Mao, J. Wang, V. Tung, J. Li, J. Bokor, A. Zettl, C.-I. Wu, T. Palacios, L.-J. Li and J. Kong, *Nature*, 2021, **593**, 211–217.

318 X. Cui, G.-H. Lee, Y. D. Kim, G. Arefe, P. Y. Huang, C.-H. Lee, D. A. Chenet, X. Zhang, L. Wang, F. Ye, F. Pizzocchero, B. S. Jessen, K. Watanabe, T. Taniguchi, D. A. Muller, T. Low, P. Kim and J. Hone, *Nat. Nanotechnol.*, 2015, **10**, 534–540.
319 C. R. Dean, A. F. Young, I. Meric, C. Lee, L. Wang, S. Sorgenfrei, K. Watanabe, T. Taniguchi, P. Kim, K. L. Shepard and J. Hone, *Nat. Nanotechnol.*, 2010, **5**, 722–726.
320 T. Roy, M. Tosun, J. S. Kang, A. B. Sachid, S. B. Desai, M. Hettick, C. C. Hu and A. Javey, *ACS Nano*, 2014, **8**, 6259–6264.
321 P. Luo, F. Zhuge, Q. Zhang, Y. Chen, L. Lv, Y. Huang, H. Li and T. Zhai, *Nanoscale Horiz.*, 2019, **4**, 26–51.
322 K. Zhang and J. Robinson, *MRS Adv.*, 2019, **4**, 2743–2757.
323 D. Kiriya, M. Tosun, P. Zhao, J. S. Kang and A. Javey, *J. Am. Chem. Soc.*, 2014, **136**, 7853–7856.
324 H. G. Ji, P. Solís-Fernández, D. Yoshimura, M. Maruyama, T. Endo, Y. Miyata, S. Okada and H. Ago, *Adv. Mater.*, 2019, **31**, 1903613.
325 G. Wang, L. Bao, T. Pei, R. Ma, Y.-Y. Zhang, L. Sun, G. Zhang, H. Yang, J. Li, C. Gu, S. Du, S. T. Pantelides, R. D. Schrimpf and H.-j. Gao, *Nano Lett.*, 2016, **16**, 6870–6878.
326 S. P. Koenig, R. A. Doganov, L. Seixas, A. Carvalho, J. Y. Tan, K. Watanabe, T. Taniguchi, N. Yakovlev, A. H. Castro Neto and B. Özyilmaz, *Nano Lett.*, 2016, **16**, 2145–2151.
327 Y. Liu, Y. Cai, G. Zhang, Y.-W. Zhang and K.-W. Ang, *Adv. Funct. Mater.*, 2017, **27**, 1604638.
328 M. Li, C.-Y. Lin, S.-H. Yang, Y.-M. Chang, J.-K. Chang, F.-S. Yang, C. Zhong, W.-B. Jian, C.-H. Lien, C.-H. Ho, H.-J. Liu, R. Huang, W. Li, Y.-F. Lin and J. Chu, *Adv. Mater.*, 2018, **30**, 1803690.
329 S. Chuang, C. Battaglia, A. Azcatl, S. McDonnell, J. S. Kang, X. Yin, M. Tosun, R. Kapadia, H. Fang, R. M. Wallace and A. Javey, *Nano Lett.*, 2014, **14**, 1337–1342.
330 D. Xiang, C. Han, J. Wu, S. Zhong, Y. Liu, J. Lin, X.-A. Zhang, W. Ping Hu, B. Özyilmaz, A. H. C. Neto, A. T. S. Wee and W. Chen, *Nat. Commun.*, 2015, **6**, 6485.
331 Y. Wang, D. Xiang, Y. Zheng, T. Liu, X. Ye, J. Gao, H. Yang, C. Han and W. Chen, *Adv. Opt. Mater.*, 2020, **8**, 1901867.
332 S. Tongay, J. Zhou, C. Ataca, J. Liu, J. S. Kang, T. S. Matthews, L. You, J. Li, J. C. Grossman and J. Wu, *Nano Lett.*, 2013, **13**, 2831–2836.
333 D. Qu, X. Liu, M. Huang, C. Lee, F. Ahmed, H. Kim, R. S. Ruoff, J. Hone and W. J. Yoo, *Adv. Mater.*, 2017, **29**, 1606433.
334 Y. Wang, Y. Zheng, C. Han and W. Chen, *Nano Res.*, 2021, **14**, 1682–1697.
335 M. Buscema, D. J. Groenendijk, G. A. Steele, H. S. J. van der Zant and A. Castellanos-Gomez, *Nat. Commun.*, 2014, **5**, 4651.
336 B. W. H. Baugher, H. O. H. Churchill, Y. Yang and P. Jarillo-Herrero, *Nat. Nanotechnol.*, 2014, **9**, 262–267.
337 A. Pospischil, M. M. Furchi and T. Mueller, *Nat. Nanotechnol.*, 2014, **9**, 257–261.
338 J. S. Ross, P. Klement, A. M. Jones, N. J. Ghimire, J. Yan, D. G. Mandrus, T. Taniguchi, K. Watanabe, K. Kitamura, W. Yao, D. H. Cobden and X. Xu, *Nat. Nanotechnol.*, 2014, **9**, 268–272.
339 D. Li, M. Chen, Z. Sun, P. Yu, Z. Liu, P. M. Ajayan and Z. Zhang, *Nat. Nanotechnol.*, 2017, **12**, 901–906.
340 G. Wu, B. Tian, L. Liu, W. Lv, S. Wu, X. Wang, Y. Chen, J. Li, Z. Wang, S. Wu, H. Shen, T. Lin, P. Zhou, Q. Liu, C. Duan, S. Zhang, X. Meng, S. Wu, W. Hu, X. Wang, J. Chu and J. Wang, *Nat. Electron.*, 2020, **3**, 43–50.
341 L. Tong, Z. Peng, R. Lin, Z. Li, Y. Wang, X. Huang, K.-H. Xue, H. Xu, F. Liu, H. Xia, P. Wang, M. Xu, W. Xiong, W. Hu, J. Xu, X. Zhang, L. Ye and X. Miao, *Science*, 2021, **373**, 1353–1358.
342 A. Castellanos-Gomez, M. Buscema, R. Molenaar, V. Singh, L. Janssen, H. S. J. van der Zant and G. A. Steele, *2D Mater.*, 2014, **1**, 011002.
343 S. P. Koenig, R. A. Doganov, H. Schmidt, A. H. C. Neto and B. Özyilmaz, *Appl. Phys. Lett.*, 2014, **104**, 103106.
344 H. Liu, A. T. Neal, Z. Zhu, Z. Luo, X. Xu, D. Tománek and P. D. Ye, *ACS Nano*, 2014, **8**, 4033–4041.
345 H. Liu, A. T. Neal, M. Si, Y. Du and P. D. Ye, *IEEE Electron Device Lett.*, 2014, **35**, 795–797.
346 S. Das, M. Demarteau and A. Roelofs, *ACS Nano*, 2014, **8**, 11730–11738.
347 Y. Du, H. Liu, Y. Deng and P. D. Ye, *ACS Nano*, 2014, **8**, 10035–10042.
348 C. Han, Z. Hu, L. C. Gomes, Y. Bao, A. Carvalho, S. J. R. Tan, B. Lei, D. Xiang, J. Wu, D. Qi, L. Wang, F. Huo, W. Huang, K. P. Loh and W. Chen, *Nano Lett.*, 2017, **17**, 4122–4129.
349 J. Kim, S. S. Baik, S. H. Ryu, Y. Sohn, S. Park, B.-G. Park, J. Denlinger, Y. Yi, H. J. Choi and K. S. Kim, *Science*, 2015, **349**, 723–726.
350 X. Yu, S. Zhang, H. Zeng and Q. J. Wang, *Nano Energy*, 2016, **25**, 34–41.
351 G. Wang, L. Bao, R. Ma, T. Pei, Y.-Y. Zhang, L. Wu, Z. Zhou, H. Yang, J. Li, C. Gu, S. Du, S. T. Pantelides and H.-J. Gao, *2D Mater.*, 2017, **4**, 025056.
352 Y. Liu and K.-W. Ang, *ACS Nano*, 2017, **11**, 7416–7423.
353 L. Chen, S. Li, X. Feng, L. Wang, X. Huang, B. C. K. Tee and K.-W. Ang, *Adv. Electron. Mater.*, 2018, **4**, 1800274.
354 P. Wu, D. Reis, X. S. Hu and J. Appenzeller, *Nat. Electron.*, 2021, **4**, 45–53.
355 F. H. L. Koppens, T. Mueller, P. Avouris, A. C. Ferrari, M. S. Vitiello and M. Polini, *Nat. Nanotechnol.*, 2014, **9**, 780–793.
356 O. Lopez-Sanchez, D. Lembke, M. Kayci, A. Radenovic and A. Kis, *Nat. Nanotechnol.*, 2013, **8**, 497–501.
357 M. Buscema, D. J. Groenendijk, S. I. Blanter, G. A. Steele, H. S. J. van der Zant and A. Castellanos-Gomez, *Nano Lett.*, 2014, **14**, 3347–3352.
358 X. Wang, P. Wang, J. Wang, W. Hu, X. Zhou, N. Guo, H. Huang, S. Sun, H. Shen, T. Lin, M. Tang, L. Liao, A. Jiang, J. Sun, X. Meng, X. Chen, W. Lu and J. Chu, *Adv. Mater.*, 2015, **27**, 6575–6581.

359 H. Huang, X. Wang, P. Wang, G. Wu, Y. Chen, C. Meng, L. Liao, J. Wang, W. Hu, H. Shen, T. Lin, J. Sun, X. Meng, X. Chen and J. Chu, *RSC Adv.*, 2016, **6**, 87416–87421.
360 G. W. Mudd, S. A. Svatek, L. Hague, O. Makarovsky, Z. R. Kudrynskyi, C. J. Mellor, P. H. Beton, L. Eaves, K. S. Novoselov, Z. D. Kovalyuk, E. E. Vdovin, A. J. Marsden, N. R. Wilson and A. Patanè, *Adv. Mater.*, 2015, **27**, 3760–3766.
361 W. Huang, L. Gan, H. Li, Y. Ma and T. Zhai, *CrystEngComm*, 2016, **18**, 3968–3984.
362 S. R. Tamalampudi, Y.-Y. Lu, R. K. UlaganUathan, R. Sankar, C.-D. Liao, K. M. Boopathi, C.-H. Cheng, F. C. Chou and Y.-T. Chen, *Nano Lett.*, 2014, **14**, 2800–2806.
363 L. Tao and Y. Li, *RSC Adv.*, 2017, **7**, 49694–49700.
364 Z. Yang, W. Jie, C.-H. Mak, S. Lin, H. Lin, X. Yang, F. Yan, S. P. Lau and J. Hao, *ACS Nano*, 2017, **11**, 4225–4236.
365 L. Liu, L. Wu, A. Wang, H. Liu, R. Ma, K. Wu, J. Chen, Z. Zhou, Y. Tian, H. Yang, C. Shen, L. Bao, Z. Qin, S. T. Pantelides and H.-J. Gao, *Nano Lett.*, 2020, **20**, 6666–6673.
366 L. Wu, J. Shi, Z. Zhou, J. Yan, A. Wang, C. Bian, J. Ma, R. Ma, H. Liu, J. Chen, Y. Huang, W. Zhou, L. Bao, M. Ouyang, S. T. Pantelides and H.-J. Gao, *Nano Res.*, 2020, **13**, 1127–1132.
367 X. Wang, H. Shen, Y. Chen, G. Wu, P. Wang, H. Xia, T. Lin, P. Zhou, W. Hu, X. Meng, J. Chu and J. Wang, *Adv. Sci.*, 2019, **6**, 1901050.
368 W. Feng, X. Zhou, W. Q. Tian, W. Zheng and P. Hu, *Phys. Chem. Chem. Phys.*, 2015, **17**, 3653–3658.
369 S. Sucharitakul, N. J. Goble, U. R. Kumar, R. Sankar, Z. A. Bogorad, F.-C. Chou, Y.-T. Chen and X. P. A. Gao, *Nano Lett.*, 2015, **15**, 3815–3819.
370 P.-H. Ho, Y.-R. Chang, Y.-C. Chu, M.-K. Li, C.-A. Tsai, W.-H. Wang, C.-H. Ho, C.-W. Chen and P.-W. Chiu, *ACS Nano*, 2017, **11**, 7362–7370.
371 S. Lei, L. Ge, S. Najmaei, A. George, R. Kappera, J. Lou, M. Chhowalla, H. Yamaguchi, G. Gupta, R. Vajtai, A. D. Mohite and P. M. Ajayan, *ACS Nano*, 2014, **8**, 1263–1272.
372 W. Feng, J.-B. Wu, X. Li, W. Zheng, X. Zhou, K. Xiao, W. Cao, B. Yang, J.-C. Idrobo, L. Basile, W. Tian, P. Tan and P. Hu, *J. Mater. Chem. C*, 2015, **3**, 7022–7028.
373 W. Luo, Y. Cao, P. Hu, K. Cai, Q. Feng, F. Yan, T. Yan, X. Zhang and K. Wang, *Adv. Opt. Mater.*, 2015, **3**, 1418–1423.
374 Z. Li, H. Qiao, Z. Guo, X. Ren, Z. Huang, X. Qi, S. C. Dhanabalan, J. S. Ponraj, D. Zhang, J. Li, J. Zhao, J. Zhong and H. Zhang, *Adv. Funct. Mater.*, 2018, **28**, 1705237.
375 G.-H. Lee, Y.-J. Yu, X. Cui, N. Petrone, C.-H. Lee, M. S. Choi, D.-Y. Lee, C. Lee, W. J. Yoo, K. Watanabe, T. Taniguchi, C. Nuckolls, P. Kim and J. Hone, *ACS Nano*, 2013, **7**, 7931–7936.
376 B. Radisavljevic, M. B. Whitwick and A. Kis, *ACS Nano*, 2011, **5**, 9934–9938.
377 H. Wang, L. Yu, Y.-H. Lee, Y. Shi, A. Hsu, M. L. Chin, L.-J. Li, M. Dubey, J. Kong and T. Palacios, *Nano Lett.*, 2012, **12**, 4674–4680.
378 S. Das, M. Dubey and A. Roelofs, *Appl. Phys. Lett.*, 2014, **105**, 083511.
379 Y.-F. Lin, Y. Xu, S.-T. Wang, S.-L. Li, M. Yamamoto, A. Aparecido-Ferreira, W. Li, H. Sun, S. Nakaharai, W.-B. Jian, K. Ueno and K. Tsukagoshi, *Adv. Mater.*, 2014, **26**, 3263–3269.
380 M. Tosun, S. Chuang, H. Fang, A. Sachid, M. Hettick, Y. Lin, Y. Zeng and A. Javey, *ACS Nano*, 2014, **8**, 4948–4953.
381 E. Liu, Y. Fu, Y. Wang, Y. Feng, H. Liu, X. Wan, W. Zhou, B. Wang, L. Shao, C.-H. Ho, Y.-S. Huang, Z. Cao, L. Wang, A. Li, J. Zeng, F. Song, X. Wang, Y. Shi, H. Yuan, H. Y. Hwang, Y. Cui, F. Miao and D. Xing, *Nat. Commun.*, 2015, **6**, 6991.
382 J. Pu, K. Funahashi, C.-H. Chen, M.-Y. Li, L.-J. Li and T. Takenobu, *Adv. Mater.*, 2016, **28**, 4111–4119.
383 M. Zhao, Y. Ye, Y. Han, Y. Xia, H. Zhu, S. Wang, Y. Wang, D. A. Muller and X. Zhang, *Nat. Nanotechnol.*, 2016, **11**, 954–959.
384 Y. Li, C. Yu, Y. Gan, Y. Kong, P. Jiang, D.-F. Zou, P. Li, X.-F. Yu, R. Wu, H. Zhao, C.-F. Gao and J. Li, *Nanotechnology*, 2019, **30**, 335703.
385 Q. Zhao, R. Frisenda, T. Wang and A. Castellanos-Gomez, *Nanoscale*, 2019, **11**, 9845–9850.
386 L. Wu, A. Wang, J. Shi, J. Yan, Z. Zhou, C. Bian, J. Ma, R. Ma, H. Liu, J. Chen, Y. Huang, W. Zhou, L. Bao, M. Ouyang, S. J. Pennycook, S. T. Pantelides and H.-J. Gao, *Nat. Nanotechnol.*, 2021, **16**, 882–887.
387 L. Liu, C. Liu, L. Jiang, J. Li, Y. Ding, S. Wang, Y.-G. Jiang, Y.-B. Sun, J. Wang, S. Chen, D. W. Zhang and P. Zhou, *Nat. Nanotechnol.*, 2021, **16**, 874–881.
388 D. Kahng and S. M. Sze, *Bell Syst. Techn. J.*, 1967, **46**, 1288–1295.
389 A. J. Hong, E. B. Song, H. S. Yu, M. J. Allen, J. Kim, J. D. Fowler, J. K. Wassei, Y. Park, Y. Wang, J. Zou, R. B. Kaner, B. H. Weiller and K. L. Wang, *ACS Nano*, 2011, **5**, 7812–7817.
390 S. Bertolazzi, D. Krasnozhon and A. Kis, *ACS Nano*, 2013, **7**, 3246–3252.
391 L. Jae-Duk, H. Sung-Hoi and C. Jung-Dal, *IEEE Electron Device Lett.*, 2002, **23**, 264–266.
392 M. Sup Choi, G.-H. Lee, Y.-J. Yu, D.-Y. Lee, S. Hwan Lee, P. Kim, J. Hone and W. Jong Yoo, *Nat. Commun.*, 2013, **4**, 1624.
393 D. Li, X. Wang, Q. Zhang, L. Zou, X. Xu and Z. Zhang, *Adv. Funct. Mater.*, 2015, **25**, 7360–7365.
394 S. Wang, C. He, J. Tang, X. Lu, C. Shen, H. Yu, L. Du, J. Li, R. Yang, D. Shi and G. Zhang, *Adv. Electron. Mater.*, 2019, **5**, 1800726.
395 Q. A. Vu, Y. S. Shin, Y. R. Kim, V. L. Nguyen, W. T. Kang, H. Kim, D. H. Luong, I. M. Lee, K. Lee, D.-S. Ko, J. Heo, S. Park, Y. H. Lee and W. J. Yu, *Nat. Commun.*, 2016, **7**, 12725.
396 J. J. Yang, D. B. Strukov and D. R. Stewart, *Nat. Nanotechnol.*, 2013, **8**, 13–24.
397 T. Szkopek, *Nat. Nanotechnol.*, 2021, **16**, 853–854.